Numerical Modeling and Experimental Testing of a Mixed Gas Joule-Thomson Cryocooler

by

John Pettitt

A thesis submitted in partial fulfillment of

the requirements for the degree of

Master of Science

(Mechanical Engineering)

at the

UNIVERSITY OF WISCONSIN-MADISON

2006

Approved by

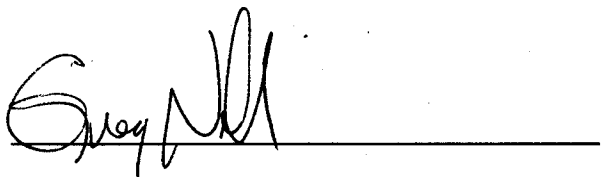

4/27/06

Assistant Professor Gregory F. Nellis — Date

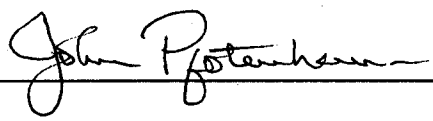

4/27/06

Professor John M. Pfotenhauer — Date

Abstract

Mixed gas Joule-Thomson (MGJT) systems have been shown to provide order of magnitude improvements in efficiency relative to JT systems that use pure working fluids. This thesis presents theoretical and experimental work related to using a single-stage, low power (< 1 W) MGJT system for cooling the current leads required by high-temperature superconducting electronics. By thermally integrating the current leads with the recuperative heat exchanger of a MGJT cycle, it is possible to intercept the electrical dissipation and conductive heat leak of the wires at a relatively high temperature which provides a thermodynamic advantage. Also, directly cooling the leads rather than indirectly cooling the chips may provide some advantages relative to thermal integration.

To design the recuperative heat exchanger for the MGJT cycle, the composition of the gas mixture was optimized using a robust genetic optimization technique. Following mixture selection, the optimization model was modified so that it included the effect of frictional pressure drop, axial conduction through the heat exchanger, and the overall conductance available from the heat exchanger on the performance of the MGJT cycle. The individual influences of these loss factors on the refrigeration power of the MGJT cycle were investigated parametrically and conceptually in order to determine the target values for a low power system and develop some insight into the relative importance of each effect. A detailed model of the specific Hampson-style heat exchanger geometry was developed and used to obtain a design for an initial demonstration device.

The demonstration device was fabricated and integrated with a thermal vacuum test facility, gas handling equipment, and the appropriate instrumentation. Several tests were carried out. First, the heat exchanger alone was tested (outside of a JT cycle) using helium as the working fluid. These data provided some experimental verification of the detailed model. Next, the test facility was modified through the installation of a fixed orifice expansion valve to allow open cycle testing of the device using high pressure (9.745 MPa) pure Argon. These measurements provided further insight into the performance of the device.

The test facility was subsequently integrated with a compressor in order to allow measurements of the Device's performance using gas mixtures in a closed loop configuration. These test results ultimately revealed issues relative to contamination, which were addressed through the installation of a liquid nitrogen trap, as well as liquid management. The liquid management issue is thought to be related to inadequate vapor kinetic energy which does not provide sufficient momentum transfer to the liquid to move it through the system. The liquid management issue constrains the performance of the MGJT cycle at low mass flow rates and was explored over a very limited range of conditions. Further testing is suggested which will allow the liquid management constraint to be explored more completely in order to guide future designs.

Acknowledgements

I would like to acknowledge the people who have assisted this project. First, I would like to thank my advisors Greg Nellis and John Pfotenhauer for giving me their guidance and their patience. They have done an excellent job of creating a positive atmosphere in which to perform this research.

Next, I would like to thank Dan Hoch for sharing his vast expertise and intuition with me; and for sharing his genuine friendship with me. I would also like to thank Sandy Klein for EES and the way its changed my thinking; Natalie Meagher and Steve Meitner, who assisted with several experimental aspects of this project. And finally, I want to acknowledge the Office of Naval Research for their financial support of this research.

Table of Contents

List of Figures

List of Tables

List of Variables

A	Area (m^2)
A_b	Surface area of tube base (m^2)
A_f	Area of a fin (m^2)
A_{ff}	Free-flow area (m^2)
cp	specific heat (kJ/kg-K)
D_{helix}	Diameter of helix (m)
err	Percent Error
Fin_{OD}	Fin diameter (m)
$Fins_{inch}$	Fins per inch (1/in)
G	Mass flux (kg/s-m^2)
h	Enthalpy (J/g)
htc	Heat transfer coefficient (W/m^2-K)
ID	Inner Diameter (in or m)
k	Thermal conductivity (W/m-K)
L	Length (m)
L_{fins}	Length or height of fins from tube base (m)
Lp	Longitudinal pitch (m)
$\dot{m}$	Mass flow rate (g/s or kg/s)
M	Number of heat exchanger segments in detailed model (equal lengths) (-)
N	Number of recuperative heat transfer segments in optimization model (-)
N_{fins}	Number of fins (-)
Nu	Nusselt number (-)
N_T	Number of Tubes (-)
OD	Outer Diameter (in or m)
P	Pressure (kpa or psig)
Pr	Prandtl number
$\dot{Q}_{load,cold}$	Heat load applied to cold end of heat exchanger (W)
$\dot{Q}_{load,dist}$	Distributed heat load along the heat exchanger length (W)
$\dot{Q}_{rec}$	Recuperated heat (kJ/kg)
$\dot{Q}_{rej}$	Heat Rejected from cycle to surroundings (J/g)
R	Thermal resistance (K/W)
r	Radius (m)
Re	Reynolds number (-)
rf_{ft}	Fin radius on finned tube (m)
Sbc	Spacing between coils (m)
Sbc_{adj}	Spacing between adjacent coils (m)
S_{ft}	Spacing between fins (m)
t	Thickness (m)
T	Temperature (K)
tf_{ft}	thickness of fin on the finned tube (m)

Tp	Transverse pitch (m)
UA	Heat exchanger stream-to-stream conductance (W/K)
$\dot{V}$	Volume flow rate (L/min or Ft^3/hr)
$\dot{W}_{comp}$	Isentropic compressor work (J/g)
X_T	Non-dimensional Transverse pitch (-)
X_L	Non-dimensional Longitudinal pitch (-)
y_i	Mole fraction of component *i* of mixture

Greek

ΔT	Hot end temperature difference (K)
η	Fin efficiency (-)
η_o	Overall fin efficiency (-)
μ	Dynamic viscosity (kg/m-s)

Subscripts

h/high/hot/HP	Associated with the high pressure or hot stream
c/low/cold/LP	Associated with the low pressure or cold stream
inlet	Entrance to cryostat/experiment
outlet	Exit of cryostat/experiment
freeze	Freezing temperature
tp	Triple point
sat	Saturation state
spec	Specified by geometry
axial	Straight line between the hot end and cold end of the heat exchanger
cond	Conduction heat transfer in the axial direction
ft	Associated with the finned tube
ot	Outer tube
it	Inner tube
tot	Total or sum

Chapter 1 Introduction

1.1 Actively Cooled Current Leads

High temperature superconducting (HTS) electronics are being developed in order to operate in the temperature range of 80 K to 120 K. These electronic components must be mounted on a cold stage that is actively cooled via a thermal connection with any one of several types of commercially available cryocoolers, as shown in Figure 1.1. A large part of the heat load on the system is related to the current leads that carry the bias current and signals from room temperature electronics. The heat leak from these wires onto the high temperature superconducting chips is related to conduction along the leads as well as ohmic dissipation (because these leads are not superconducting).

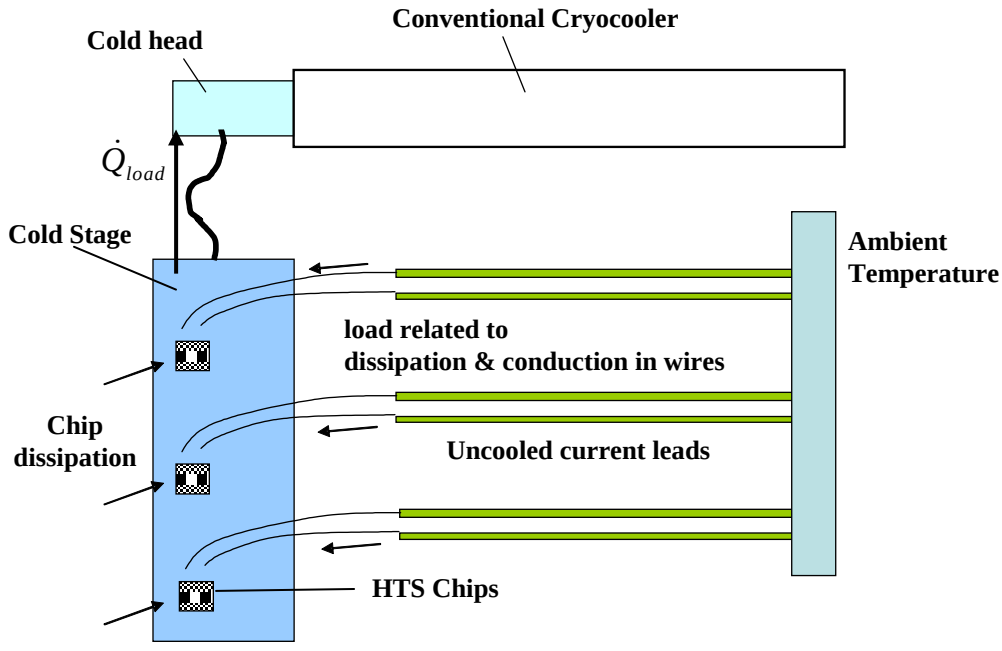

Figure 1.1: The conventional cooling configuration used for high temperature superconducting electronics.

There are two disadvantages associated with the cooling configuration shown in Figure 1.1. Thermal integration with the cryocooler is difficult. The current leads deposit thermal loads throughout the electronics package at the various electrical connections however the cooling load is removed from a single thermal interface with the cold stage. Therefore, chips mounted closer to the cold stage will be colder than those mounted further away. The performance of superconducting electronics is sensitive to temperature and it is important that interfacing chips be at the same temperature.

Also, the heat is allowed to reach the lowest temperature part of the cycle before it is removed. Entropy is the ratio of heat transfer to temperature and therefore, the heat load represents the largest entropy flow at the coldest point in the cycle. The power and size requirements of the cryocooler generally scale with the entropy flow that it must remove and therefore there is a thermodynamic advantage associated with removing the heat load at a higher temperature.

Ideally, the entire electronics package would be kept at a uniform cryogenic temperature and the heat generated by ohmic dissipation would be removed at a temperature very near where it was generated. Several researchers, including Williams (1963), have shown that cooling current leads carrying high currents for large superconducting magnets with vapor cryogen allow for much of the heat leak to be intercepted before it reaches the cold end. Vapor cooling current leads for high temperature superconducting electronics has not previously been studied. The direct implementation of vapor cooling via the boil-off

of a cryogen is not likely to be feasible for applications that require a gravity independent system due to the presence of the liquid.

The objective of this thesis is to study a system in which the current leads are thermally integrated with the recuperative heat exchanger within a mixed gas Joule-Thomson (MGJT) system, as shown in Figure 1.2. The recuperative heat exchanger removes the conductive and ohmic heat leak of the current leads at the temperature where it is generated and also provides cooling to the HTS computer chips at several locations in the electronics package. The cooling is provided via the leads rather than indirectly (as shown in Figure 1.2). This actively cooled current lead concept has thermal integration and thermodynamic advantages; the configuration may permit a more uniform temperature distribution from chip-to-chip and also allow heat to be removed from the system in a more reversible manner.

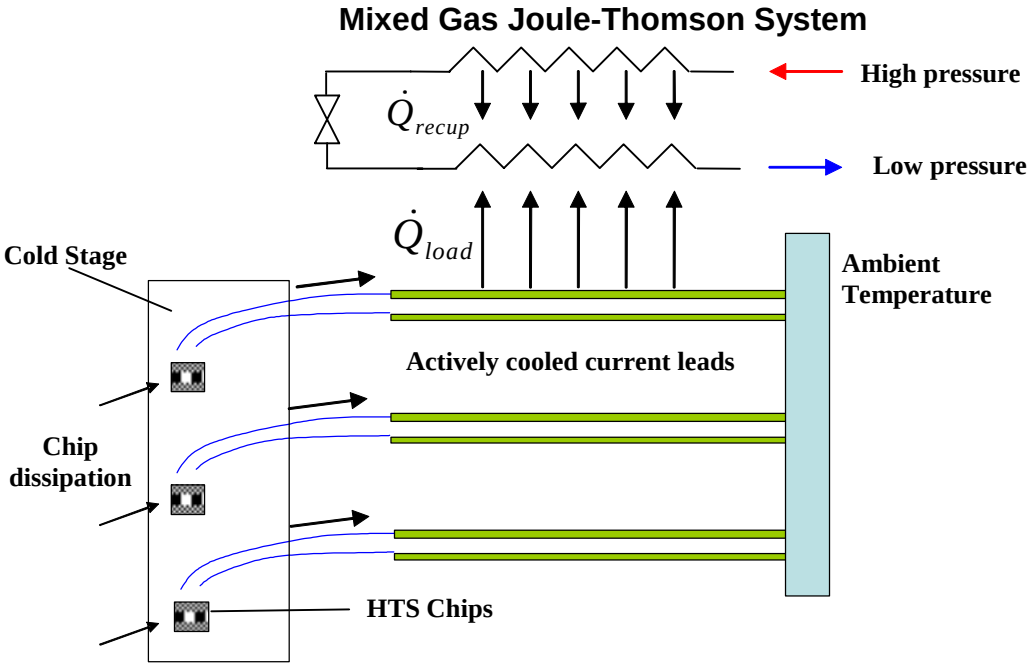

Figure 1.2: The proposed method of cooling HTS electronics.

This project has focused primarily on the details of the MGJT refrigeration cycle; while there has been substantial research in this area, there has been relatively little detailed theoretical work reported that supports the more numerous publications regarding specific experimental results. Also, the use of an MGJT system for high efficiency, low power, low temperature applications involving a distributed load has not been thoroughly studied. In the following sections, JT and MGJT systems are introduced and discussed.

1.2 Mixed Gas Joule-Thomson Cycle

The simplest, closed cycle configuration for a Joule-Thomson system is shown in Figure 1.3. The cycle consists of a compressor, an aftercooler, a recuperative heat exchanger, a valve, and an evaporator or load heat exchanger. In this cycle, the working fluid is compressed to a high pressure (state 2) and cooled to room temperature (state 3) in the aftercooler. The high pressure gas enters the recuperative heat exchanger and is cooled (by the returning low pressure gas) until it exits the heat exchanger at a cryogenic temperature (state 4). The high pressure, cold working fluid is expanded through a valve; this isenthalpic expansion causes the temperature of the fluid to drop (state 5). The cold, low pressure fluid accepts heat as it passes through the load heat exchanger or evaporator. The working fluid enters the cold end of the heat exchanger (state 6) and warms as it pre-cools the high pressure gas until finally it exits the heat exchanger and enters the suction side of the compressor (state 1).

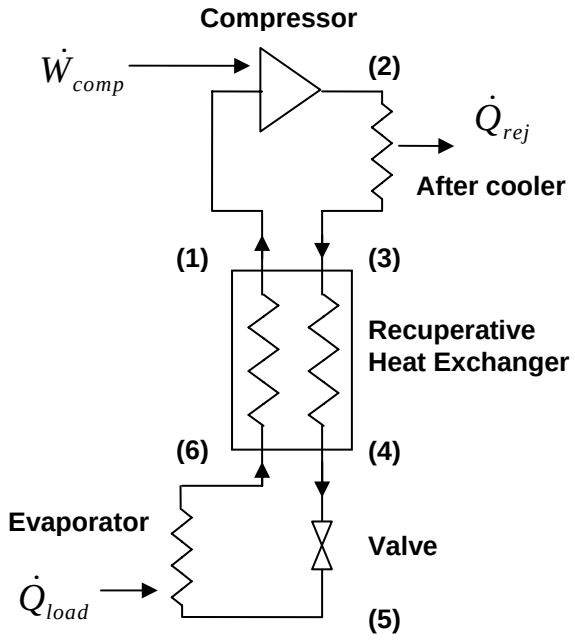

Figure 1.3: Component diagram for a Joule-Thomson cycle.

The refrigeration cycle shown in Figure 1.3 is named after the Joule-Thomson effect, which is the temperature response of the working fluid to the constant enthalpy pressure drop through the valve. For ideal gases, enthalpy is only a function of temperature and not of pressure. Therefore there is no temperature response for an ideal gas to an isenthalpic expansion. If the working fluid behaves as an ideal gas at the operating pressures and temperatures within the system then it cannot be used within a Joule-Thomson system. The working fluid within a Joule-Thomson system must exhibit substantial non-ideal (or real gas) behavior in order to provide refrigeration. This must be true over the entire temperature range spanned by the system; in Figure 1.3, the working fluid must provide a large real gas effect from T_5 to T_1.

Pure fluids, such as argon or nitrogen, provide only a small real gas effect near room temperature at the pressure levels that are achievable using conventional, small compressors; therefore, these pure fluids can provide only a small refrigeration capacity when operating between room temperature and cryogenic temperatures. An intuitive discussion of this has been presented by Alexeev, Haberstroh, and Quack (1997) and Keppler, Nellis, and Klein (2004). Consider an ideal JT cycle, that is, one in which the heat exchanger has an infinite stream-to-stream conductance (*UA*), is perfectly insulated, and allows the flow of working fluid with no pressure drop. In such a cycle, the maximum possible cooling load that can be accepted in the evaporator (per unit mass flow rate of fluid) is equal to the minimum value of the enthalpy difference between the high and low pressure streams at the hot end of the heat exchanger,

$$\frac{\dot{Q}_{\max}}{\dot{m}} = h_1 - h_3 = h(T_1, P_1) - h(T_3, P_3) = h(T, P_1) - h(T, P_3) \tag{1.1}$$

Since the recuperative heat exchanger is perfect, the temperatures T_1 and T_3 are equal (the pinchpoint within the recuperative heat exchanger occurs at the hot end) and so for a set of operating pressures, the maximum cooling power is a function of the hot end temperature only. The maximum refrigeration capacity per unit of mass flow rate for argon and nitrogen operating between the cycle pressures of 1000 KPa and 100 KPa is illustrated in Figure 1.4. Note the sharp peak that occurs when the saturation temperature of the fluid at the high pressure is reached and then the precipitous drop that occurs at the saturation temperature of the fluid at low pressure. Between these temperatures the performance of the fluid is high as the fluid is within its vapor dome and therefore exhibits an extremely high real gas effect. The saturation temperature of the fluid at its

low pressure represents the minimum temperature that the cycle can achieve; the liquid state of the fluid is essentially incompressible and, like an ideal gas, has a very small real gas effect.

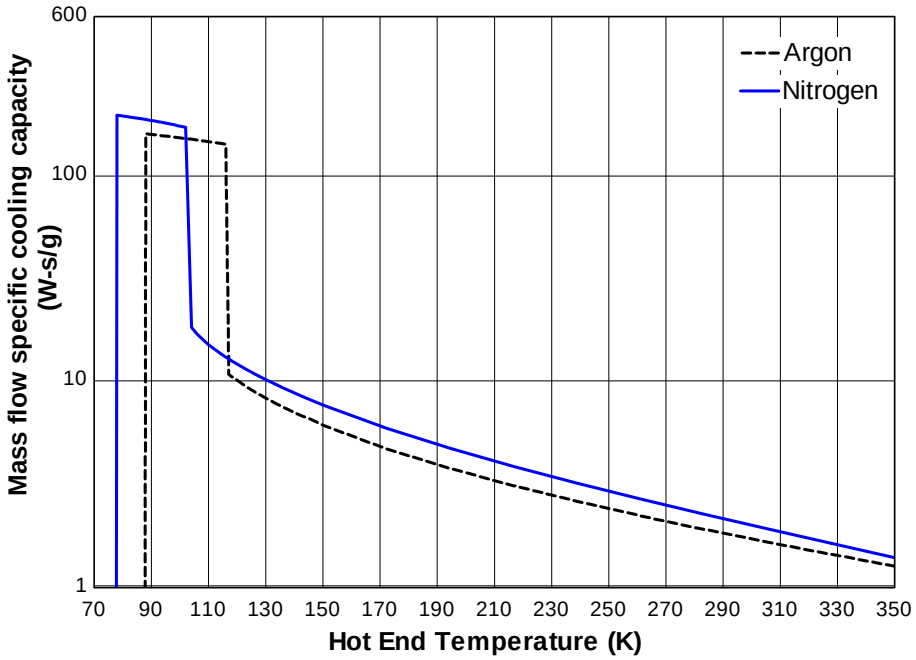

Figure 1.4: Maximum cooling power per unit of mass flow rate for a closed JT cycle using argon and nitrogen as a function of hot end temperature for operating pressures of 100 kPa and 1000 kPa.

There are other fluids which have greater real gas behavior near room temperature, such as ethane and methane; the maximum cooling capacity per unit mass flow rate for these fluids are shown together with nitrogen and argon in Figure. 1.5.

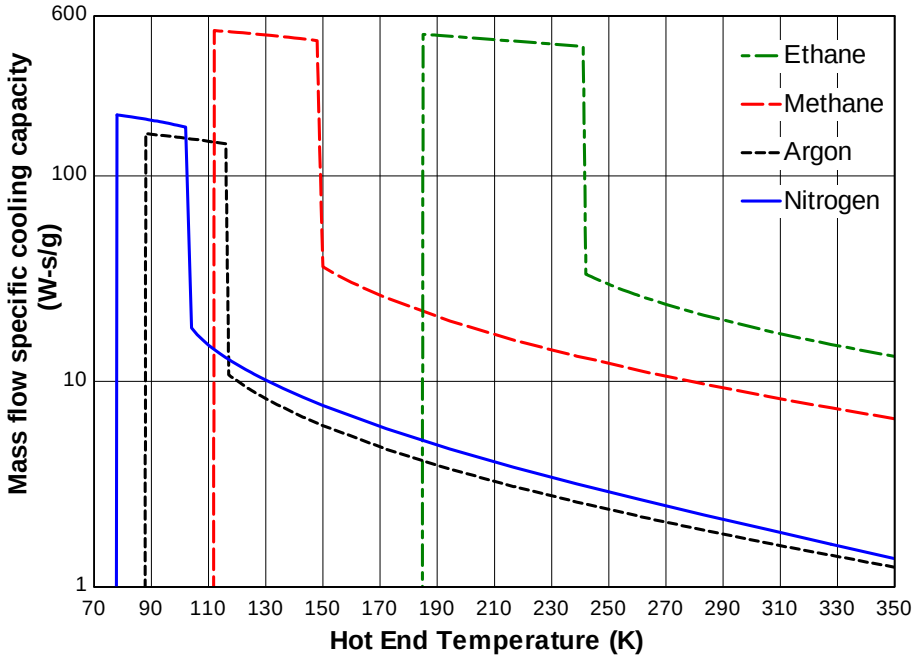

Figure 1.5: Maximum cooling power per unit of mass flow rate for a closed JT cycle as a function of hot end temperature for operating pressures of 100 kPa and 1000 kPa.

Notice that methane and ethane can provide much greater refrigeration power than argon and nitrogen; however, the coldest achievable temperature is much higher for these fluids. The limitation on minimum temperature is a consequence of the saturation temperature of the low pressure stream and this has kept pure working fluids like methane and ethane from being options for JT systems cooling superconducting electronics because they do not provide refrigeration at low enough temperatures.

It was Alfeev (1973) who proposed that mixtures of the fluids shown in Figure 1.5 as well as other hydrocarbons and halocarbons could be created to provide a high refrigeration power over the large temperature range of 300 K to 80 K by essentially smoothing out the sharp peaks exhibited in Figure 1.5. Mixtures exhibit a behavior

referred to as a temperature glide where they do not boil at constant temperature as pure substances do. The temperature glide effect is related to a substantially increased vapor dome and therefore a larger real gas effect over a larger temperature range. Figure 1.6 illustrates the maximum cooling capacity per unit of mass flow rate associated with pure nitrogen and a mixture of nitrogen, ethane, and methane; it is clear that the use of the three component mixture has increased the performance of the cycle. The reason is clear from examination of Figure 1.7 which shows the pressure enthalpy diagram for pure nitrogen (a) and the same mixture of nitrogen, ethane, and methane (b). The mixture has a vapor dome that encompasses a much broader range of temperature and therefore is a more attractive working fluid for use within a JT cycle.

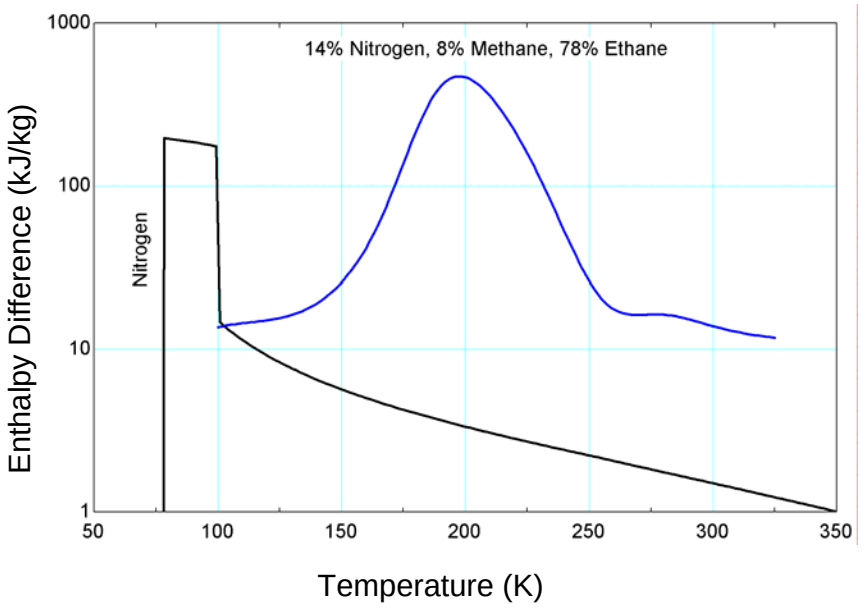

Figure 1.6: Enthalpy difference between 1000 kPa and 100 kPa (i.e., maximum cooling capacity per mass flow rate) as a function of temperature for nitrogen and a mixture of 14%N_2/8%CH_4/78%C_2H_6 (by mole).

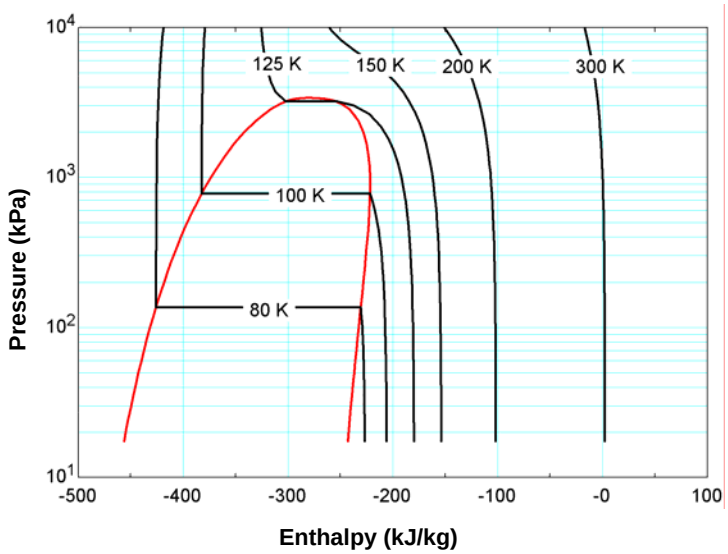

(a)

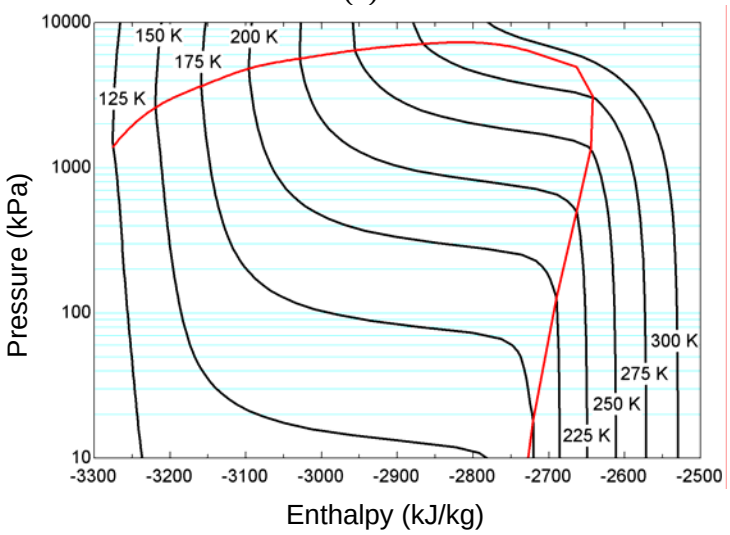

(b)

Figure 1.7: Pressure-enthalpy diagram for (a) pure nitrogen and (b) a mixture of 14%N_2/8%CH_4/78%C_2H_6 (by mole).

Since the 1970's, several researchers, including Little (1988), Boiarski et al, (1998), and Luo et al. (2000), have demonstrated that various gas mixtures exhibit an order of magnitude increase in thermodynamic efficiency relative to their single component counterparts. Mixed gas JT cycles have become attractive for many applications, including cooling of sensors (Rijpma et al, 2003), biomedical samples, and cryosurgical

probes (Naer,2002). Systematic techniques for optimizing the composition of a gas mixture for use in a JT cycle subject to a particular operating condition have been introduced by Keppler et al. (2004), Little (1997), Gong et al. (2002), and Alexeev et al. (1997).

Both Boiarski et al. (1998) and Gong et al. (2001) have measured the overall heat transfer coefficient for gas mixtures at cryogenic temperatures through the use of tube-in-tube and paired tube recuperative heat exchangers. However, measurement of the overall heat transfer coefficient data does not allow investigation of the specific mechanisms that drive the multi-phase, multi-component heat transfer. As part of this project, Nellis et al. (2005) provide a detailed and local measurement of the heat transfer coefficient for gas mixtures appropriate for very low temperature applications at cryogenic temperatures.

The nominal design requirements associated with this project include a target operating temperature below 100 K with a small cooling power, on the order of 100's of milliwatts. This combination of low power and low temperature is not typical and it was found in this work that there are some unique design features and issues that arise for these conditions. Most notably, the device requires very low flow rates and therefore the management of any small amount of liquid becomes critical. The work described in the literature is summarized here with these issues in mind.

Several MGJT systems employing the Hampson style heat exchanger have been designed, fabricated, and tested. Naer and Rozhentzsev (2001) discuss a system that uses

a mixture of isobutane, ethane, and methane (74.5%, 21%, 4.5%) in order to provide greater than 50 W at 170 K (more than 100x the refrigeration and at a temperature that is 70 K higher than our current project). The system operates at a discharge pressure of 1.25 MPa and a suction pressure of 0.17 MPa; the flow rate and the details of the expansion mechanism that was used are not reported. The system was not integrated with a vacuum facility but was encased in 0.08 m thick polyurethane. The quality of the mixture in the low pressure stream of the heat exchanger was reported to be 0.30. In the same paper, the researchers report the use of an auto cascade MGJT cycle with a single phase separator, in order to provide 1 W of cooling at 79 K for a cryosurgical device. The cool down time was less than 45 minutes. However, they do not comment on the feasibility of using a single stage MGJT to achieve similar performance.

Ng et al. (2002) describe test results for a 5.0 cm (2.0 inch) long Hampson style heat exchanger in an open cycle using high purity Argon (99.9995%). Test results are provided for two supply pressures, 14.0 and 18.0 MPa. The dimensions of the shell, mandrel, and capillary used in the tests are summarized in Table 1.1. The heat exchanger was insulated but not integrated with a vacuum facility.

Table 1.1: Dimensions of the heat exchanger described by Ng et al. (2000).

Dimension	Finned capillary	mandrel	Shell
ID	0.01181 in (0.3 mm)	0.09055 in (2.3 mm)	0.1772 in (4.5 mm)
OD	0.01969 in (0.5 mm)	0.09843 in (2.5 mm)	0.189 in (4.8 mm)

A steady state temperature of 110 K was achieved within 60 seconds of activation while accepting a 3.5 W heat load. The flow rates were 13 SLPM for the 18 MPa run and 10 SLPM for the 14 MPa run; these are consistent with the flow rates used in the demonstration device discussed subsequently. Ng. et al. (2000) also discuss a numerical model of the heat exchanger which is used to predict the temperature distribution of the mandrel, shell, and gas streams through the heat exchanger. The expansion mechanism used in the device is described as a "jet tube" located at the end of the capillary for the valve; however, no dimensions or discussion is provided.

Chien, Chen, and Chou (1996) performed open cycle experiments with high pressure (20.68 MPa) pure nitrogen (99.998%) and a dual orifice system comprised of a self regulating valve and a fixed orifice. The self regulating valve includes a bellows mechanism which is located within the mandrel (see Figure 1.8). The bellows contracts when it is cooled by the low pressure return stream, thereby closing the end of a valve stem against the flow opening. After cool down, the self regulating valve would become completely shut and the cold end temperature would rise, causing the valve to open and the system to cool down again.

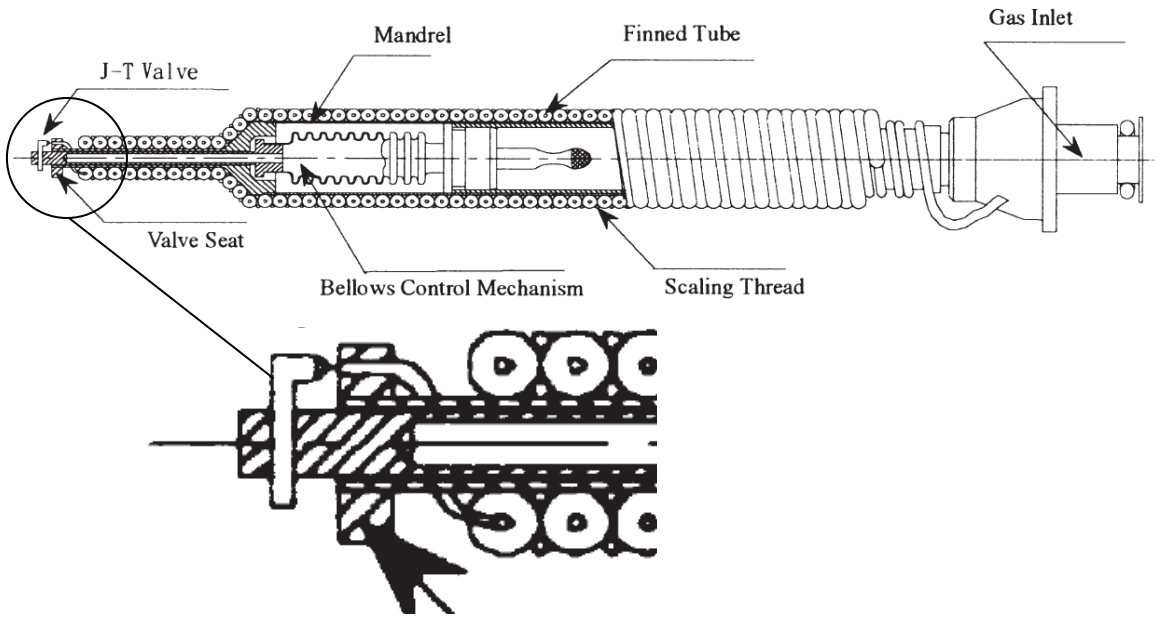

Figure 1.8: Schematic drawing of bellows control self-regulating JT cooler from Chien, Chen, and Chou (1996).

To circumvent this temperature oscillation, the expansion was switched to a fixed orifice of diameter 12 μm (0.0005 inch) which was installed in parallel with the self regulating valve . The flow rate through the fixed orifice was 0.01 g/s; this flow rate is consistent with the flows observed in this thesis, but at higher pressures and smaller orifice sizes. The researchers did not describe any liquid management issues with the pure nitrogen.

Papell et al. (1990) at the Nasa Lewis Research Center obtained mass flow rate, pressure drop, and temperature drop data for liquid and two phase nitrogen flowing through “visco jets” which are composed of several stages of multiple orifices that force the flow to change direction several times. By assembling these jets in series, it is possible to create a larger flow resistor without resorting to very small orifices that may become clogged. The more complex design (compared to a straight orifice) allows for the pressure drop to

be the same as a smaller straight orifice while employing larger orifice sizes, which are more easily manufactured. The fluid inlet pressures varied from 30 to 60 psia and the flow rates varied from 0.005 g/s to 0.5 g/s. During these tests, the two-phase, small mass flow rate runs experienced what was described as “partial blockage” which was attributed to gas contamination because the blockage was gone after the system warmed to room temperature. However, it is possible that the observed behavior was related to liquid management issues that are consistent with those described in this thesis.

1.3 Thesis Organization

Non-ideal working fluids are optimal for use in a JT cycle; therefore, the mixed gas working fluids used in a MGJT cycle will generally be two-phase throughout a large fraction of the heat exchanger and at the cold end. The formation of liquid in the cold end of the system has not been cited as a limitation to the development of previous systems; however previous systems typically operate at much larger flow rates or higher temperatures than the application discussed here and this may account for the lack of information in the literature regarding liquid management issues in MGJT devices. Conversations with engineers at PraxAir and Prometheus, companies that develop large scale MGJT systems for liquefaction of natural gas, have suggested that liquid management is an important issue in their design and that liquid can collect in locations where the vapor velocity is too small. This behavior is not reported formally in any paper that was reviewed here; however, these companies rarely publish such practical, proprietary information.

This thesis discusses the modeling and design of low power, low temperature MGJT systems and describes test results for an experimental device. The test results demonstrate that fluid management issues constrain the amount of liquid that can be permitted at a fixed orifice valve. This thesis discusses the experimental results that suggest this constraint.

In order to design the MGJT cycle, a gas mixture of nitrogen, methane, and ethane was optimized to provide the greatest cooling power per unit of conductance using the optimization model created by Keppler et al. (2004). A detailed model of the heat exchanger geometry was developed in order to predict the heat exchanger losses associated with a particular geometry; these losses include pressure drop, axial conduction through the heat exchanger, and heat transfer temperature difference for the specific Hampson-style geometry. The optimization model described by Keppler et al. (2004) was modified so that these heat exchanger losses are accounted for in the prediction of the cooling power.

Using this modeling tool, a Hampson-style heat exchanger was designed, fabricated and integrated with a thermal vacuum test facility, gas handling equipment, fixed orifice expansion valves, and appropriate instrumentation. The system was tested using high pressure (9.75 MPa) pure argon in an open cycle configuration in order to verify the test facility and the model under relatively simple operating conditions. Further experiments using gas mixtures were performed in a closed loop configuration. The test results with

gas mixtures illustrate the issues relative to liquid management that constrain the performance.

Chapter 2 Numerical Modeling

2.1 Mixture Selection

2.1.1 Mixture Properties

The thermophysical and transport properties of the candidate mixtures were obtained using the database "SUPERTRAPP Version 3" (also called NIST 4) [Ely and Huber, 2003]. NIST 4 provides thermodynamic properties for nearly 200 pure components and mixtures of up to 20 of these components. The database uses the Peng-Robinson equation of state to carry out the phase equilibrium calculations that are required to determine the liquid and vapor properties of the mixture. For all of the modeling done in this project, the properties for multiphase mixtures are obtained using the average of the properties of each phase combined by a vapor quality weighted sum.

The selection of optimal mixtures was performed using the optimization model developed by Keppler et al. (2004). This optimization model is implemented with EES (Engineering Equation Solver) [Klein, 2005] and is discussed in detail in the next section. The EES model obtains mixture properties from NIST4 using an interface program (EESNIST4). This interface program makes it possible to utilize the NIST 4 database in the context of larger models because calling the database is not substantially different than using an "internal procedure" within the EES environment.

Keppler et al. (2004) verified the NIST 4 results for a several mixtures against the results obtained from the NIST Database 23 (also known as "REFPROP") (Lemmon, et al

(2003)). REFPROP uses the Benedict-Webb-Rubin equation of state and Helmholtz-energy state equations in order to provide properties and therefore it is considered more accurate; however, it is also more computationally intensive and REFPROP has difficulty converging at temperatures below 150 K. For the conditions where REFPROP does converge, the two databases (NIST 4 and NIST 23) provide essentially the same thermodynamic property values over the range of pressures and temperatures that were investigated.

2.1.2 Optimization Model

In this section, the details of the optimization model developed by Keppler et al. (2004) are summarized in order to clarify the mixture selection process and simplify the description of the modifications that were made to the optimization model in order to apply it to this project, as discussed in section 2.2.

A schematic of the cycle is provided in Fig. 2.1. In order to identify the appropriate mixture for cooling the current leads of HTS electronics, the model must allow for the typical heat load concentrated at the cold end ($\dot{Q}_{load,cold}$) as well as a distributed heat load ($\dot{Q}_{load,dist}$). This requires an additional input for the cycle calculation which is the ratio of the distributed load to the cold load ($\dot{Q}_{load,dist} / \dot{Q}_{load.cold}$). The other required inputs are the high (discharge) and low (suction) pressure levels (P_{high} and P_{low}), the heat rejection temperature (T_3), and the cold load temperature (T_6). The composition of the working fluid, $\bar{y}$, is specified as a vector containing the molar concentration of the working fluid

for each of the *NC* components. The composition of the mixture is adjusted by the optimization algorithm in order to maximize the refrigeration per unit of heat exchanger conductance; note that other figures of merit such as theoretical efficiency or refrigeration per unit of flow rate can also be considered. A genetic optimization algorithm is used for this process; this optimization technique has been extensively investigated and shown to properly identify the global optimal composition, as discussed by Keppler et al. (2004).

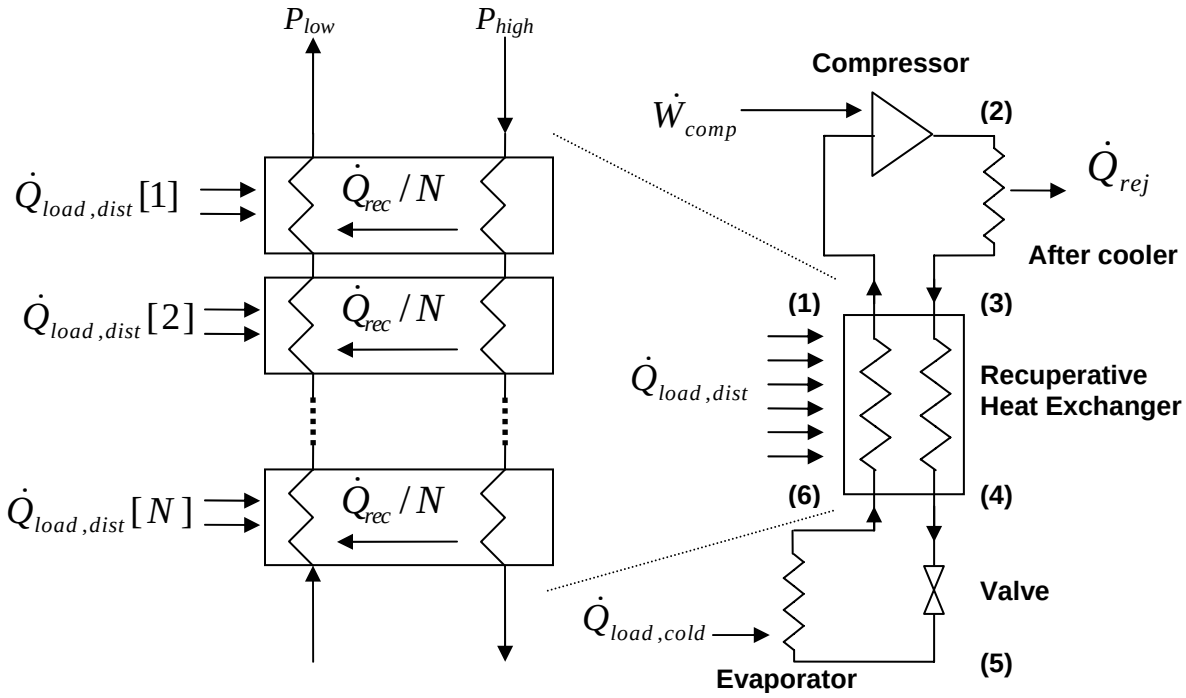

Figure 2.1: The recuperative heat exchanger broken into *N* segments of equal recuperative heat transfer.

The model begins by assuming a hot end temperature difference (ΔT, the difference between the hot inlet and cold exit temperature); this temperature difference is iteratively adjusted based on subsequent calculations until all of the equations described below are satisfied (EES handles this process automatically although it is often useful to set the hot end temperature difference in order to obtain a reasonable set of initial guess values for

the iteration). The temperature of the low pressure fluid leaving the heat exchanger (T_1) can be computed:

$$T_1 = T_3 - \Delta T_{hot} \tag{2.1}$$

The enthalpies of the working fluid at the hot inlet (h_3), cold inlet (h_6), and cold exit (h_1) are computed based on the known temperatures and pressures using the function *"enthalpy_TP"* which returns the molar enthalpy of a mixture at a specified temperature, pressure, and composition vector ($\bar{y}$) by calling the NIST 4 database.

$$h_1 = enthalpy\_TP[\bar{y}, T_1, P_{low}] \tag{2.2}$$

$$h_6 = enthalpy\_TP[\bar{y}, T_6, P_{low}] \tag{2.3}$$

$$h_3 = enthalpy\_TP[\bar{y}, T_3, P_{high}] \tag{2.4}$$

An energy balance on the cold stream provides a relationship between the stream-to-stream heat transfer in the heat exchanger per unit of mass flow rate ($\dot{Q}_{rec} / \dot{m}$) and the distributed load on the cycle per unit of mass flow rate ($\dot{Q}_{load,dist} / \dot{m}$):

$$\frac{\dot{Q}_{rec}}{\dot{m}} = h_1 - h_6 - \frac{\dot{Q}_{load,dist}}{\dot{m}} \tag{2.5}$$

The enthalpy of the hot exit flow (h_4) can be computed using an energy balance on the hot stream:

$$h_4 = h_3 - \frac{\dot{Q}_{rec}}{\dot{m}} \tag{2.6}$$

The enthalpy and pressure allow the hot exit temperature (T_4) to be obtained:

$$T_4 = temperature\_hP[\bar{y}, T_4, P_{high}] \tag{2.7}$$

where the function "*temperature_hP*" returns temperature given enthalpy and pressure, again using the NIST 4 database. An energy balance on the adiabatic expansion valve requires that the specific enthalpy at the valve exit (h_5) must equal the specific enthalpy at the valve inlet (h_4):

$$h_5 = h_4 \tag{2.8}$$

which allows the temperature of the fluid leaving the expansion valve (T_5) to be obtained:

$$T_5 = temperature\_hp[\bar{y}, h_5, P_{low}] \tag{2.9}$$

The refrigeration load concentrated at the cold end per unit mass flow rate is calculated:

$$\frac{\dot{Q}_{load,cold}}{\dot{m}} = h_6 - h_5 \tag{2.10}$$

The distributed load per unit mass flow rate is calculated based on the specified distributed-to-cold load ratio:

$$\frac{\dot{Q}_{load,dist}}{\dot{m}} = \max\left(0, \frac{\dot{Q}_{load,dist}}{\dot{Q}_{load,cold}} \frac{\dot{Q}_{cold,load}}{\dot{m}}\right) \tag{2.11}$$

where the use of the maximum function prevents the imposition of a non-physical, negative heat load (a distributed cooling effect).

Equations (2.1) through (2.11) allow for the simultaneous solution of the distributed and cold load based on the assumed temperature difference between the fluids at the hot end. The solution does not provide any information about the internal temperature distribution or the heat exchanger conductance (*UA*) that is required to achieve the assumed hot end temperature difference. The conductance is a particularly important heat exchanger

design parameter and provides a more physical input to the model than the hot end temperature difference; indeed, in some situations there may be positive but non-physical values of the hot end temperature difference which require the temperature distribution within the heat exchanger to "cross", resulting in the transfer of heat from cold to hot.

It is necessary to relate the conductance to the assumed hot end temperature difference; therefore, the heat exchanger is divided into a large (*N*) number of smaller heat exchangers that are each modeled as having constant properties. This discretization is depicted in Figure 2.1. The "size" of each control volume is dictated by requiring that the total recuperative heat exchange ($\dot{Q}_{rec}$) is divided equally among all *N* segments; thus, these are control volumes of equal recuperative heat transfer rather than of equal surface area or conductance. The energy balance on a differential segment of the heat exchanger is shown in Figure 2.2.

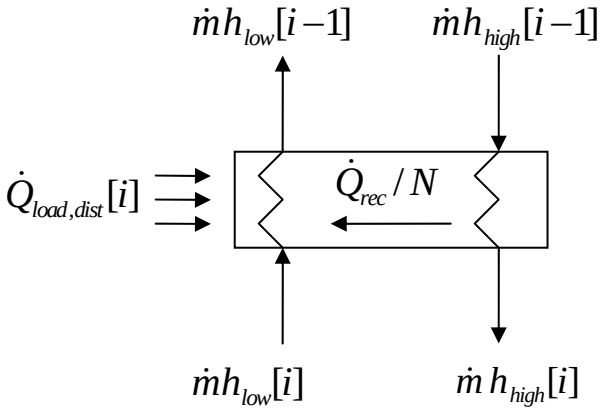

Figure 2.2: Differential energy balance on one heat exchanger segment.

The distributed load is assumed to be incident on the low pressure fluid; therefore, the enthalpy of the hot fluid leaving each differential element ($h_{high}[i]$) can be computed according to:

$$h_{high}[i] = h_{high}[i-1] - \frac{\dot{Q}_{rec}}{\dot{m}N} \quad i = 1...N \tag{2.12}$$

where $h_{high}[N]$ is the enthalpy of the high pressure fluid entering the heat exchanger (previously calculated as h_3). The enthalpy of the cold fluid entering each element ($h_{low}[i]$) can be computed according to:

$$h_{low}[i] = h_{low}[i-1] - \frac{\dot{Q}_{rec}}{\dot{m}N} - \frac{\dot{Q}_{load,dist}[i]}{\dot{m}} \quad i = 1...N \tag{2.13}$$

where $h_{low}[0]$ is the enthalpy of the low pressure fluid entering the heat exchanger (previously calculated as h_6). The distributed heat transfer rate is assumed to be distributed equally in each segment ($\dot{Q}_{load,dist}[i]$),

$$\dot{Q}_{load.dist}[i] = \frac{\dot{Q}_{load,dist}}{N} \tag{2.14}$$

Alternatively, the distributed heat load can be distributed according to heat exchanger conductance (i.e., those segments with larger conductance are assigned a larger amount of the total distributed heat load); this type of distribution is consistent with a spatially uniform heat flux,

$$\dot{Q}_{load,dist}[i] = \dot{Q}_{load,dist}\frac{dUA[i]}{UA} \tag{2.15}$$

where $dUA[i]$ is the amount of conductance required by the $i^{\underline{th}}$ segment, which will be determined subsequently (note that iteration is required to ensure that the spatial distribution of the distributed load and conductance are consistent).

The temperature distribution associated with the two streams can be obtained based on the enthalpy and pressures:

$$T_{high}[i] = temperature\_hP(\bar{y}, h_{high}[i], P_{high}) \quad i = 1...N \tag{2.16}$$

$$T_{low}[i] = temperature\_hP(\bar{y}, h_{low}[i], P_{low}) \quad i = 1...N \tag{2.17}$$

It is possible to model each of the individual heat exchanger segments using conventional ε-NTU type relations in order to estimate the differential conductance required by each segment ($dUA[i]$) and therefore, by integration, the total conductance required by the heat exchanger (UA). However, the conventional ε -NTU type relations that are reported in most text books do not permit a distributed parasitic load and therefore are not applicable to this problem. Therefore, the ε-NTU relationship associated with a counter-flow heat exchanger subjected to a uniform heat flux has been derived by Nellis and Pfotenhauer (2004) and is repeated below. The number of transfer units based on the hot side capacity ratio (NTU_{high}) is implicitly related to the temperatures entering and leaving the segment, the hot-to-cold capacity ratio (Cr), and the non-dimensional distributed heat load (χ_{low}) according to:

$$\Theta_{high}[i]=\left(NTU_{high}[i]\,\chi_{low}[i]+\frac{\left(Cr[i]-1\right)}{Cr[i]}\right)\frac{\left(Cr[i]-1\right)+Cr[i]\,\chi_{low}[i]\left(1-\exp\left(\left(Cr[i]-1\right)NTU_{high}[i]\right)\right)}{\frac{\left(Cr[i]-1\right)}{Cr[i]}\left(\exp\left(\left(Cr[i]-1\right)NTU_{high}[i]\right)-1\right)} \tag{2.18}$$

where

$$\Theta_{high}[i]=\frac{T_{high}[i-1]-T_{low}[i-1]}{T_{high}[i-1]-T_{low}[i]} \tag{2.19}$$

$$Cr[i]=\frac{\left(h_{high}[i-1]-h_{high}[i]\right)}{\left(h_{low}[i-1]-h_{low}[i]\right)}\frac{\left(T_{low}[i-1]-T_{low}[i]\right)}{\left(T_{high}[i-1]-T_{high}[i]\right)} \tag{2.20}$$

$$\chi_{low}[i]=\frac{\dot{Q}_{load,dist}[i]}{dUA[i]\left(T_{high}[i-1]-T_{low}[i]\right)} \tag{2.21}$$

The number of transfer units is related to the differential amount of conductance in each segment:

$$dUA[i]=NTU_{high}[i]\frac{\left(h_{high}[i-1]-h_{high}[i]\right)}{\left(T_{high}[i-1]-T_{high}[i]\right)}\dot{m} \tag{2.22}$$

The total conductance is the sum of the differential conductances ($dUA[i]$) calculated using Equation (2.22). Taken together, equations (2.1) through (2.22) allow various figures of merit to be computed for the cycle with a specified total conductance; for example, the coefficient of performance (COP) of the cycle (based on a reversible, isothermal compressor model) as well as the refrigeration (the total of the distributed and concentrated loads) per unit of mass flow rate can be computed. However, the most

appropriate optimization target for this application is the total refrigeration per unit of heat exchanger conductance ($\dot{Q}/UA$), since maximizing this target suggest the most compact refrigeration system. This target is important for a military application where the cooling system must ultimately be integrated into a limited geometric envelope and be, essentially, invisible to the end user.

There are additional considerations for the optimization. In order to be viable, the refrigerant mixture under consideration must not freeze anywhere in the cycle. Unfortunately, there is little published work regarding the freezing point of mixtures that are appropriate for a JT cycle and therefore it is necessary to develop an approximate method for constraining the optimization. In general, the freezing point of a mixture is lower than the mole fraction weighted linear average of the freezing points of its constituents; this phenomenon is referred to as freezing point depression. In the optimization model, the freezing point temperature of the mixture (T_{freeze}) is conservatively estimated according to be the mole fraction weighted average of the triple points of the various components ($T_{tp,i}$).

$$T_{freeze} = \sum_{i=1}^{NC} y_i \cdot T_{tp,i} \tag{2.23}$$

where y_i is the mole fraction of component i. If the temperature at the exit of the valve is less than this estimate of the freezing point temperature then the composition is excluded from further consideration (practically, the refrigeration potential is assigned a large, negative value). The freezing point constraint is conservative in that it likely excludes some viable mixtures that would not truly freeze due to freezing point depression.

There are additional constraints that may be added to the optimization model. For example, the carry-over of liquid to the suction of the compressor should be avoided. Subsequent work, presented later in this thesis and based on experimental observations, suggests that there is a relationship between the amount of liquid that can be tolerated within the heat exchanger and the vapor velocity; this relationship should be formalized and integrated with the optimization algorithm as an additional constraint.

2.1.3 Optimization

The purpose of this section is to describe the particular operating conditions that were used in order to find the optimal mixture that provides the basis of the design of the demonstration device, described in section 2.4. The first step in the optimization of the design mixture is the specification of the particular constituent components that will be included in the optimization process. Prior work has shown (e.g., Maytel et al. 2006) that the performance of a MGJT system is improved as the number of components is increased. This means that a smaller, more compact system (or one exhibiting higher performance) could be designed using a seven component mixture as opposed to a three component mixture. Although this decrease in size is desirable for an eventual, production device, it is likely that designing for a 7 component mixture would lead to a demonstration device that is undersized (i.e., has insufficient conductance) for the study of 3 component mixtures. Also, it is experimentally difficult to generate a 7 component mixture with any degree of tolerance. Therefore, a 3 component mixture including ethane, methane, and nitrogen was chosen for design; this choice was motivated by the

desire to have a simple mixture that could be explored experimentally with some precision. The operational pressures and temperatures are likewise chosen based on consideration of the experimental constraints. The discharge pressure from the compressor is selected using the operating limit of the APD compressor that is available for this project; note that lower cold end temperatures can theoretically be obtained with a given mixture by lowering the suction pressure of the compressor because the saturation temperature of each of the components is reduced when the pressure is lowered as shown in Figure 2.3. A suction pressure of 100 kPa is selected to avoid contamination problems related to air infiltration. The design conditions are summarized in Table 2.1.

Table 2.1: Design conditions.

Input Variable	**Value**
P_{high}	1700 kPa
P_{low}	100 kPa
T_3	300 K
component 1	nitrogen
component 2	methane
component 3	ethane

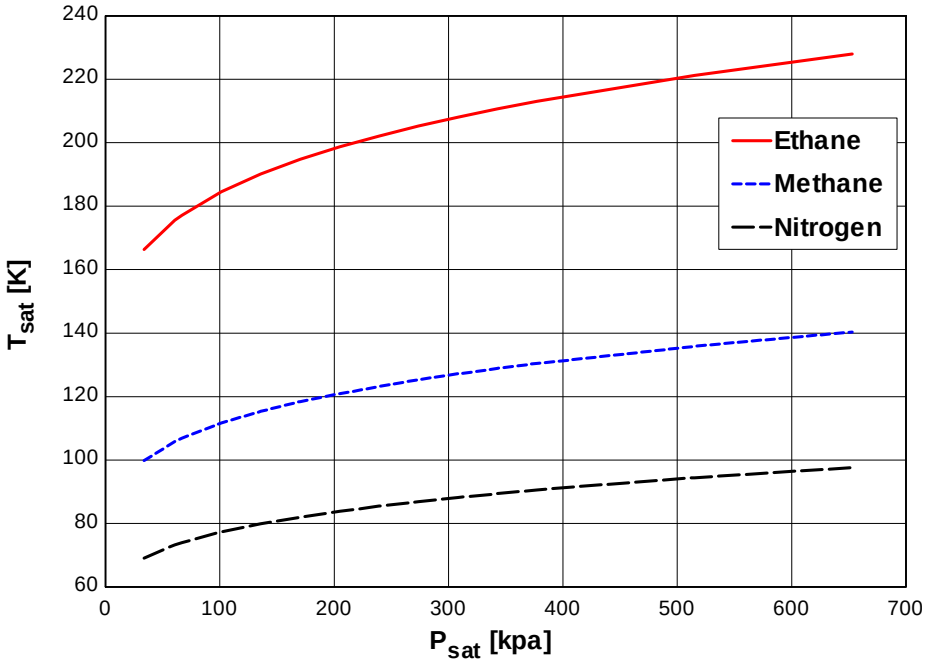

Figure 2.3: Saturation temperature of mixture components as a function of pressure.

The cold inlet temperature to the heat exchanger (T_6) is chosen to be 80 K to explore the very low temperature mixtures that are of primary interest for cooling high temperature superconducting electronics. The remaining inputs to the optimization process include the ratio of distributed load to cold end load ($\dot{Q}_{load,dist} / \dot{Q}_{load.cold}$) and the hot end temperature difference (ΔT) or, equivalently, the conductance of the heat exchanger per unit of mass flow rate ($UA/\dot{m}$).

To illustrate the influence of these variables on the selection of the optimum mixture, Figures 2.4 and 2.5 show the optimal mixture composition and the resulting performance, expressed as $\dot{Q}/UA$ (which was the optimization objective for these runs) as a function

of ΔT for $\dot{Q}_{load,dist} / \dot{Q}_{load.cold} = 1$ and $\dot{Q}_{load,dist} / \dot{Q}_{load.cold} = 0$, respectively; note that both Figures 2.4 and 2.5 use the design conditions shown in Table 2.1.

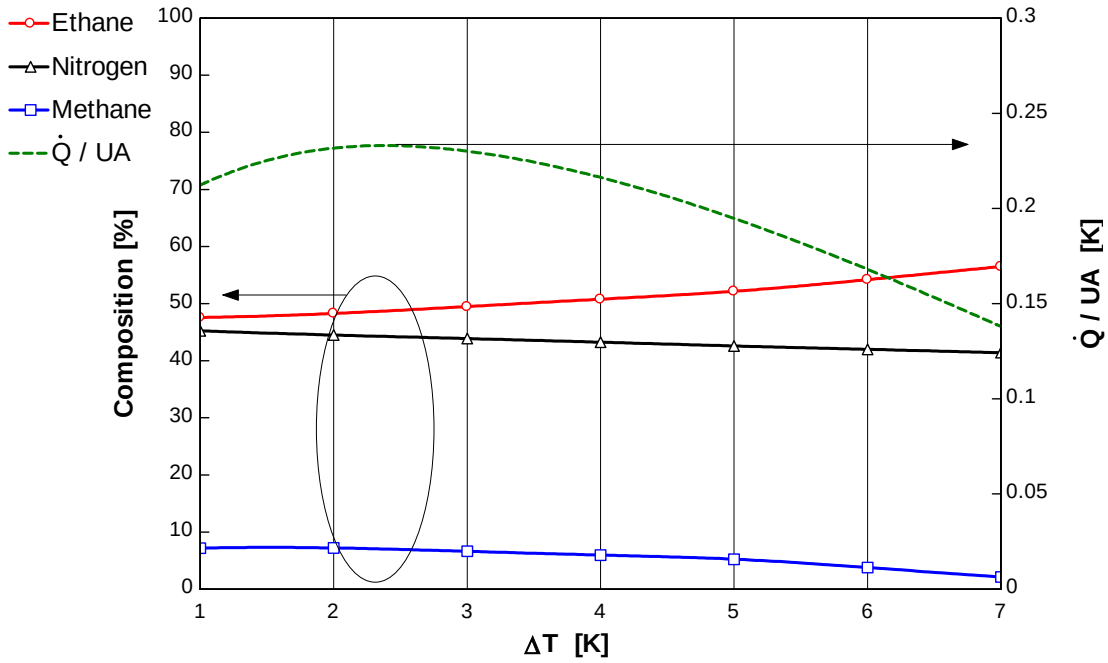

Figure 2.4: Optimal composition and refrigeration power per unit heat exchanger conductance for $\dot{Q}_{load,dist} / \dot{Q}_{load.cold} = 1$.

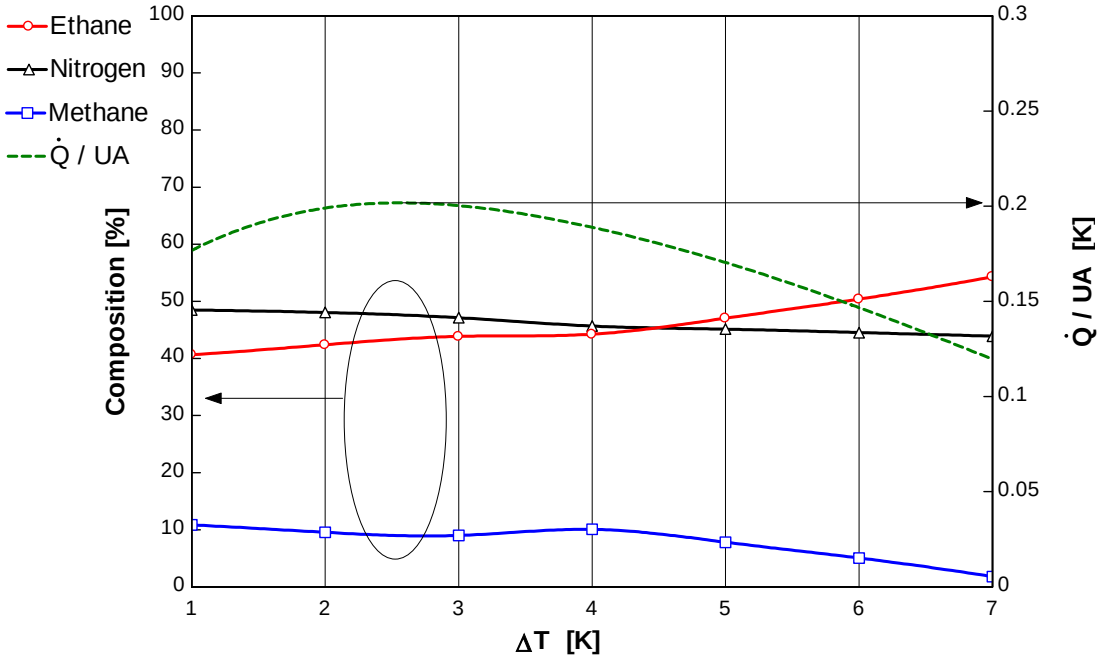

Figure 2.5: Optimal composition and refrigeration power per unit heat exchanger conductance for $\dot{Q}_{load,dist} / \dot{Q}_{load.cold} = 0$.

Notice that the optimal composition with respect to the variable ΔT occurs at a hot end temperature difference between 2 and 3 K. At first, this seems contrary to intuition since we know that the refrigeration per mass flow rate is a linearly decreasing function of hot end temperature difference (with a perfect recuperator providing the maximum refrigeration as ΔT approaches 0 K). However, a system with a small ΔT will require a larger heat exchanger (as ΔT approaches zero, the conductance will become infinite) and is therefore not the most compact system (although it may be the most efficient system). Therefore, above some value of conductance (i.e., below some value of ΔT) there is a diminishing incentive (in terms of $\dot{Q}/UA$) to bring the temperatures of the streams closer together.

The refrigeration capacity per unit conductance for the two ratios of distributed to concentrated loads are shown together in Fig. 2.6; the percent improvement associated with accepting 50% of the load over a distributed temperature range is approximately 15% and is relatively unaffected by the value of ΔT as shown in Fig. 2.6.

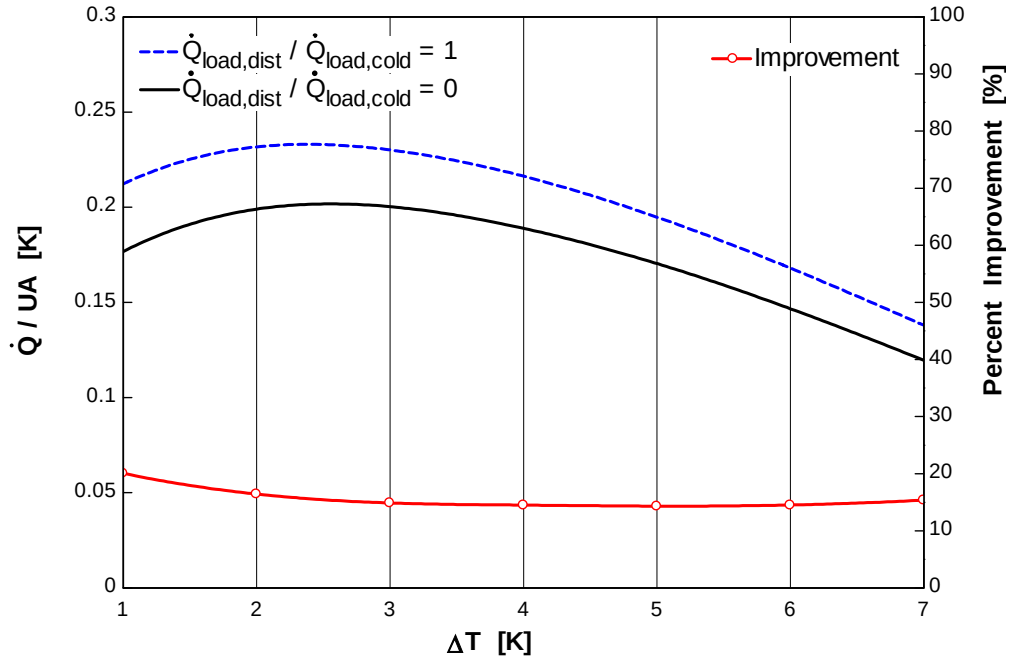

Figure 2.6: The refrigeration capacity per unit of conductance associated with receiving half of the total heat load in a distributed fashion is 15%, on average, over a wide range of ΔT.

The minimum cycle temperature (T_5) and the refrigeration per unit of mass flow rate for the optimal mixtures are shown in Figures 2.7 and 2.8.

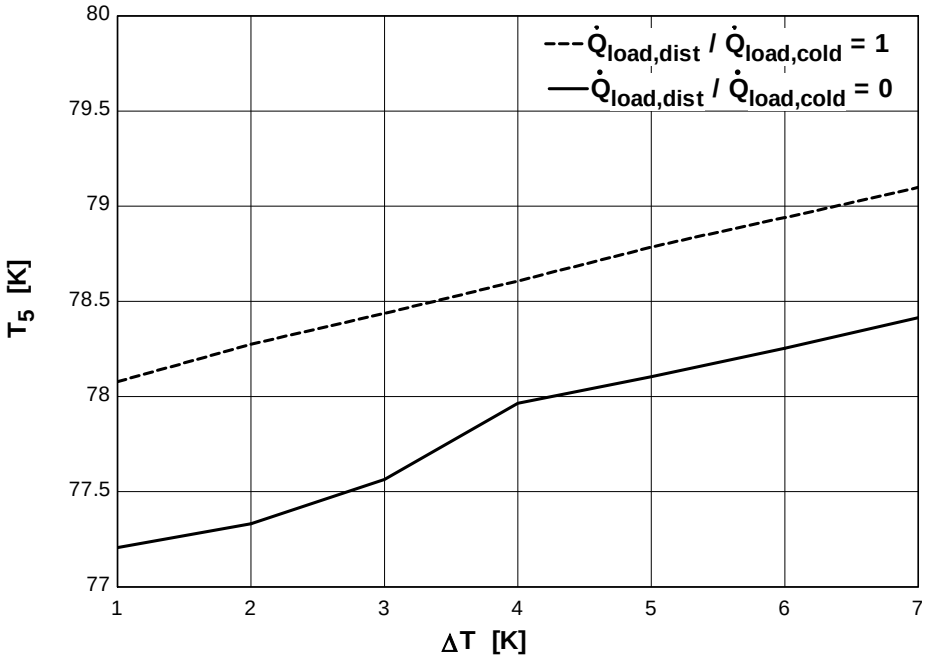

Figure 2.7: The minimum cycle temperature for the optimal mixtures found for $\dot{Q}_{load,dist} / \dot{Q}_{load.cold} = 0$ and $\dot{Q}_{load,dist} / \dot{Q}_{load.cold} = 1$.

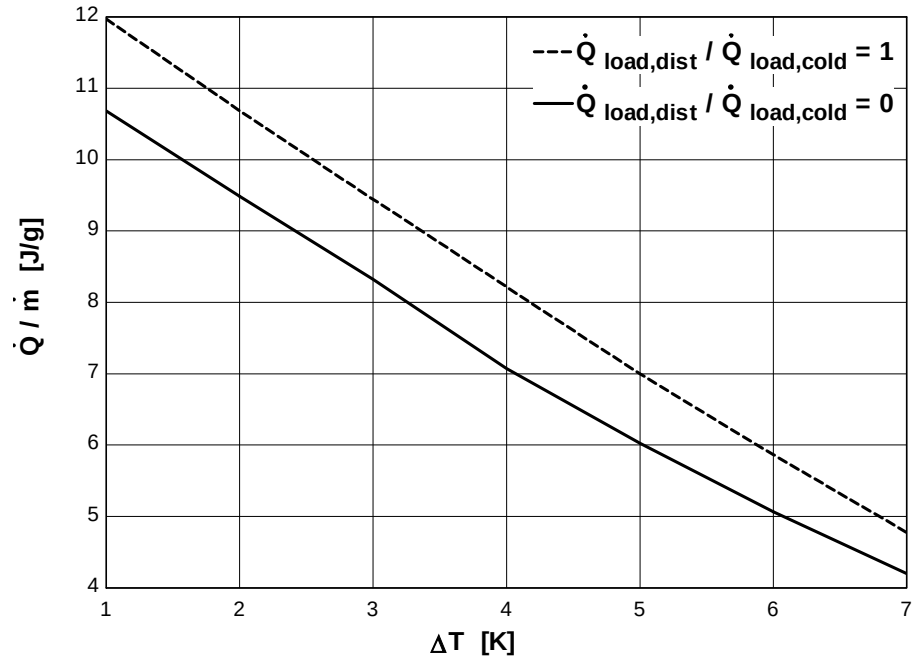

Figure 2.8: The refrigeration power per unit of mass flow rate for the optimal mixtures found for $\dot{Q}_{load,dist} / \dot{Q}_{load.cold} = 0$ and $\dot{Q}_{load,dist} / \dot{Q}_{load.cold} = 1$.

Figure 2.8 shows the motivation for selecting $\dot{Q}/UA$ as opposed to $\dot{Q}/\dot{m}$ as the figure of merit for the optimization process; $\dot{Q}/UA$ has a clear optimal value that is associated with a reasonable size of heat exchanger whereas $\dot{Q}/\dot{m}$ would inevitably push the optimization towards an infinitely large heat exchanger. It is interesting that the distributed case has a higher refrigeration capacity but operates at a slightly higher temperature at the entrance to the evaporator (T_5). This result is due to the fact that the distributed case only needs to remove half of the total refrigeration load at the cold end. The other half is removed at higher temperatures using the cold stream of the recuperator. Therefore, the temperature change from T_5 to T_6 (i.e., across the load heat exchanger which is sometimes called the evaporator) is smaller.

It is important to point out that the optimal mixtures shown in Figures 2.4 and 2.5 freeze at temperatures that essentially lie exactly on the line of minimum cycle temperatures shown in Figure 2.7 (according to the freeze criteria of equation (2.23)). This indicates that the freeze constraint in some way dominates the optimization process and those mixtures which are the highest performing are also nearest to this constraint. Even though the conservative nature of the freezing criteria in Equation (2.23) provides some protection against freezing (because of freezing point depression), the process of building the mixture introduces some uncertainty in the concentration of the mixture. As a precaution against the possibility that the introduction of an off-design composition (due to experimental uncertainties) will lead to freezing, a less optimal design mixture was chosen that would not freeze (again, according to Eq.(2.23)) over a wider range of the

composition that corresponds to the limits of the expected experimental uncertainty associated with building the mixture. The expected range was estimated using the results of previous research which utilized the same gas handling equipment [Hughes, 2004]. To obtain this "freeze-tolerant" mixture, the optimization was performed with the freeze temperature constraint increased by 3 K relative to the coldest point in the cycle (the same operating conditions were assumed otherwise). The design mixture, uncertainties, and operating conditions that were chosen are summarized in Table 2.2.

Table 2.2: Allowable composition variation and new operating conditions for a "freeze-tolerant" mixture.

Design Mixture	**Composition**	**Estimated Uncertainty**	**Operating Conditions**	
Nitrogen	39%	± 2 %	P_{high}	1700 kPa
Methane	6%	± 3 %	P_{low}	100 kPa
Ethane	55%	± 3 %	T_3	300 K
			T_6	85 K

In order for the refrigeration capacity of the "freeze-tolerant" mixture to be comparable to the mixtures that were shown in Figures 2.4 and 2.5 (which are not "freeze-tolerant") it was found that the system must operate at a somewhat higher cold inlet temperature of T_6=85 K. The lowest cycle temperature (T_5) is shown in Figure 2.9 for the distributed and concentrated heat loads.

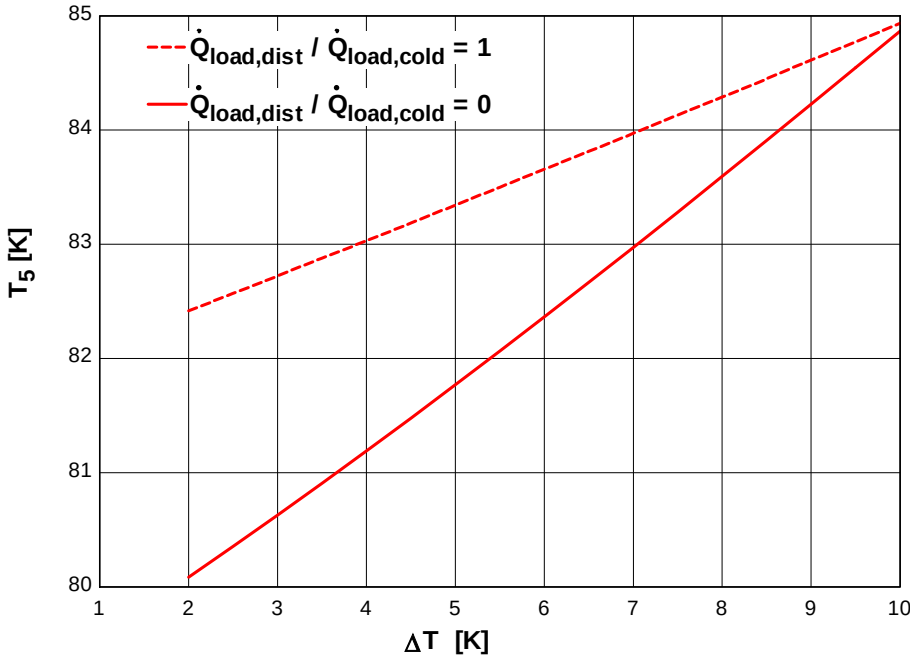

Figure 2.9: Minimum cycle temperature for the "freeze-tolerant" mixture in Table 2.2.

Figure 2.10 illustrates the $\dot{Q}/UA$ for the "freeze-tolerant" mixture as a function of the hot-end temperature difference for the two ratios of distributed to concentrated load. Note that the improvement in performance associated with accepting a distributed heat load is less for the "freeze-tolerance" mixture and is significant only for ΔT less than approximately 3 K.

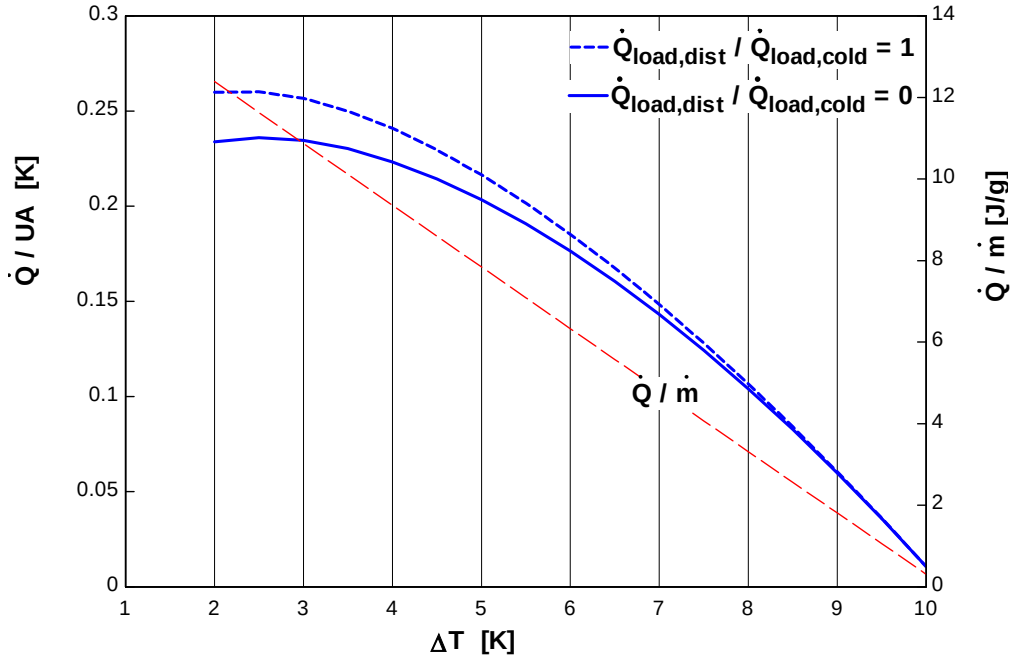

Figure 2.10: Refrigeration per unit of heat exchanger conductance for the design mixture and the operating conditions of Table 2.2. The refrigeration per unit mass flow rate ($\dot{Q}/\dot{m}$) is the same for both modes of receiving the heat load.

The conductance per unit mass flow rate that is required to achieve the cooling indicated in Figure 2.10 is shown in Figure 2.11.

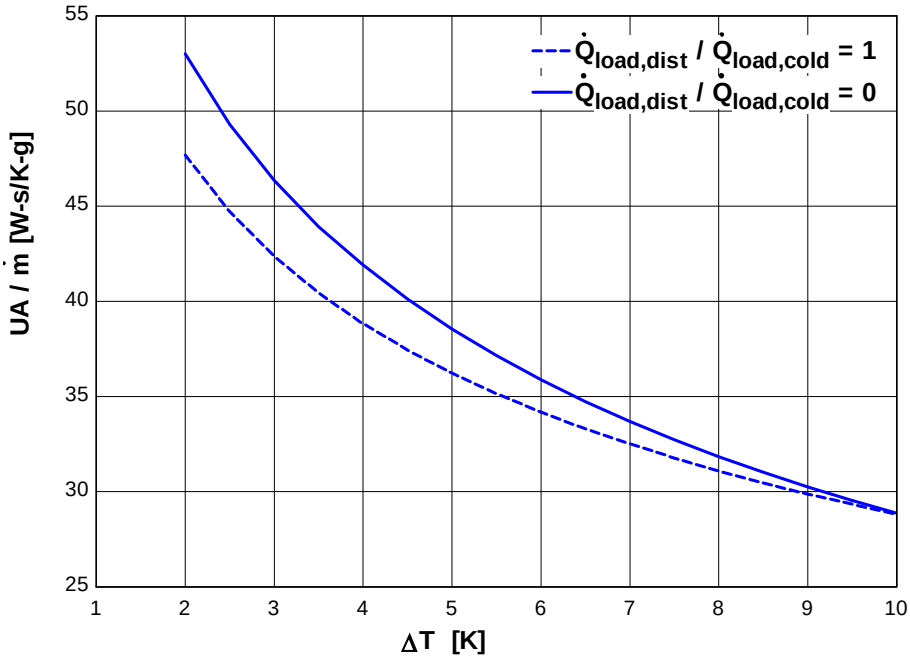

Figure 2.11: Required heat exchanger conductance per unit mass flow rate as a function of hot end temperature difference.

2.2 Cycle Performance Model

Section 2.1 provides an estimate of the optimal mixture composition for the design conditions as well as the likely performance, specifically the required conductance and mass flow rate. In order to design a heat exchanger around these requirements, both a cycle performance model and detailed design model were developed. The basis for the cycle performance model was the optimization model that was previously described; the optimization code is not used for optimization of the composition but rather to predict the cycle characteristics given a mixture. The code is modified in order to account for the effect of the heat exchanger loss characteristics (e.g., the pressure drop on the hot side) on the cycle performance; the heat exchanger losses themselves are predicted using a separate, detailed model of the heat exchanger geometry (which is described in section 2.3) and these loss characteristics are input into the cycle performance model which predicts the refrigeration capacity. Therefore, the inputs for the cycle performance model include the conductance of a candidate geometry (UA_{spec}), the mass flow rate ($\dot{m}$), the pressure drop in the high and low pressure streams (DP_{HP} and DP_{LP}), and the axial resistance to heat transfer through the heat exchanger (R_{axial}).

The cycle performance model performs essentially the same calculations previously described in section 2.2 for the optimization model. However, the cycle performance model does not optimize the composition to maximize $\dot{Q}/UA$ but rather achieves conditions that are consistent with the calculated conductance by adjusting the assumed hot end temperature difference. That is, the input variable ΔT is adjusted in order to minimize the error between the actual and required conductance (UA_{spec} and UA):

$$err = \frac{\left|UA_{spec} - UA\right|}{UA_{spec}} \tag{2.24}$$

Since there is a single, well behaved optimization variable, ΔT, the optimization process is straightforward and a more direct algorithm can be used (the golden section search technique as opposed to the genetic method).

The pressure drop is included in the cycle calculations by assuming that the pressure drop in the heat exchanger acts only to reduce the operational pressures (this is a conservative approach, essentially assuming that the entire pressure drop occurs external to the heat exchanger),

$$P_{high} = P_{inlet} - DP_{HP} \tag{2.25}$$

$$P_{low} = P_{outlet} - DP_{LP} \tag{2.26}$$

The predicted rate of axial conduction through the heat exchanger can be computed based on the temperature span of the cycle and the thermal resistance to axial conduction,

$$\dot{Q}_{cond} = \frac{\left(T_3 - T_6\right)}{R_{axial}} \tag{2.27}$$

The axially conducted heat transfer is debited from the refrigeration predicted by the model.

The cycle performance model is formulated so that the heat exchanger losses are accounted for in a conservative manner (that is the actual performance should theoretically be somewhat better than predicted given a set of loss characteristics). The modeling methodology is generic and can be applied to any heat exchanger geometry.

The final step in the design of the MGJT system is to develop a modeling tool capable of predicting heat exchanger losses for a specific geometry.

2.3 Detailed Model of Heat Exchanger Geometry

2.3.1 Description of Geometry

The heat exchanger geometry selected for this project is the Hampson configuration that is frequently used in JT cycles. The Hampson heat exchanger consists of two concentric tubes (the outer tube is the shell and the inner is the mandrel) with a third tube wrapped helically around the inner tube (the mandrel). This geometry is depicted in Figure 2.12. Typically, the helically wound tube is finned in order to increase the heat transfer area. All of the designs considered in this project involve finned, helically wound tubes and therefore the helically wound tube will subsequently be referred to as the "finned tube"; variables that are associated with this tube are given the subscript "*ft*". A cross-sectional view of a Hampson heat exchanger (looking along the axis of the centerline) with a finned tube is shown in Figure 2.13; the important geometric variables that are subsequently used in the detailed model are indicated.

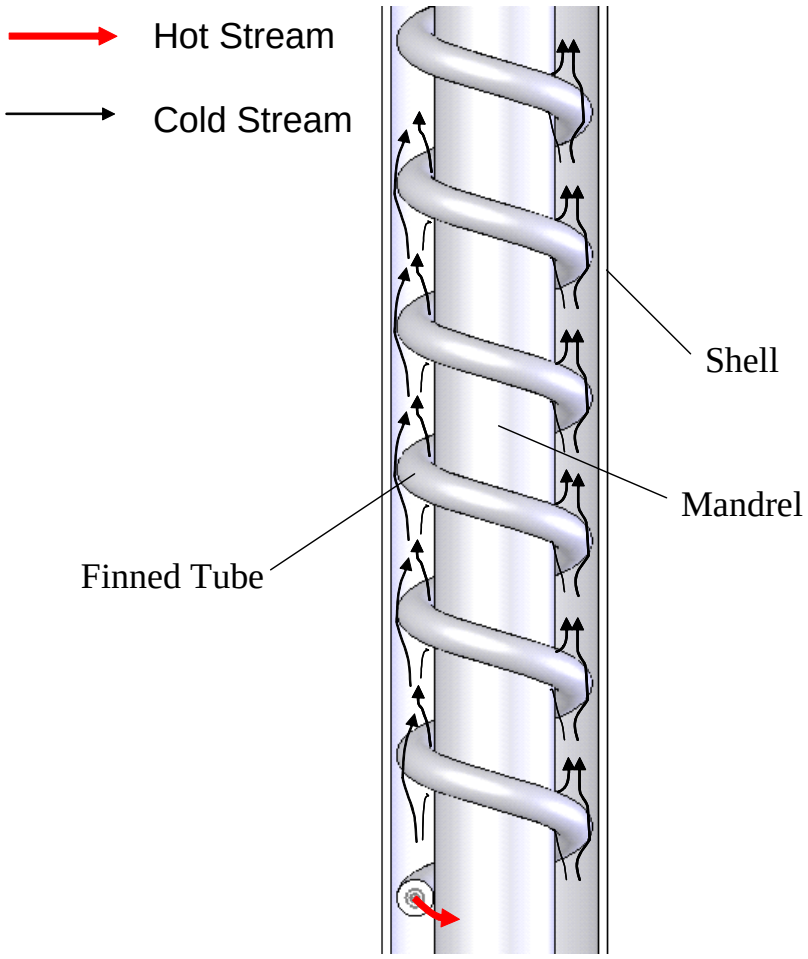

Figure 2.12: Hampson style heat exchanger. The mandrel and shell act only as support structures and pressure barriers; only the helically wound tube (i.e. the finned tube in the figure, although the fins are not shown) provides heat transfer area.

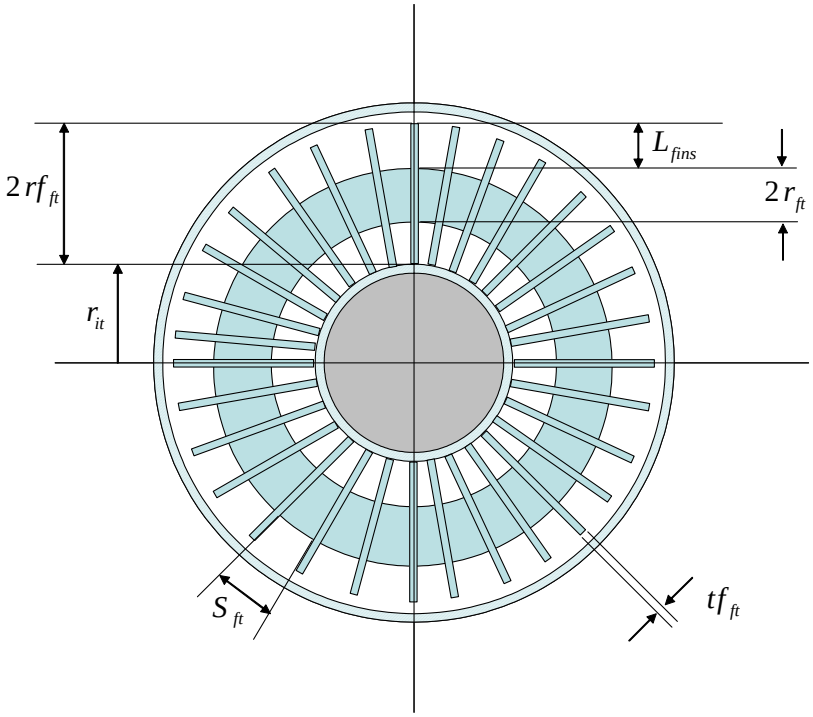

Figure 2.13: Cross-sectional view (along the axis) of a Hampson style heat exchanger. The low pressure stream travels through the array of fins presented by the finned tube while the high pressure stream is carried by the tube itself.

2.3.2 Heat Exchanger Calculation

It is necessary to account for the large variation in the properties of the working fluid and the heat exchanger material that are driven by the large temperature difference spanned by the heat exchanger. Therefore, the detailed model discretizes the overall length of the heat exchanger by dividing it into equal length segments. The model assumes (and never iterates on this assumption) that a linear temperature distribution exists in both streams from the hot end temperature (T_3) to the cold end (T_6) and uses this temperature distribution to compute the properties that are used to model each section.

$$L_{ot}[i] = \frac{L_{ot,t}}{M}$$

$$T_c[i] = T_h[i] = T_3 - i(T_3 - T_6) \quad i = 0..M \tag{2.28}$$

where $L_{ot,t}$ is the total length of the outer tube (or shell) and M is the number of heat exchanger segments. The length of the inner tube is assumed to be the same as the outer tube. The length of the inner tube together with the desired pitch of the helix is sufficient to calculate the length of the finned tube (or, given the pitch and the finned tube length, the required length of the inner tube can be found). The equation used to compute the length of the helically wound tube was verified against the results obtained from a 3-D CAD model of a helically wound tube.

The total conductance of the heat exchanger (UA) is the sum of the conductance of each heat exchanger segment ($UA[i]$) which is inversely related to the total resistance to heat transfer between the hot and cold streams ($R_{tot}[i]$),

$$UA[i] = \frac{1}{R_{tot}[i]} \tag{2.29}$$

The thermal resistances that together contribute to $R_{tot}[i]$ include the convective resistance between the cold stream and the finned surface ($R_c[i]$), the conductive resistance of the finned tube wall ($R_{cond}[i]$), and the convective resistance between the hot stream and the internal surface of the finned tube ($R_h[i]$). These are indicated in Equations (2.30) to (2.32) and illustrated in Figure 2.14 in the form of a thermal resistive circuit.

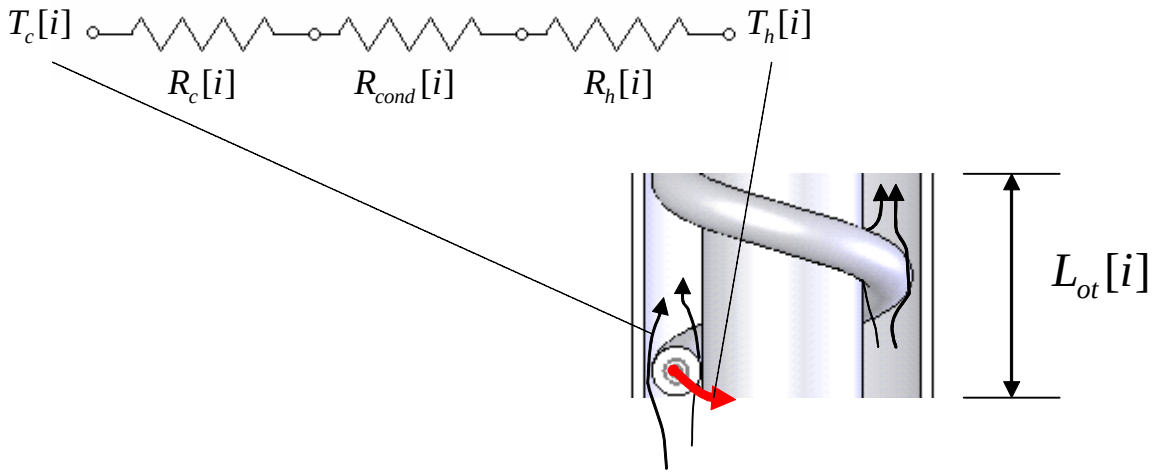

Figure 2.14: Resistance network for the ith control volume.

$$R_c[i] = \frac{1}{\eta_o[i]\, htc_c[i]\, A_t[i]} \tag{2.30}$$

$$R_{cond}[i] = \frac{\ln\left(r_{ft} / r_{ft,inner}\right)}{2\pi\, k_{ft}[i]\, L_{ft}[i]} \tag{2.31}$$

$$R_h[i] = \frac{1}{htc_h[i]\, A_h[i]} \tag{2.32}$$

where $A_h[i]$ is the inner surface area of the finned tube that is in contact with the hot fluid and $A_t[i]$ is the total outer surface area of the finned tube that is in contact with the cold stream.

$$A_h[i] = \pi\, (2\, r_{ft,innner})\, L_{ft}[i] \tag{2.33}$$

$$A_t[i] = N_{fins}[i]\, A_f + A_b[i] \tag{2.34}$$

where $N_{fins}[i]$ is the number of fins in the i^{th} section of finned tube. The inner and outer radii of the finned tube are $r_{ft,inner}$ and r_{ft} (not including the fins), and the length of the

finned tube in each segment is $L_{ft}[i]$. The thermal conductivity of the finned tube material is $k_{ft}[i]$.

The calculation of the heat transfer coefficients for the hot ($htc_h[i]$) and cold streams ($htc_c[i]$) is discussed in section 2.3.3. The overall surface efficiency of the finned tube, $\eta_o[i]$, is described in Incropera and DeWitt (2002) and represents the efficiency of the array of fins on the finned tube.

$$\eta_o[i] = 1 - N_{fins}[i]\left(\frac{A_f}{A_t[i]}\right)(1-\eta_f[i]) \tag{2.35}$$

where A_f is the surface area of an individual fin:

$$A_f = 2\left[\pi(rf_{ft}^{\,2} - r_{ft}^{\,2})\right] \tag{2.36}$$

where rf_{ft} is the outer radius of the fins on the finned tube. The parameter $A_b[i]$ that appears in the computation of the total surface area, Eq. (2.34), is the surface area of the exposed base of the finned tube that lies between adjacent fins.

$$A_b[i] = S_{ft}\,\pi\,(2r_{ft})(N_{fins}[i]-1) \tag{2.37}$$

where S_{ft} is the finned tube pitch. The adiabatic tip fin efficiency, $\eta_f[i]$, also described in Incropera and DeWitt (2002), is a function of fin material, geometry, and heat transfer coefficient ($htc_c[i]$):

$$\eta_f[i] = \frac{2r_{ft}}{m[i](rf_{ft}^{\,2} - r_{ft}^{\,2})}\left(\frac{K_1(m[i]r_{ft})\ I_1(m[i]rf_{ft}) - I_1(m[i]r_{ft})\ K_1(m[i]rf_{ft})}{I_o(m[i]r_{ft})\ K_1(m[i]rf_{ft}) + K_o(m[i]r_{ft})\ I_1(m[i]rf_{ft})}\right) \tag{2.38}$$

$$m[i] = \frac{2htc_c[i]}{k_{ft}[i]\,tf_{ft}} \tag{2.39}$$

where $K_0(x)$ and $K_1(x)$ are the value of *zero*-order and *first*-order Modified Bessel functions of the second kind, and $I_0(x)$ and $I_1(x)$ are *zero*-order and *first*-order Modified Bessel functions of the first kind.

The thermal conductivity of the finned tube material ($k_{ft}[i]$) is a function of temperature for the operating temperature range of the heat exchanger. Correlations for the thermal conductivity of several finned tube materials at cryogenic temperatures are obtained from NIST (Marquardt et. al., 2000), and are expressed in the form,

$$\begin{aligned}\log_{10} k = a + b(\log_{10} T) + c(\log_{10} T)^2 + d(\log_{10} T)^3 + e(\log_{10} T)^4 + f(\log_{10} T)^5 \\ + g(\log_{10} T)^6 + h(\log_{10} T)^7 + j(\log_{10} T)^8\end{aligned} \tag{2.40}$$

The accuracy of the correlation is reported to be at least 2% for most materials in the database. The thermal conductivity of OFHC Copper on the other hand varies based on its alloy as indicated by the residual resistivity ratio (RRR) value. To make an estimation of the thermal conductivity of the copper irregardless of its RRR value, an average formulation is employed. The equation for the average formulation has a slightly different form.

$$Log_{10}(k) = \frac{a + cT^{0.5} + eT + gT^{1.5} + iT^2}{1 + bT^{0.5} + dT + fT^{1.5} + hT^2} \tag{2.41}$$

The coefficients for some of the materials in the database are given in Table 2.3 and plotted in Figure 2.15. For both Eq. (2.40) and (2.41), the temperature units are [K] and the thermal conductivity is in [W/m-K].

Table 2.3: Experimental coefficients for thermal conductivity.

Coefficients	304 Stainless Steel	6061 Aluminum		Copper (OFHC)
a	-1.4087	0.07981		2.2154E0
b	1.3982	1.0957		-4.7461E-1
c	0.2543	-0.07277		-8.8068E-1
d	-0.6260	0.08084		1.3871E-1
e	0.2334	0.02803		2.9505E-1
f	0.4256	-0.09464		-2.0430E-2
g	-0.4658	0.04179		-4.8310E-2
h	0.1650	-0.00571		1.2810E-3
i	-0.0199	0		3.207E-3
Data range	1-300 K	1-300 K		4-300 K
Percent error	2%	0.5		n/a

The percent change of the various alloys relative to their room temperature values are shown in Figure 2.16.

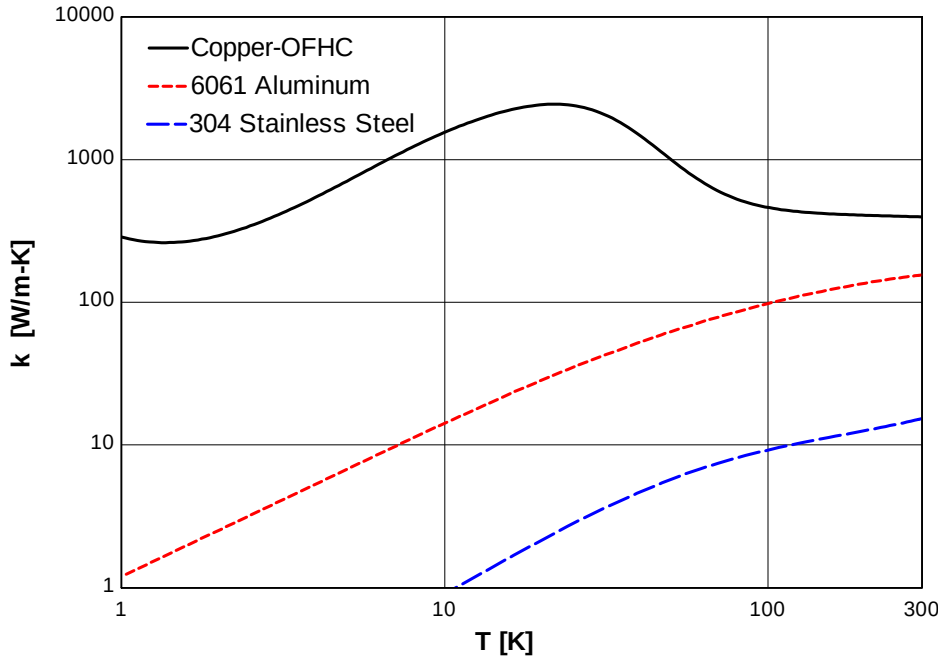

Figure 2.15: Thermal conductivity as a function of temperature.

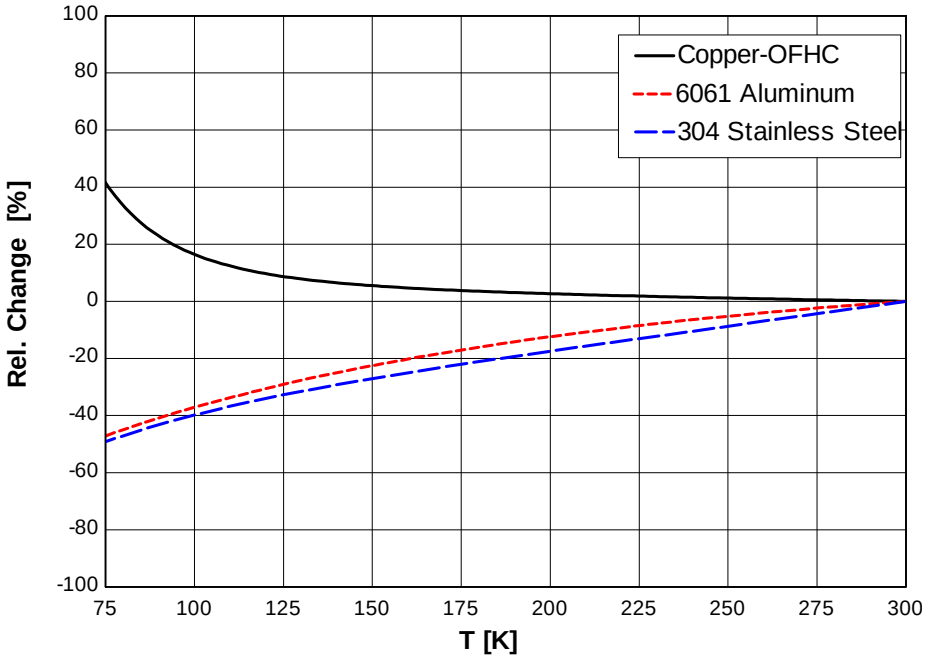

Figure 2.16: Percent change between the thermal conductivity at 300 K and the thermal conductivity at lower temperatures.

Note that the thermal conductivity of Copper-OFHC increases at cryogenic temperatures while the conductivity of 6061 Aluminum and 304 Stainless Steel decreases. The material database available from NIST does not include property information for the Copper-Nickel-715 that is used to manufacture the finned tube used in this project. The thermal conductivity of the Copper-Nickel alloy at 300 K is reported to be 29 [W/m-K] by the MATWEB online resource (2006) and this value is used in the model regardless of temperature; however, this approximation introduces some error as it is likely that the conductivity of the alloy will decrease with temperature.

The total resistance to heat transfer ($R_{tot}[i]$) in each segment is the sum of each of the components of the resistance network ($R_h[i]$, $R_{cond}[i]$, and $R_c[i]$); therefore, the largest resistances contribute most significantly to the overall total resistance. The largest

resistance is typically $R_c[i]$, followed by $R_h[i]$, and then finally $R_{cond}[i]$. The magnitude of $R_c[i]$ explains why the helical tube is typically finned in order to decrease the convection resistance between the cold fluid and the helical tube. Also, because $R_{cond}[i]$ contributes negligibly to the overall resistance it is not imperative that the conductivity of the material be known precisely. Therefore, although the thermal conductivity of the finned tube is not represented as accurately as the thermal conductivity of the inner and outer tubes (which were made from 304 stainless steel for all of the devices), the resulting error in the performance prediction is small.

2.3.3 Heat Transfer Prediction

As was mentioned previously, optimal mixtures exhibit two-phase behavior over essentially the entire temperature range of the system, therefore the convection heat transfer of the hot and cold streams will be enhanced by the boiling two phase mixture. Rather than pursuing a model of the two-phase heat transfer situation, the single phase correlations available from the literature are used with some modification; this approach is thought to be conservative. Because of the modular nature of the model, more precise heat transfer coefficient information can be integrated with the model, for example the measurements discussed by Hughes (2004), in order to achieve greater experimental agreement. The correlations listed in Tables 2.4 and 2.5 are recommended by Timmerhaus and Flynn (1989) for turbulent flow and by Incropera and DeWitt (2002) for laminar flow.

Table 2.4: Single-phase heat transfer for the i^{th} segment of the hot stream.

Geometry	Flow	Nusselt Number
Helical tube (Hot stream)	*Re < 2,300* (Laminar)	$Nu_h[i] = 3.66$ (assume constant temperature walls)
	Re > 2,300 (Turbulent)	$Nu_h[i] = \dfrac{\left(0.023\, Re_h[i]^{-0.2}\left(1+3.5\dfrac{ID_{ft}}{D_{helix}}\right)G_h\ cp_h[i]\, Pr_h[i]^{\frac{-2}{3}}\right)ID_{ft}}{k_h[i]}$
$Re_h[i] = \dfrac{G_h\ ID_{ft}}{\mu_h[i]}$		$G_h = \dfrac{\dot{m}}{A_{ff,h}}$ $\quad D_{helix} = 2\left(r_{it} + 2rf_{ft}\right)$ $\quad A_{ff,\,h} = \pi\left(\dfrac{ID_{ft}}{2}\right)^2$ $\quad Pr_h[i] = \dfrac{\mu_h[i]\, cp_h[i]}{k_h[i]}$

The Nusselt number of the hot stream ($Nu_h[i]$) is a function of the thermal properties of the mixture, the mass flux (G_h), Reynolds number ($Re[i]$), Prandtl number ($Pr[i]$), inner diameter of the helical tube (ID_{ft}), and the diameter of the helical path (D_{helix}) that the finned tube follows. The $1 + 3.5(ID_{ft}/D_{helix})$ term within the numerator of the turbulent flow correlation accounts for the increase in the heat transfer that is related to longitudinal vortices created by tight turning helical tubes [Incropera and DeWitt (2002)]. If the diameter of the helix is very large then this effect becomes negligible.

The correlations for the cold stream Nusselt number ($Nu_c[i]$) are similar to those of the hot stream; however, the area term required to compute the mass flux (G_c) is more complicated due to the complex geometry on the low-pressure side.

Table 2.5: Single-phase heat transfer for the i^{th} segment of the cold stream.

Geometry Type	Flow	Nusselt Number
Bank of in-line Tubes (Cold stream)	*Re < 2,300* (Laminar)	$Nu_c[i] = 3.66$ (assume constant temperature walls)
	Re > 2,300 (Turbulent)	$Nu_c[i] = \dfrac{0.26\, Re_c[i]^{-0.4}\, G_c\, cp_c[i]\, Pr_c[i]^{-\frac{2}{3}}\, D_{eff}}{k_c[i]}$
	$Re_c[i] = \dfrac{G_c\, D_{eff}}{\mu_c[i]}$	$D_{eff} = OD_{ft}$ $Pr_c[i] = \dfrac{\mu_c[i]\, cp_c[i]}{k_c[i]}$ $G_c = \dfrac{\dot{m}}{A_{ff,c}}$ $A_{ff,c} = \pi\left(r_{ot}\right)^2 - A_{frontal}$

The mass flux of the cold stream (G_c) is defined as the ratio of the mass flow rate ($\dot{m}$) and the free-flow area ($A_{ff,c}$). The free-flow area of the cold stream is the difference between the available flow area within the shell and the sum of the frontal area that is presented by the fins ($A_{turb,Fins}$), the inner tube ($A_{turb,it}$), and the finned tube without fins ($A_{turb,ft}$). These areas are best understood by consulting Figure 2.13 concurrently with their definitions.

$$A_{turb,\,fins} = 2\left(tf_{ft}\; L_{fins}\right) N_{fins,rev} \tag{2.42}$$

$$A_{turb,it} = \pi\left(r_{it}\right)^2 \tag{2.43}$$

$$A_{turb,\,ft} = \left(2\, r_{ft}\right) 2\pi\left(r_{it} + rf_{ft}\right) \tag{2.44}$$

where L_{fins} is the length of the fins from the base of the finned tube and $N_{fins,rev}$ is the number of fins per revolution of the finned tube on the mandrel. The frontal area of the finned tube is the product of the circumference of the centerline of the tube and outer the diameter of the finned tube (without fins).

2.3.4 Pressure Drop Prediction

Initially, it is assumed that the only significant source of pressure drop is friction between the heat exchanger walls and the working fluid. At the start of the transient cool down process, the pressure drop will be entirely single phase. The single-phase correlations for the hot stream pressure drop per unit length ($\Delta P/\Delta L$) and the cold stream pressure drop per unit coil of finned tube ($\Delta P/\Delta N$) are provided in Table 2.6. Note that a single correlation is used for the entire Reynolds number range.

Table 2.6: Single-phase pressure drop in the hot and cold streams.

Geometry Type	Pressure drop/length (kPa/m) or coil (kPa/-)
Helical tube (Hot stream)	$\left(\frac{\Delta P}{\Delta L}\right)_h [i] = \left(\frac{0.079}{\mathrm{Re}_h[i]^{0.25}}\right)\left(\frac{2\,G_h^{\,2}}{ID_{ft}\,\rho_h[i]}\right)$
Bank of in-line Tubes (Cold stream)	$\left(\frac{\Delta P}{\Delta N}\right)_c [i] = \left[0.088 + 0.16\,X_L\left(X_T - 1\right)^{-n}\right]\frac{G_c^{\,2}}{Re_c[i]^{0.15}\,\rho_c[i]}$ $n = 0.43 + 1.13/X_L$

The single-phase pressure drop of the cold stream is a function of the non-dimensional transverse (X_T) and longitudinal pitch (X_L) of the finned tube. These are defined as the ratio of the transverse (T_p) and longitudinal pitch (L_p) and the outer diameter of the finned tube (OD_{ft}); note that T_p and L_p are illustrated in Figure 2.17:

$$X_T = \frac{T_p}{OD_{ft}} = \frac{2\,rf_{ft} + 2\,r_{it}}{OD_{ft}} \tag{2.45}$$

$$X_L = \frac{L_p}{OD_{ft}} = \frac{Sbc + 2\,rf_{ft}}{OD_{ft}} \tag{2.46}$$

where *Sbc* is the space between coils, defined as the distance between the edges of the overall finned diameter of the finned tube or the Fin_{OD}:

$$Fin_{OD} = 2\ L_{fins} + OD_{ft} \tag{2.47}$$

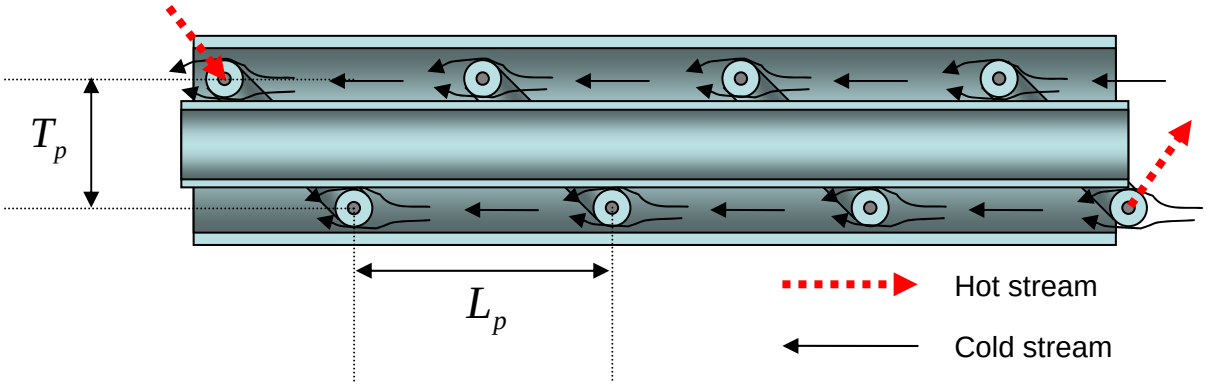

Figure 2.17: Transverse (T_p) and Longitudinal pitch (L_p) for Hampson heat exchanger.

The pressure drop of each segment is the product of the pressure gradient and the appropriate differential length. The differential pressure drop is then summed together to provide an estimate of the total pressure drop through the high and low pressure streams.

$$DP_{HP} = \sum_{i=1}^{M}\left[\left(\frac{\Delta P}{\Delta L}\right)_h[i]\ L_{ft}[i]\right]$$

$$DP_{LP} = \sum_{i=1}^{M}\left[\left(\frac{\Delta P}{\Delta L}\right)_c[i]\ L_{it}[i]\right] \tag{2.48}$$

As the working fluid is cooled further, it becomes a two-phase mixture. The pressure drop of a two-phase mixture can be significantly different from a single-phase fluid. The two-phase correlation used in this model was developed by Mueller-Steinhagen and Heck (1986) and recommended by Ould Didi, Kattan, and Thome (2002). The two-phase

model of pressure drop per unit length is an empirical extrapolation between the all gas flow (*Q=1*) and the all liquid flow (*Q=0*), where *Q* is the quality of the fluid.

$$\left(\frac{dP}{dz}\right)_{fric} = C\left(1-Q\right)^{1/3} + bQ^3 \qquad (2.49)$$
$$\text{where } C = a + 2\left(b-a\right)Q$$

The coefficients *a* and *b* are the single-phase pressure gradients (kPa/m) for all liquid and all gas flow respectively. Therefore, since the single-phase correlations are already within the model for the cold and hot streams, (as indicated by Table 2.6) the description of the two-phase frictional pressure drop prediction is complete.

2.3.5 Axial Resistance Calculation

The resistance to axial conduction through the Hampson style heat exchanger is related to the resistance that is presented by the inner tube ($R_{axial,it}$), the finned tube ($R_{axial,ft}$), and the outer tube ($R_{axial,ot}$) which are in parallel, as shown in Figure 2.18 and presented in Equation (2.50).

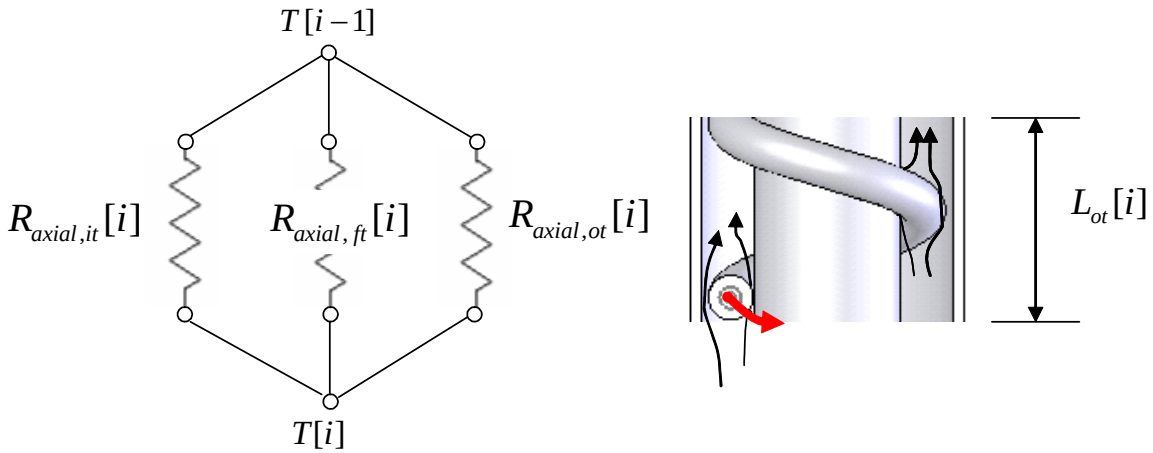

Figure 2.18: Parallel circuit network for R_{axial} calculation. *T[i-1]* is warmer than *T[i]*.

$$R_{axial}[i] = \left(\frac{1}{R_{axial,it}[i]} + \frac{1}{R_{axial,\,ft}[i]} + \frac{1}{R_{axial,ot}[i]} \right)^{-1} \tag{2.50}$$

$$R_{axial,it}[i] = \frac{L_{it}[i]}{k_{it}[i]\,A_{it}} \tag{2.51}$$

$$R_{axial,\,ft}[i] = \frac{L_{ft}[i]}{k_{ft}[i]\,A_{ft}} \tag{2.52}$$

$$R_{axial,ot}[i] = \frac{L_{ot}[i]}{k_{ot}[i]\,A_{ot}} \tag{2.53}$$

The areas through which the heat is transmitted are determined by the thickness of each tube,

$$A_{it} = \pi \left(r_{it}{}^2 - r_{it,inner}{}^2 \right) \tag{2.54}$$

$$A_{ft} = \pi \left(r_{ft}{}^2 - r_{ft,inner}{}^2 \right) \tag{2.55}$$

$$A_{ot} = \pi \left(r_{ot,outer}{}^2 - r_{ot}{}^2 \right) \tag{2.56}$$

The axial resistance of each heat exchanger segment is then summed to provide an estimation of the total axial resistance (R_{axial}).

$$R_{axial} = \sum_{i=1}^{M} R_{axial}[i] \tag{2.57}$$

Thus axial conduction of heat through the heat exchanger is a function of the thermal conductivity of the heat exchanger components, and the length and thickness of the shell and mandrel.

Note that the formulation for $R_{axial,ft}$ is most likely an under estimate, since the presence of the fins is neglected. The entire length of the finned tube is employed rather than the sum of the unfinned length. Even so, the mandrel and shell (in parallel with the finned tube) provide a much smaller resistance to axial conduction than the finned tube, therefore, though the $R_{axial,ft}$ is an underestimate, its contribution to the total axial resistance is small.

2.4 Design

2.4.1 Design Methodology

The modeling tools discussed in the previous section can be used to determine the refrigeration power of a candidate device (i.e., a given geometry) for a set of operating conditions by coordinating their inputs and outputs as shown in Figure 2.19.

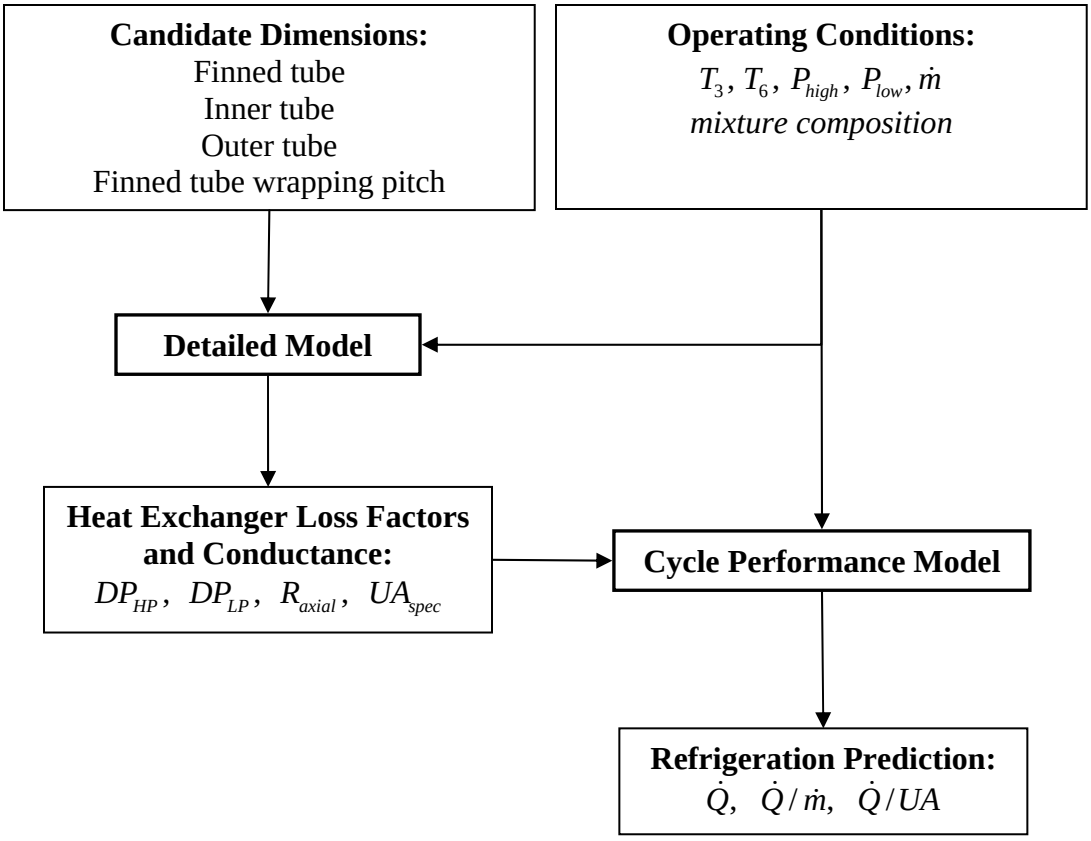

Figure 2.19: Performance prediction process.

It is not feasible to perform a complete parametric study and optimization of the Hampson geometry using the full modeling process described in Figure 2.19; therefore, the process is accelerated by first exploring the influence of the loss factors on the cycle independent of the geometry. This process provides some understanding relative to the

required performance in terms of the heat exchanger characteristics (i.e., the required conductance, pressure drop, axial conduction) which can be used directly within the detailed heat exchanger model. This two-step process saves time and allows a more comprehensive optimization of the geometric parameters by removing the need to run the cycle performance model for every geometry change. That is, instead of spending a large amount of time mapping out the relationship between each design variable and the resulting refrigeration prediction, the limitations imposed by the loss factors provide an intermediate standard that allows a rapid evaluation of the suitability of a candidate design. In addition, by separating the discussion of the influence of the loss factors from the specific geometric variables associated with the Hampson heat exchanger, the underlying reasons for the design constraints become clear. This design process is illustrated in Figure 2.20.

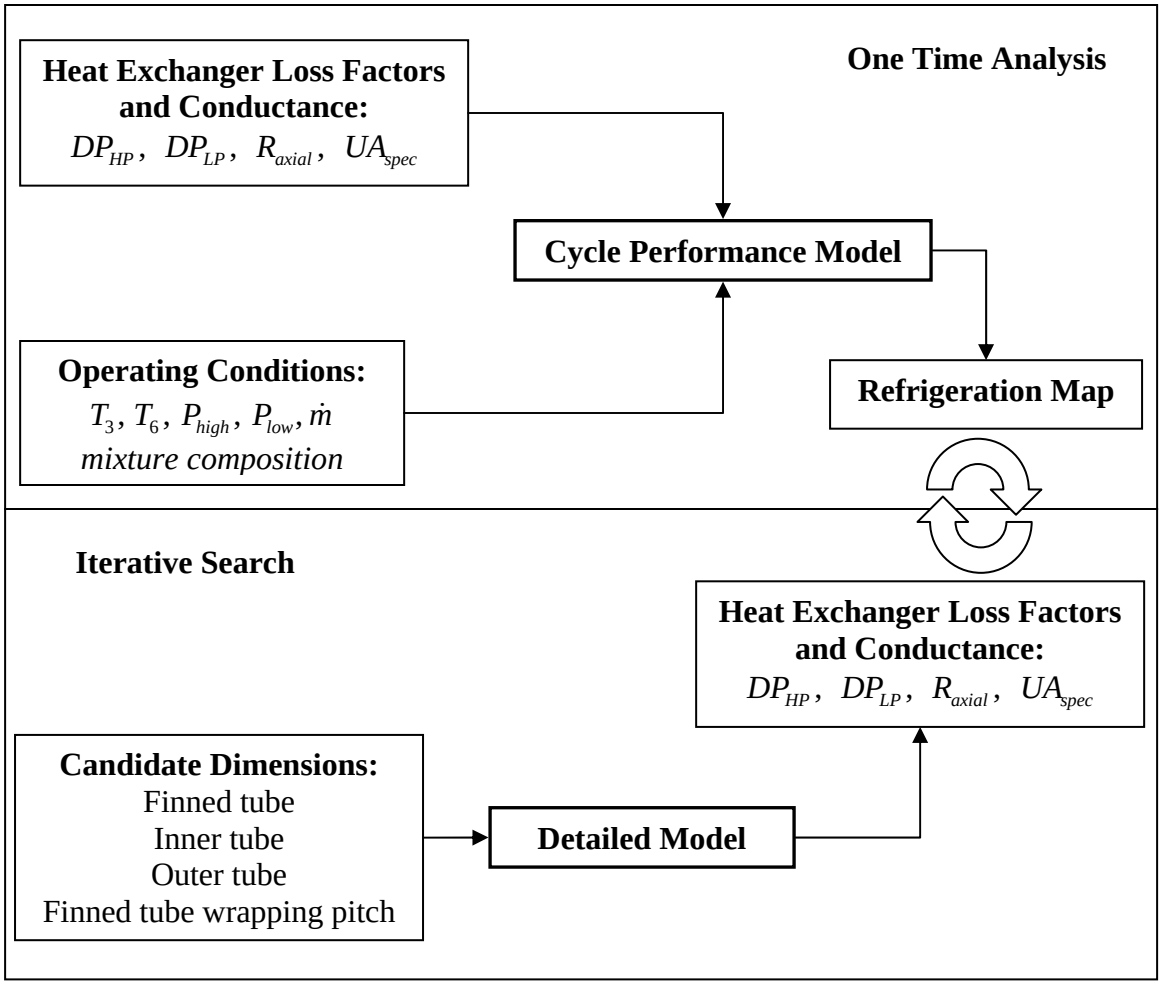

Figure 2.20: Design search method.

Using the approach outlined in Figure 2.20, many of the design variables of the Hampson geometry can be determined in a relatively short time. Once the values for the majority of the design variables are approximately defined then the full prediction process is used to make a more precise estimate of the device performance.

2.4.2 Design Constraints

There are two categories of design constraints; fluid-thermal constraints which are captured by the loss factors and manufacturing constraints that are specific to the design of the Hampson style heat exchanger as well as the time and money that is available to build prototypes. The thermal-fluid constraints will be discussed here and manufacturing considerations are discussed in Chapter 3.

The first and most important characteristic of the heat exchanger is its conductance (*UA*). In order to understand the influence of *UA* on the performance of a system, reconsider Figure 2.10 which shows $\dot{Q}/\dot{m}$ and $\dot{Q}/UA$ as a function of the hot end temperature difference ΔT for the nominal design conditions summarized in Table 2.2.

For this discussion, only the $\dot{Q}_{load,dist}/\dot{Q}_{load.cold} = 0$ case is considered (the distributed load case shows nearly the same characteristics). Notice that $\dot{Q}/UA$ has an optimum near ΔT = 3 K and that $\dot{Q}/\dot{m}$ is approximately 11 J/g at this value of ΔT. Instead of viewing the refrigeration capacity as a function of ΔT, a more intuitive representation of $\dot{Q}/\dot{m}$ can be displayed by plotting the refrigeration capacity (W) of the cycle as a function of mass flow rate at this optimal condition, as shown in Figure 2.21. This figure provides immediate information relative to the magnitude of the mass flow rate that is appropriate for a device that is designed to receive a cold end heat load on the order of 100's of milliwatts.

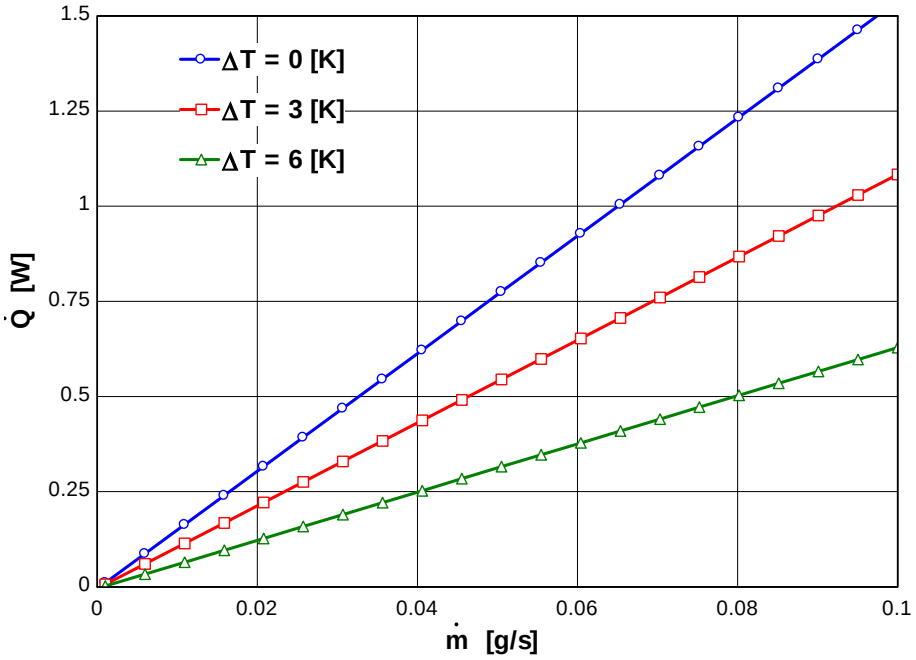

Figure 2.21: Refrigeration capacity as a function of mass flow rate for ΔT = 0K, 3K, and 6K (with no other losses).

Figure 2.21 represents the ideal performance of the cycle; that is, the refrigeration that would be provided in the absence of pressure drop or axial conduction losses and assuming that the heat exchanger conductance is sufficiently large to provide the stated hot end temperature difference. As was discussed previously, even though the maximum possible cooling results from the ΔT = 0 K case, this is not a particularly interesting or optimal case as it requires an infinitely large heat exchanger. The optimal system is closer to the ΔT = 3K case, as this provides the most refrigeration per unit of conductance. The conductance requirement for the ΔT = 3K is shown in Figure 2.22 as a function of the mass flow rate.

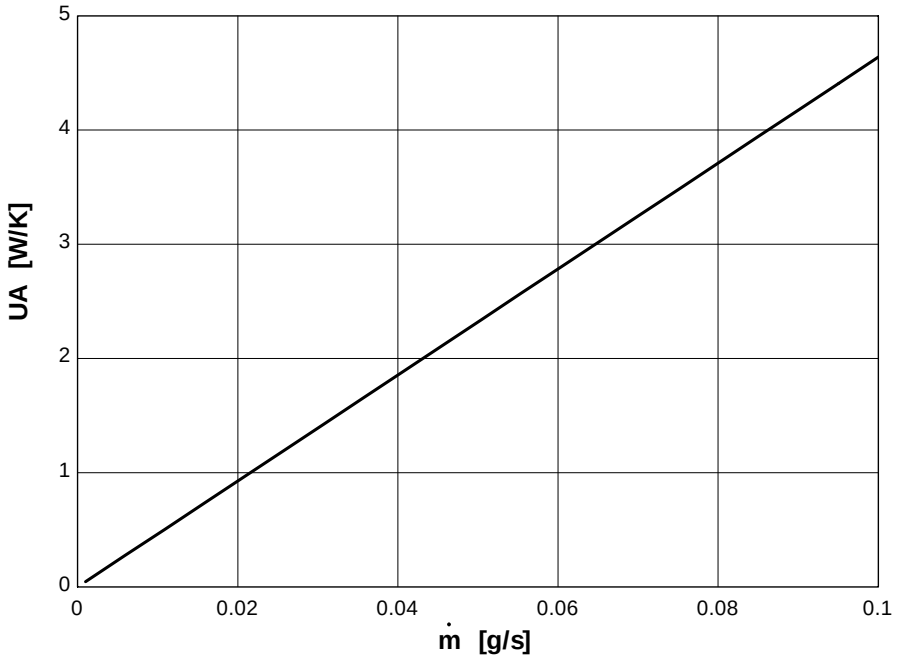

Figure 2.22: Heat exchanger conductance required to provide the refrigeration shown for ΔT = 3K.

Note that if the actual heat exchanger conductance is less than the locus of points shown in Fig. 2.22 then the hot end temperature difference will increase and, according to Fig. 2.10, the amount of refrigeration provided will decrease. Figure 2.23 illustrates the refrigeration as a function of mass flow rate for various values of conductance and clearly shows the penalty associated with reduced conductance.

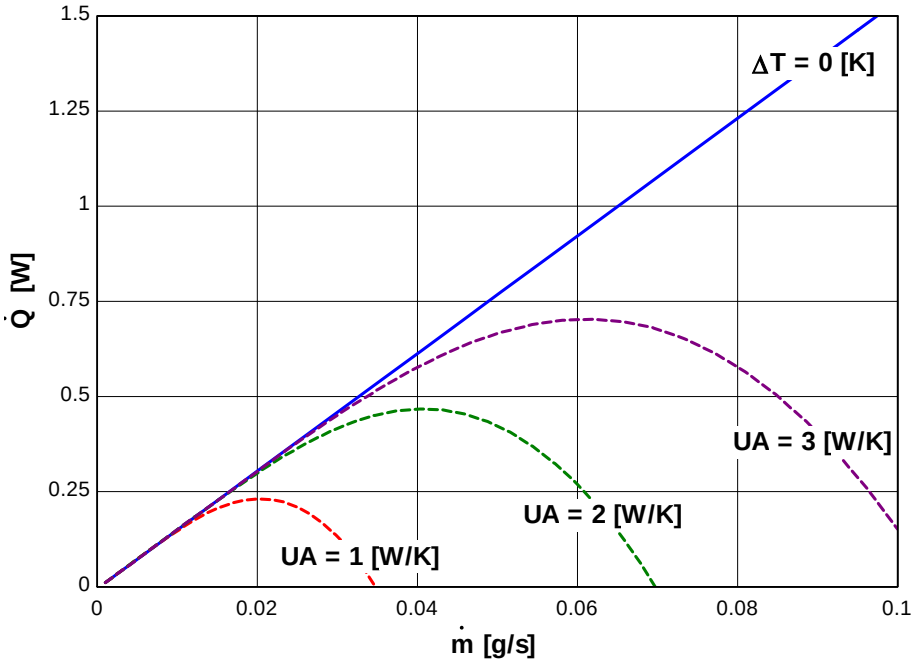

Figure 2.23: Refrigeration power as a function of mass flow rate and the stated conductance. The ΔT = 0K case requires an infinite conductance.

The implication of Figure 2.23 is that there is an optimum mass flow rate which depends on the conductance. If the mass flow rate is too small then the heat exchanger is oversized and refrigeration potential of the cycle (which, for an ideal heat exchanger is proportional to the mass flow rate) is reduced. If the mass flow rate is too large then the heat exchanger is undersized and the cycle performance is degraded by the heat exchanger losses. The advantage of the mixture optimization that was previously described is that it ensures that the *UA* required to achieve the predicted refrigeration power is a minimum compared to other mixtures for the operating conditions in Table 2.2. If this were not the case, then this process would be less meaningful, as a better performing mixture might be available which would change the conductance

requirement. It should also be noted that the design mixture freezes for $\Delta T < 2$ K [per Eq. (2.23)]. Therefore, to produce figures such as 2.23, the freeze constraint was ignored.

The process of determining the specific values for the Hampson geometry that are reasonable is shortened in that the cycle performance model does not need to be run until the detailed model predicts that a candidate design provides at least the conductance shown in Figure 2.23. That is, for 500 mW of refrigeration it seems clear that the mass flow rate will be on the order of 0.05 g/s and the conductance must be at least 2.5 W/K. These are very valuable targets that can, with confidence, be transferred to the detailed model in order to guide the geometry selection process.

The pressure drop in both the hot (DP_{HP}) and cold streams (DP_{LP}) can be evaluated in the context of the range of mass flow rates required to develop the target refrigeration power. The pressure drop associated with the hot stream will be much larger than the pressure drop of the cold stream for any practical geometry due to the much larger free flow area that is available to the cold stream. Therefore, pressure drop in the hot stream will be the focus of this discussion and we will look specifically at how pressure drop affects the cooling power of the device if it is assumed that it is otherwise perfect; that is, the device provides the required heat exchanger conductance for $\Delta T = 3$ K and does not permit any axial heat leak through conduction.

Figure 2.24 shows the refrigeration per unit of mass flow rate as a function of the hot side pressure drop and indicates that the result of a 100 kPa pressure drop through the finned tube will be a loss of almost 1 (J/g) in the refrigeration per unit mass flow rate.

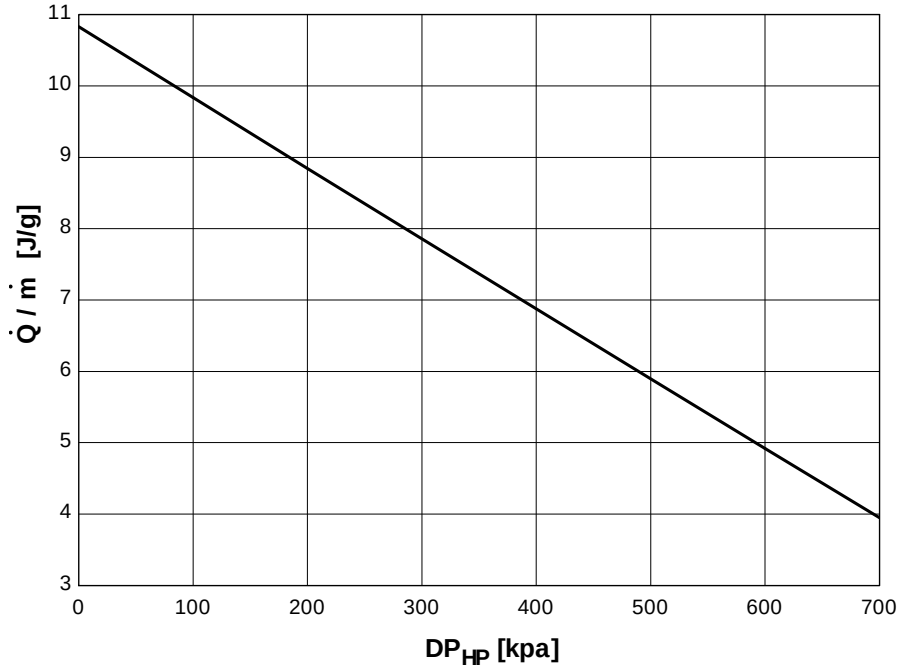

Figure 2.24: Refrigeration power per unit mass flow rate as a function of hot stream pressure drop (ΔT = 3K).

The refrigeration power is illustrated as a function of mass flow rate for different values of the pressure loss in Figure 2.25. Notice that the refrigeration decreases by about 9% per 100 kPa. Again, this investigation has revealed useful information that can be transferred directly to the detailed model; specifically, a candidate device must have a pressure drop that is less than 200 kPa in order to be suitable for this application.

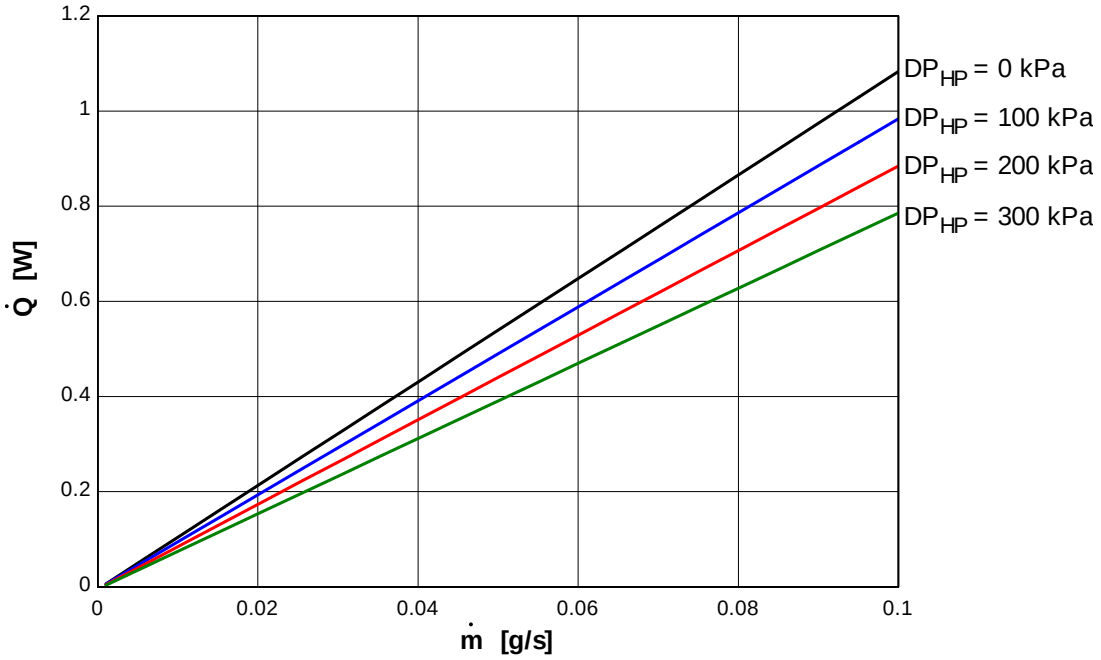

Figure 2.25: The loss in refrigeration power as the inlet pressure to the orifice is lowered by pressure drop through the hot stream.

Finally, axial conduction through the heat exchanger provides an additional loss of refrigeration power. The axial conduction loss reduces the refrigeration by an amount that is essentially independent of the mass flow rate and therefore provides a lower limit on the mass flow rate range; that is, in order to provide refrigeration the system must remove more heat than is conducted to the cold end. Figure 2.26 illustrates the heat transferred to the cold end by axial conduction as a function of the axial conduction resistance.

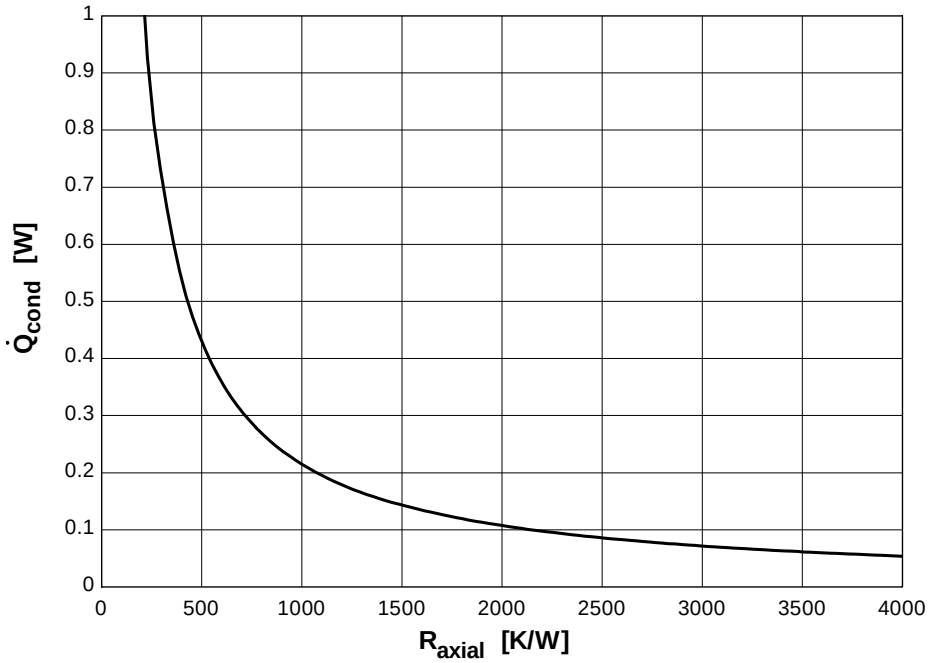

Figure 2.26: The axial conduction loss as a function of the axial conduction thermal resistance at the design conditions.

By comparing Figure 2.26 to Figure 2.22, it is clear that designs with lower mass flow rate and therefore lower refrigeration capacity are more vulnerable to axial conduction (of course these designs are also more efficient as they require less compressor power). In order to make a low mass flow rate design (i.e., a small and efficient device) the required resistance to axial conduction must be very large; on the order of 1000-2000 K/W based on Fig. 2.26.

In conclusion, shortfalls in the conductance and pressure drop in the hot stream both tend to reduce the available refrigeration relative to what could be provided by the design mixture at ΔT = 3 K; these losses increase as the mass flow rate is increased. The axial conduction consumes a set amount of refrigeration power and therefore limits the

minimum mass flow rate. By exploring the influence of these loss factors on cycle performance independent of the geometric parameters, some intuition is obtained relative to the impact of conductance, pressure drop, and axial conduction and their required values for a recuperative heat exchanger that is suitable for this application. Specifically, the previous discussion has resulted in valuable targets for mass flow rate, conductance, pressure drop, and thermal resistance to axial conductance that can be applied to the Hampson geometric design process. The following sections discuss the design of the two demonstration devices that were fabricated for this project.

2.4.3 Device A Design

The design of Device A (the first demonstration device) was simplified by the fact that the finned tube available for the device was specified (a length of finned tube of approximately the right size had been previously donated) and therefore many of the geometric parameters could not be adjusted. The finned tube's specifications are summarized in Table 2.7 and a photograph is provided in Figure 2.27.

Table 2.7: Finned tube dimensions for Device A.

Geometric variable	inch	metric
$L_{ft,t}$	59 (in)	1.5 (m)
OD_{ft}	0.021 (in)	0.5334 (mm)
ID_{ft}	0.011 (in)	0.2794 (mm)
L_{fins}	0.010 (in)	0.254 (mm)
Fin_{OD}	0.041 (in)	1.04 (mm)
S_{ft}	0.007 (in)	0.1778 (mm)
tf_{ft}	0.003 (in)	76.2 (μm)
$Fins_{inch}$ / Fin Pitch	100 (1/in)	254 (μm)

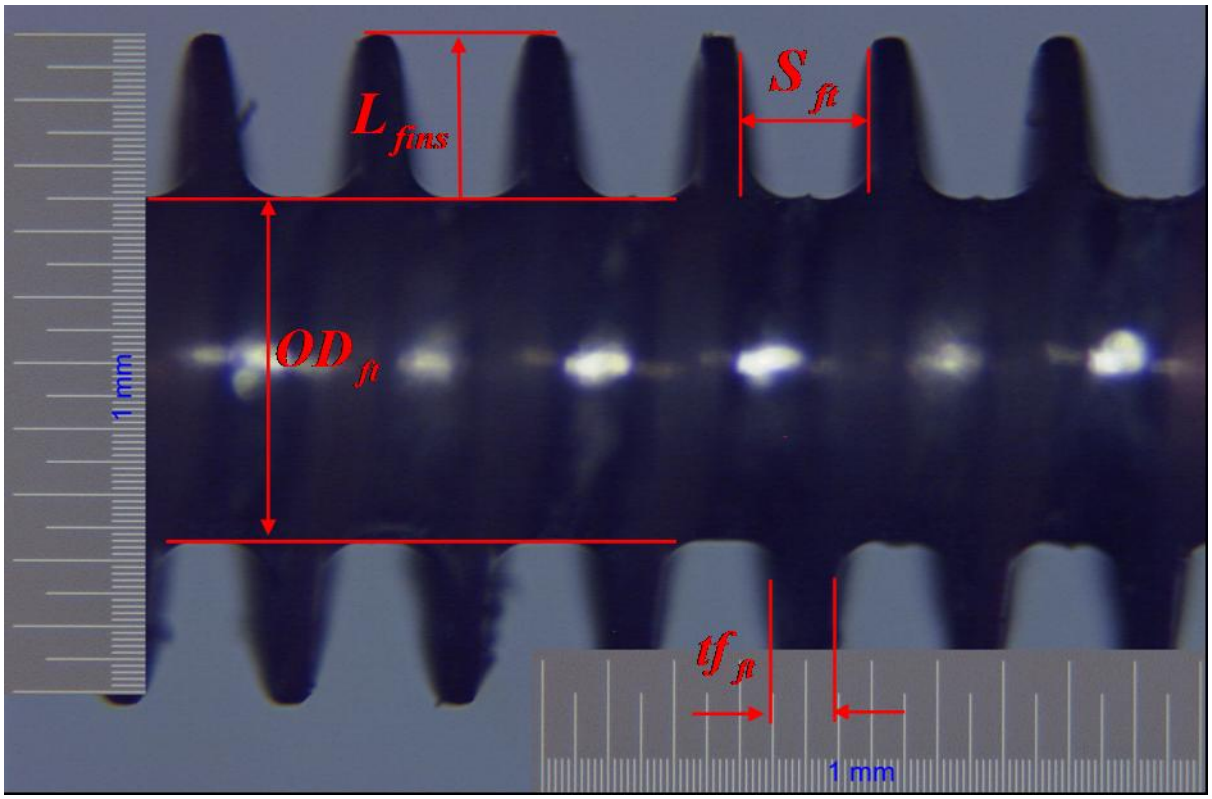

Figure 2.27: Finned tube at 50 X magnification.

The design question for this device is therefore, 'How is the specific finned tube best employed?', rather than, 'Which size finned tube is best?'. The finned tube specifications provide most of the information that is required for the detailed model to predict the conductance and hot stream pressure drop as a function of the mass flow rate for the device. The influence of the pitch and mandrel diameter on conductance and pressure drop are relatively small compared to the influence of the finned tube diameter, length, and fin size.

To determine the conductance of the finned tube it is necessary to specify the length of finned tube that is required for assembly (this is mainly related to providing sufficient length to seal the finned tube to the heat exchanger inlet and outlet ports); this is a manufacturing constraint that is discussed in Chapter 3 and results in a finned tube length that is available for the heat exchanger itself of 1.13 m (44.488 in). The remaining design choices are mostly related to minimizing the axial conduction to the cold end; specifically, the material and diameters of inner and outer tubes as well as the spacing between the coils (*Sbc*) must be selected.

The thermal conductivity of the mandrel and shell contributes only to the axial conduction and not to the stream-to-stream conductance of the device; therefore, the thermal conductivity of these tubes should be as small as possible. In addition, the device must be hermetically sealed. While, it may be possible to manufacture a device from non-metallic, insulating materials (e.g., G-10 or Micarta) that is sealed using non-traditional joining techniques (e.g., Stycast or some other cryogenic epoxy), this type of design would require substantial development effort which is beyond the scope of this project. Therefore, 304 stainless steel was selected for both the mandrel and the shell; 304 SS can be obtained as very thin wall tubes, can be sealed using TIG welding and has a relatively low thermal conductivity.

The next constraint that must be considered is the geometric envelope of the vacuum space which is more generally related to the size of the device that can be tolerated by a given application; the geometric envelope will ultimately be related to system level

constraints related to the details of an application. For this project, the available Dewar can contain a cryostat that is no longer than 0.889 m (35 in) long. This limits the overall length of the heat exchanger and thus the maximum axial resistance that can be obtained.

The remaining design choices include the ID of the outer tube, the OD of the inner tube, and the spacing between coils (*Sbc*). The thicknesses of the shell and mandrel walls are selected based on the minimum sizes that are commercially available and can be welded. The selection of the sizes for the shell and mandrel are controlled by consideration of axial conduction as well as some aspects of the assembly process. In order to minimize axial conduction, the smallest diameter tubing that is otherwise feasible should be selected. However, very small mandrel sizes increase the risk of crimping the thin-walled finned tube as it is wrapped upon the mandrel (i.e., winding the tube too tightly so that it breaks). Based on a trial wrapping process of the same size finned tube onto a 4 mm (0.1575 in) diameter mandrel, the combination of mandrel and shell detailed in Table 2.8 were selected.

Table 2.8: Inner and outer tube dimensions for Device A.

Geometric variable	Value	Tolerance (in)
OD_{ot}	6.35 mm (0.25 in)	± 0.127 mm (0.005 in)
t_{ot}	0.254 mm (0.010 in)	
OD_{it}	3.40 mm (0.134 in)	± 0.127 mm (0.005 in)
t_{it}	0.2032 mm (0.008 in)	

The shell and mandrel described in Table 2.8 provides a theoretical clearance of 350 μm (0.014 in) between the outer surface of the fins (after the finned tube is wrapped on the mandrel) and the inner surface of the shell. This clearance seems somewhat generous;

however, it was selected because the actual clearance will be substantially less than the theoretical clearance which is based on a perfect and rigid winding. The finned tube will spring back somewhat due to its elasticity (i.e., it will try to retain its initial, straight shape); this effect can be controlled somewhat by the wrapping process but not eliminated. Also, the inner and outer tubes are not perfectly straight and their diameters are not exactly as specified; therefore some clearance is necessary to account for these manufacturing tolerances.

Wrapping the finned tube (which is 1.13 m long) with a spacing of 3.0 mm (0.118 in) results in a mandrel length of 0.315 m (12.4 in); this completely specifies the geometry for Device A. Figure 2.28 illustrates the total axial thermal resistance of the mandrel/shell/finned tube assembly; note that the 0.315 m length of Device A provides a total axial thermal resistance of nearly 3500 K/W. The axial resistance provided by the entire assembly is therefore sufficiently greater than the previously discussed target value of 1500 K/W.

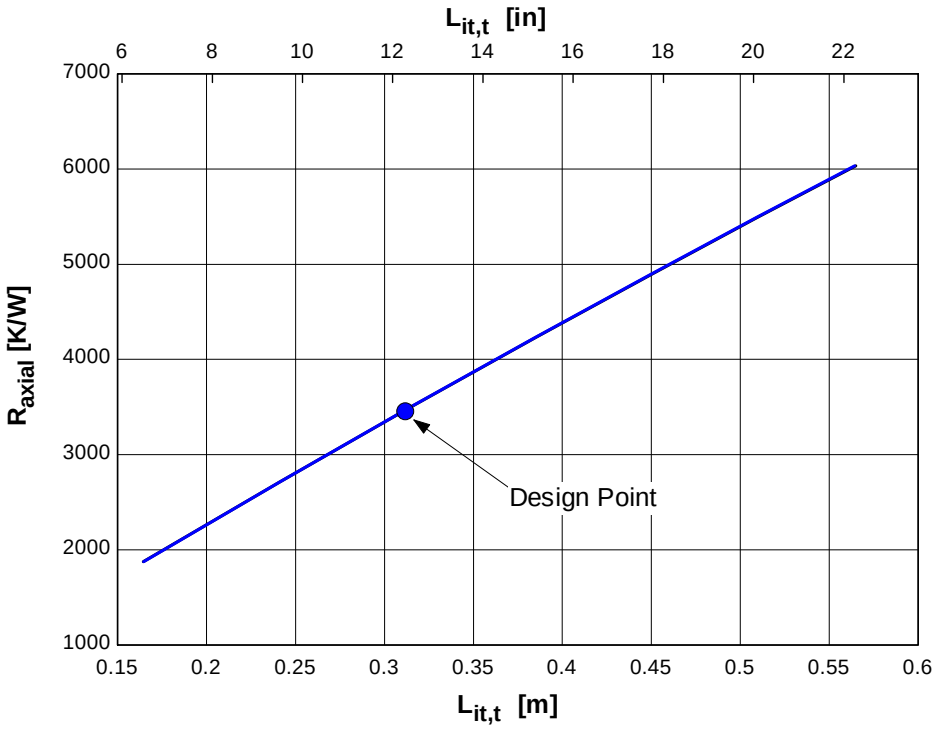

Figure 2.28: Axial resistance of the selected mandrel/shell/finned tube assembly as a function of heat exchanger length.

The conductance for Device A as a function of mass flow rate is shown in Figure 2.29, together with the conductance requirement for ΔT = 3 K. Note that the mass flow rate scale has been reduced from 0 - 0.1 g/s (in all of the previous plots about loss factors) to 0 - 0.05 g/s. The conductance function of the heat exchanger is almost constant at 1 W/K as a function of mass flow rate; this is substantially below the target requirement of 2.5 W/K previously identified but cannot be adjusted based on the fixed length of finned tube.

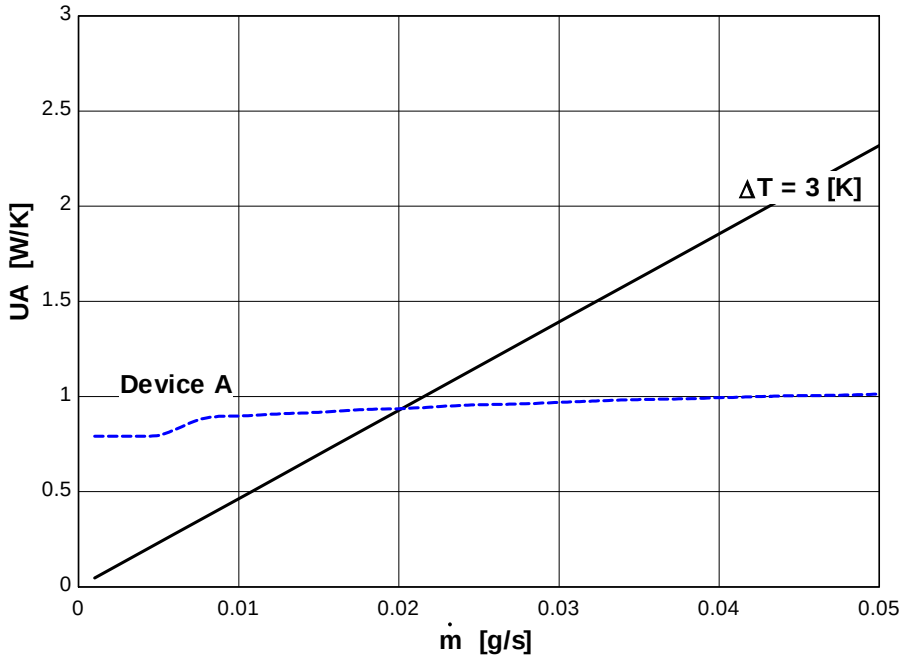

Figure 2.29: The required conductance for ΔT = 3 K and the conductance function for Device A.

From the previous discussion on the influence of the heat exchanger conductance, it is clear that the cooling performance for Device A will have an optimum that occurs between 0.01-0.02 g/s and that the flow rate must be less than 0.04 g/s in order to provide any positive refrigeration due to limited conductance. This restricts the cooling performance of the device to the lower end of the target cooling range (<500 mW).

The hot stream pressure drop as a function of mass flow rate is shown in Figure 2.30. Notice that the hot stream pressure drop is consistent with the target value of a few hundred kPa at the mass flow rates of interest.

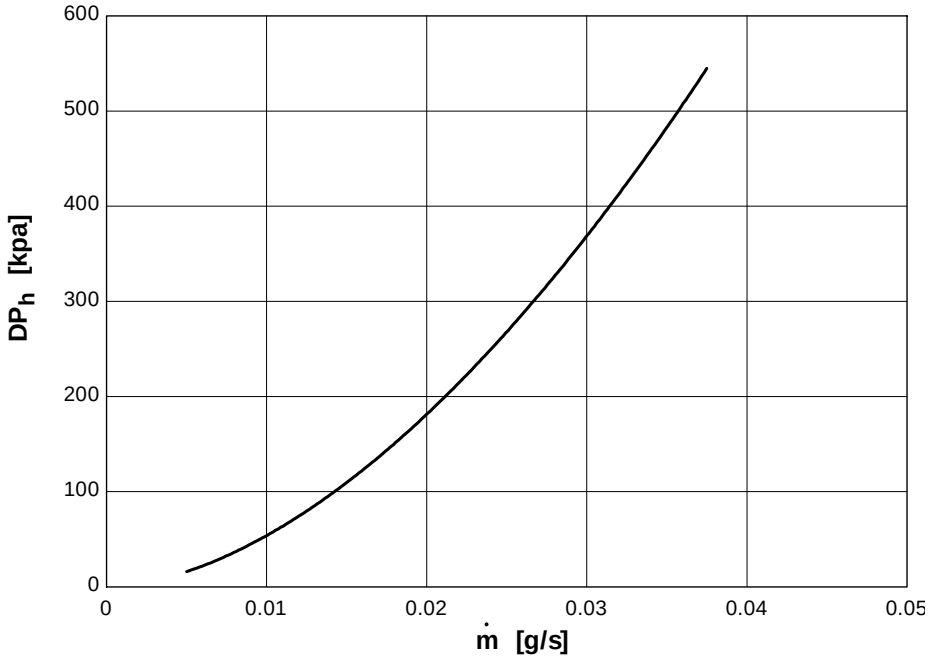

Figure 2.30: Hot stream pressure drop of Device A.

Figure 2.31 illustrates the cooling power of the device as a function of mass flow rate; the upper curve represents the cooling power with no losses and the successively lower curves are generated as each loss is applied. Notice that the loss related to the limited conductance is the largest factor (which is not surprising given the sub-optimal conductance associated with Device A) whereas axial conduction and pressure drop affect the performance approximately equally.

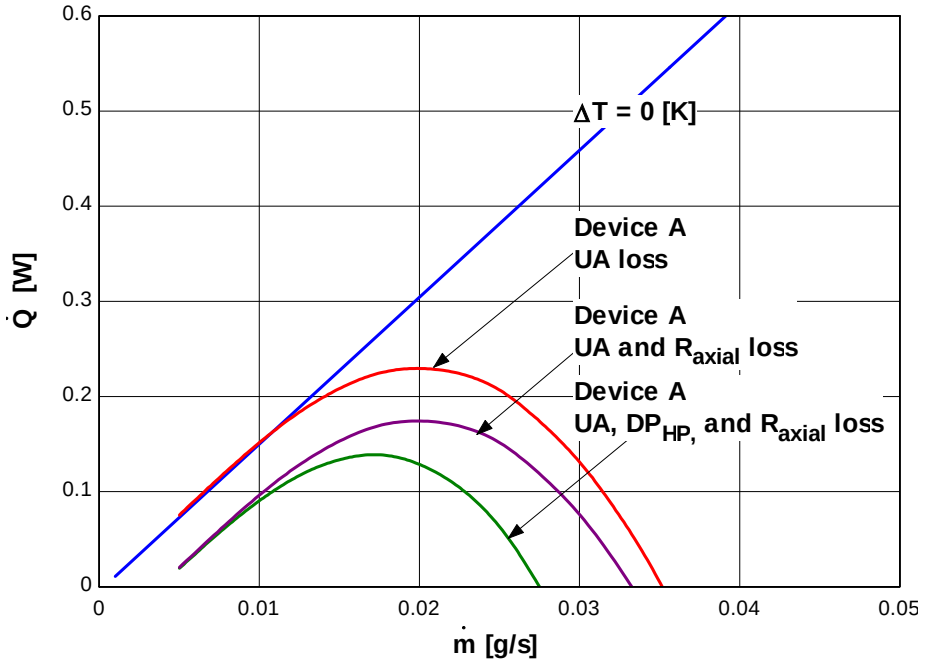

Figure 2.31: The influence of the various loss factors on the performance of Device A.

Note that the device should be able to provide a little over 100 milliwatts of cooling with a mass flow rate of nominally 0.015 g/s. This is a very small cooling power but it is consistent with the target requirements for high temperature superconducting electronics. The mechanical design, fabrication, and testing of the device was warranted in order to confirm detailed model prediction. Once verified, a higher performance design could be more easily fabricated and tested with the aid of the design model. In addition, the cooling power shown in Figure 2.31 is considered conservative and should be improved by the presence of two-phase flow within both the hot and cold streams.

2.4.4 Device B Design

During testing of Device A (described more completely in a subsequent chapter) it was observed experimentally that the flow rate ceased suddenly when the cold end achieved a temperature that was significantly above the 85 K target for the design; this behavior was repeatable and the temperature seemed to correspond to the point at which liquid began to form. This was attributed to liquid management; that is, the vapor velocity for Device A is very small due to the relatively large open area on the low pressure side and the very low mass flow rate. Therefore, the vapor velocity was insufficient to move the liquid through the channels resulting in a buildup of liquid and a reduction in the flow.

Based on these tests, a second device was designed with the objective of attaining higher mass flow rates and therefore higher kinetic energy. To enable the range of the mass flow rate to increase it is necessary that the pressure drop in the high pressure side be decreased and the conductance of the heat exchanger must be increased. Increasing the ID of the finned tube will decrease the pressure drop of the hot stream for a given mass flow rate but with a corresponding reduction in the heat transfer coefficient within the tube and therefore a reduction in the overall conductance for a given length heat exchanger. Therefore, increasing the ID_{ft}, is useful only inasmuch as the overall conductance is not decreased significantly. An alternative technique for increasing the mass flow rate range of the device is to wrap multiple finned tubes in parallel on the mandrel; as illustrated in Figure 2.32.

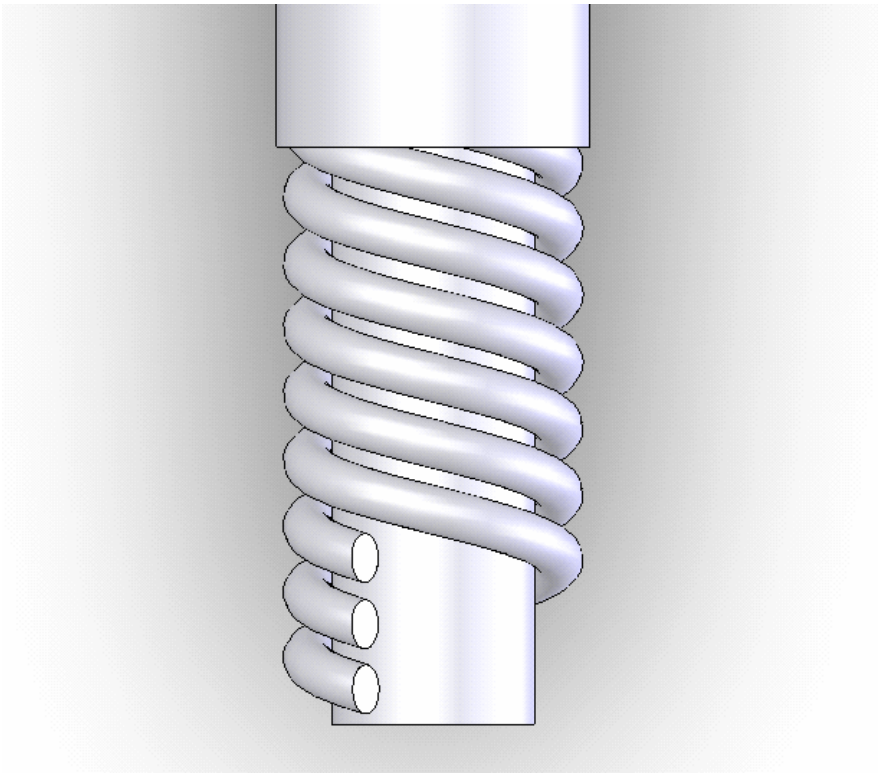

Figure 2.32: Multiple finned tubes in parallel (the fins are not shown).

In addition to reducing the pressure drop, the addition of the multiple finned tubes increases the conductance of the device for a given mass flow rate by increasing the surface area. As the conductance was shown to be the major constraint on the performance of Device A, the benefit of parallel tubes is considered worth the effort required to develop the necessary fabrication techniques.

The modifications that need to be made to the detailed model to account for multiple finned tubes are relatively straightforward. First, the mass flow rate through each tube is assumed to be equal to the total mass flow rate divided by the number of tubes (N_T); this assumes a perfect distribution of the fluid. The pressure drop through the finned tubes is calculated using this mass flow rate through each tube instead of the total mass flow rate.

The total axial resistance of the heat exchanger is decreased by adding multiple finned tube resistors; this is accounted for by adding parallel resistors to the overall resistance network that represents axial conduction through the heat exchanger. Finally, the conductance of the heat exchanger is multiplied by the number of tubes.

An additional consideration for the multiple tube design is related to the spacing of the multiple tubes; the parameter, *Sbc* is the spacing between a particular finned tube and its own next coil, not the adjacent coil. Thus, for clarity, let Sbc_{adj} be the spacing between adjacent finned tubes. Note that for a single finned tube, this parameter is the same as *Sbc*.

$$Sbc = N_T \left(Sbc_{adj} \right) + Fin_{OD} \left(N_T - 1 \right) \tag{2.58}$$

The finned tube selected for Device B (based primarily on evaluating the limited set of finned tubes that are available for purchase at a reasonable price) is summarized in Table 2.9.

Table 2.9: Finned tube dimensions for Device B.

Geometric variable	inch	metric
$L_{ft,t}$	60 (in)	1.524 (m)
OD_{ft}	0.058 (in)	1.473 (mm)
ID_{ft}	0.041 (in)	1.041 (mm)
t_{ft}	0.0085 (in)	0.216 (mm)
L_{fins}	0.03 (in)	0.762 (mm)
Fin_{OD}	0.118 (in)	2.997 (mm)
S_{ft}	0.023 (in)	0.591 (mm)
tf_{ft}	0.008 (in)	203.2 (μm)
$Fins_{inch}$ / Fin Pitch	32 (1/in)	794 (μm)

The size of the finned tube used for Device B is larger than for Device A. As a basis of comparison, note that the outer diameter of the fins for the Device A tube is the same size as the inner diameter of the tube used for Device B. However, the length of the finned tubes for either device are approximately 1.5 m long; as with Device A, the total length of the finned tube is not available for the heat exchanger due to the length required for the headers. Based on the experience of assembling Device A, it is assumed that the length required for the headers is approximately 0.15 m (6 in) (corresponding to 0.076 m on each end). Therefore, the length of finned tube wrapped on the mandrel must be less than 1.37 m (54 in). The remaining fabrication constraints limit the design parameters to the ranges listed in Table 2.10.

Table 2.10: Assumed fabrication limits to multiple tube design.

Variable	Range
N_T (Number of Tubes)	1 - 4
OD_{it}	0.25 - 0.5 (in)
$Annular_{tol}$ (Tolerance between wrapped finned tube and ID of the shell)	0.010 - 0.015 (in)
$L_{it,t}$	0.315 - 0.34 (m)
t_{ot} , t_{it}	$\leq$ 0.010 (in)

The influence of the mandrel and shell size on the loss factors (for the multiple tube geometry) was investigated. For Device A, the selection of a smaller diameter mandrel/shell combination was driven by the desire to reduce the axial conduction loss and the conductance of the device was not influenced by the mandrel size because the entire available length of the finned tube could be utilized given the available mandrel length. However, this is not the case for the multiple tube geometry. Consider how the

spacing, *Sbc* (or the spacing between coils of the same finned tube) of the individual finned tubes is quite large in Figure 2.32. The addition of more finned tubes will further increase this spacing. Because the mandrel length restraint (Dewar space) is essentially the same for device B, adding finned tubes decreases the length of the individual finned tubes that can be installed and therefore affects the conductance and pressure drop.

As the finned tube length is decreased, the conductance of each individual finned tube is decreased. At some point, the addition of another finned tube lowers the overall conductance as opposed to increasing it. Since the Dewar length available for the device cannot be increased, the only way to allow for a longer finned tube is to increase the diameter of the mandrel which allows longer finned tubes to be wrapped for a given length of heat exchanger. However, the addition of finned tubes and the associated increase in the diameter of the mandrel will both tend to increase the axial conduction.

The design process for the multiple tube geometry is the same as the single tube process described in Figure 2.20. Since the required conductance, axial resistance, and pressure drop were previously determined (section 2.4.2), the task of designing device B involves comparing the loss factors for several geometric specifications to these requirements; this process was continued until the refrigeration power and mass flow rate were increased by several times over Device A. Rather than present the details of the design process, the design trade-offs associated with this geometry are more easily communicated by presenting the cooling power prediction for the three designs shown in Table 2.11.

Table 2.11: Shell and mandrel illustration designs.

Design	1	2	3
ID_{ot}	12.7 mm (0.5 in)	15.875 mm (0.625 in)	19.05 mm (0.75 in)
t_{ot}	0.1524 mm (0.006 in)	0.2032 mm (0.008 in)	0.254 mm (0.010 in)
OD_{it}	6.35 mm (0.25 in)	9.53 mm (0.375 in)	12.7 mm (0.5 in)
t_{it}	0.1524 mm (0.006 in)	0.1524 mm (0.006 in)	0.1524 mm (0.006 in)
$Annular_{tol}$	0.3556 mm (0.014 in)	0.3556 mm (0.014 in)	0.3556 mm (0.014 in)

To create a meaningful comparison between the single tube and multiple tube designs, the spacing (*Sbc* or Sbc_{adj}) is adjusted to maintain a mandrel length of no less than 0.315 (m) and a finned tube length not greater than 1.372 (m). The mandrel length limitation ensures that the difference in axial resistance between designs will be due solely to the changes in the mandrel diameter and the finned tube length limitation ensures that the length of finned tube is utilized to the full extent possible.

The refrigeration power of each design is shown as a function of mass flow rate for mandrel sizes of 6.35 mm, 9.53 mm, and 12.7 mm (i.e., designs 1 through 3) in Figures 2.33 through 2.35, respectively. For each design, 1 through 4 tube configurations are shown. Note that the increased flow area provided by the larger finned tubes reduces the hot stream pressure drop to a negligible value for all designs. Therefore, only conductance and axial resistance significantly influence the performance.

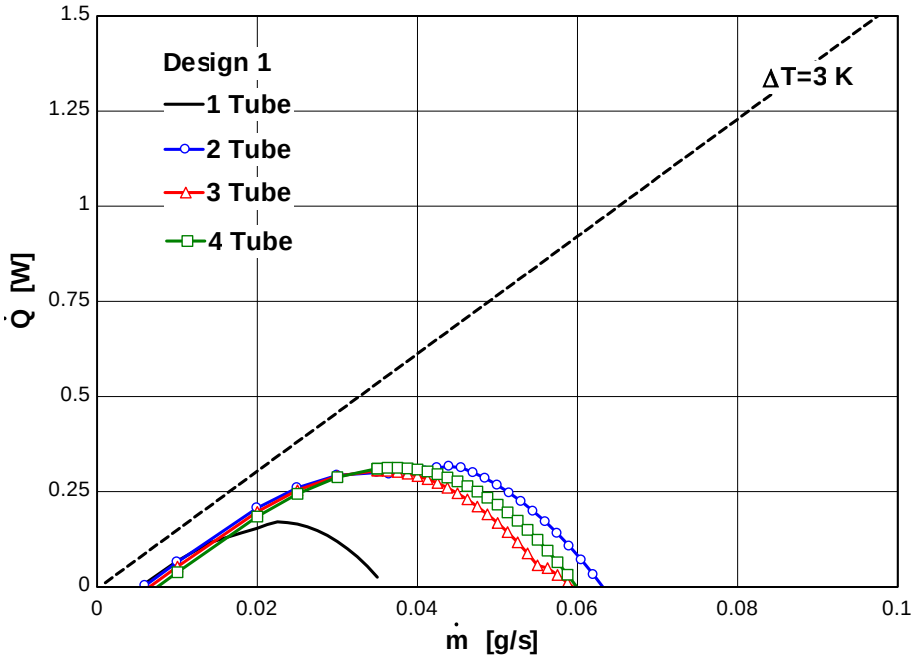

Figure 2.33: Refrigeration power of multiple tubes using a 6.35 mm (0.25 in) mandrel (i.e., Design #1).

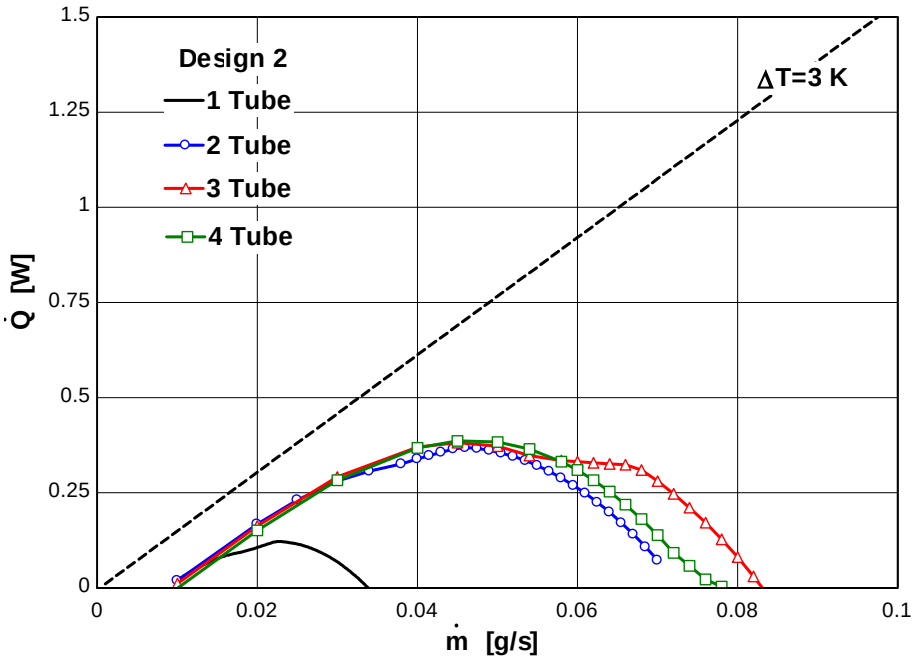

Figure 2.34: Refrigeration power of multiple tubes using a 9.53 mm (0.375 in) mandrel (i.e., Design #2).

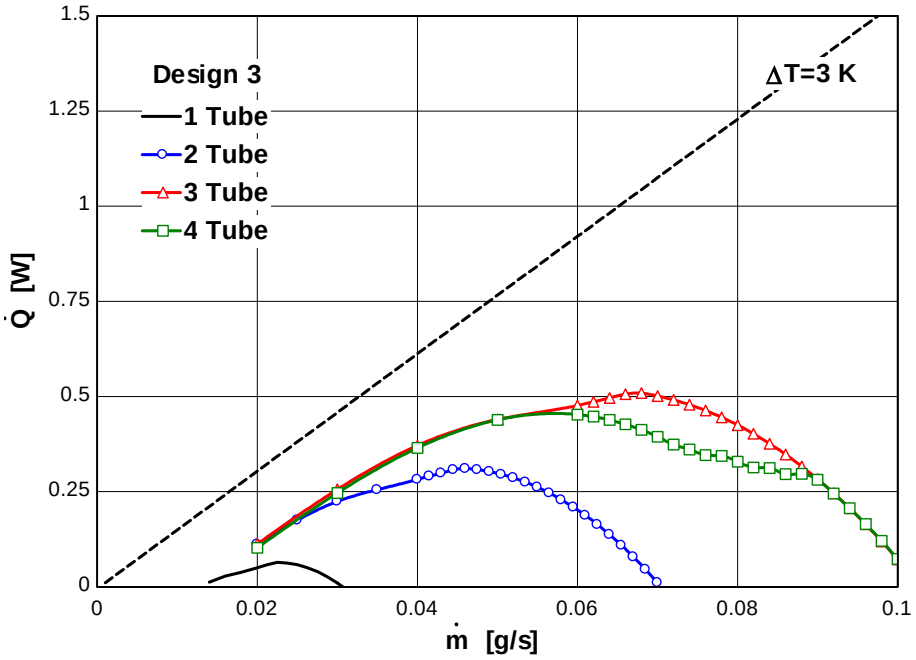

Figure 2.35: Refrigeration power of multiple tubes using a 12.7 mm (0.5 in) mandrel (i.e., Design #3).

For design 1 (see Fig. 2.33), there is no benefit to using more than 2 finned tubes. This is because the maximum length finned tube that can be wrapped with multiple tubes gets smaller with each additional finned tube. Figure 2.36 illustrates the maximum length of tube that can be wrapped as a function of the number of tubes for the 3 different mandrel sizes (i.e., the three designs). Note that for the smallest mandrel (Design #1), the tube length is immediately reduced as the number of tubes increases; this reduction is delayed as the diameter of the mandrel increases.

The geometric constraint associated with wrapping multiple tubes is the reason that the larger mandrel diameters are more desirable than smaller ones. The larger diameter mandrels permit long finned tubes, which in turn provide a larger conductance. The

increase in axial conduction (for these diameters) is not enough to diminish the benefit of the increased conductance.

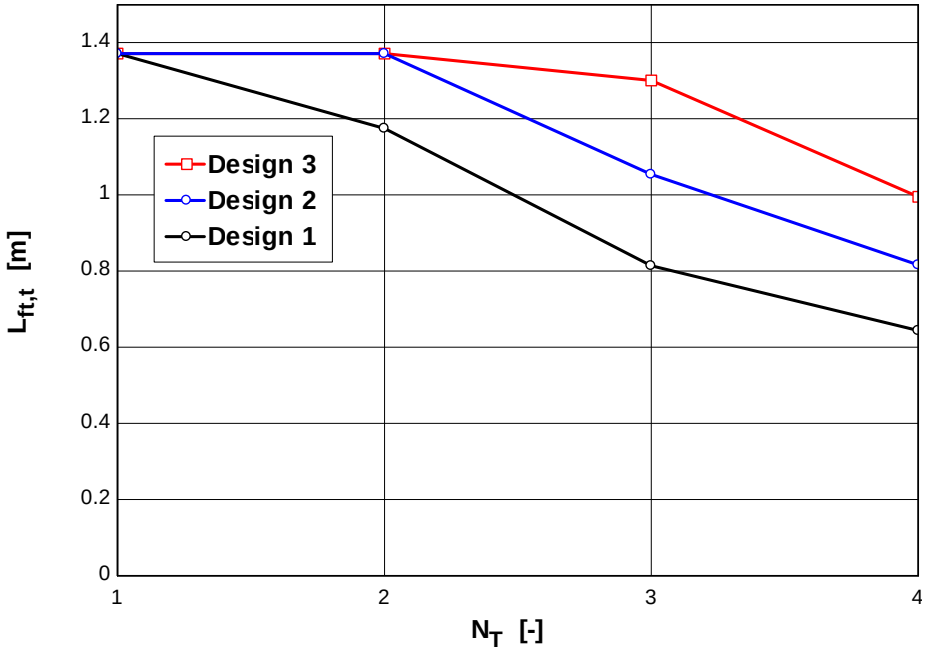

Figure 2.36: Maximum finned tube length for the mandrel length of 0.315 m.

For designs 2 and 3, the increase in refrigeration power for the 3 tube cases are a direct result of an increase in the conductance; Figure 2.37 illustrates the conductance as a function of mass flow rate for various numbers of tubes using the largest mandrel (Design 3). Note that increasing from 2 to 3 tubes increases the conductance while the conductance of the four tube design is actually slightly less than the 3 tube design because of the slight reduction in the mass flow rate per tube and therefore the heat transfer coefficient.

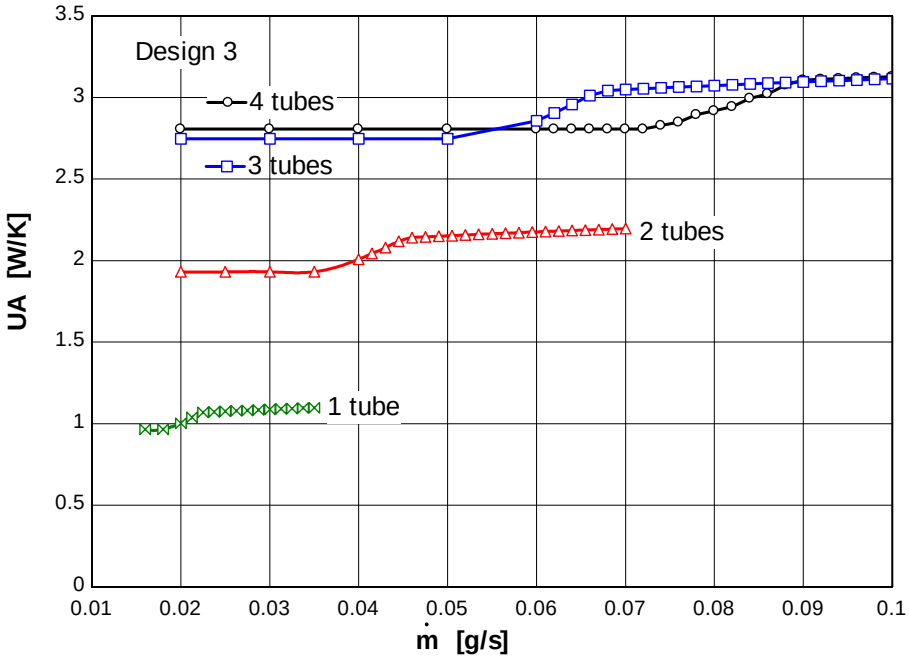

Figure 2.37: Conductance as a function of mass flow rate for various numbers of tubes and a 12.7 mm (0.5 in) mandrel (Design 3).

As predicted earlier, the increase in the axial conduction loss due to adding finned tubes is small compared to the increase in axial conduction caused by the mandrel diameter. Figure 2.38 illustrates the rate of conductive heat leak as a function of the number of tubes for the various mandrel sizes (i.e., designs). Note that the dominant conduction path is through the shell and tube rather than through the finned tubes and therefore the size of the mandrel has a larger effect on the axial conduction penalty than the number of finned tubes (recall that the mandrel length is fixed for this analysis).

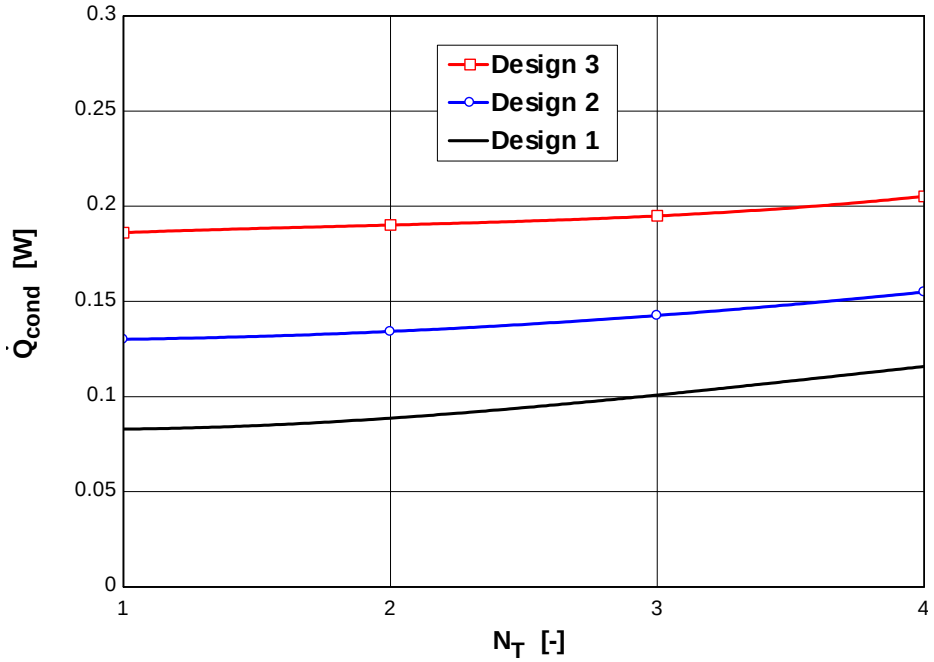

Figure 2.38: Axial conduction loss as a function of the number of finned tubes for various mandrel diameters.

Based on the preceding analysis, Device B utilizes a 12.7 mm (0.5 in) mandrel with a 3 tube design; the geometry is summarized in Table 2.12.

Table 2.12: Shell and mandrel for Device B.

Design	Device B
ID_{ot}	18.59 mm (0.732 in)
t_{ot}	0.254 mm (0.010 in)
OD_{it}	12.32 mm (0.485 in)
t_{it}	0.203 mm (0.008 in)
$Annular_{tol}$	0.279 mm (0.011 in)

The predicted cooling performance for device B as a function of mass flow rate is shown in Figure 2.39.

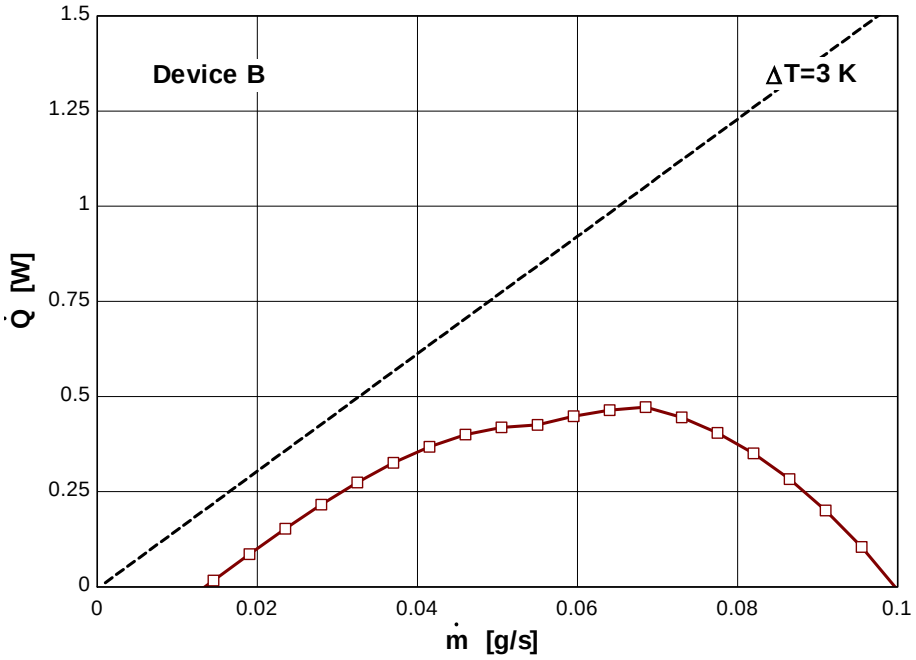

Figure 2.39: Predicted refrigeration as a function of mass flow rate for Device B.

Device B can provide more than 400 milliwatts of refrigeration at a flow rate of approximately 0.08 g/s. Both the refrigeration and the mass flow rate have been increased by a factor of four; therefore, it is expected that the fluid management issues seen for Device A will not be present.

Chapter 3 Experimental Testing

3.1 Device A Fabrication

This chapter explains the experimental results obtained from testing Device A. For convenience, the results are explained in detail in sections 3.1 to 3.4 and are also summarized in section 3.5. The fabrication of Device A is now discussed. The major fabrication tasks associated with assembling the heat exchanger components for Device A included wrapping the finned tube, sealing the hot stream from the cold stream, and sealing the shell, mandrel, and heat exchanger ports.

The major risk associated with wrapping the finned tube is that the thin-walled tube may become crimped as it is bent. The mandrel was cut slightly longer than its design length and welded to a 50.8 mm (2 in) long, 6.35 mm (0.25 in) diameter round bar on one end; this bar was held in the chuck of a lathe while the other end was held using a rotating center. After the mandrel was secured, one end of the finned tube was taped to the lathe chuck at nearly a 45^{o} angle from the axis of the mandrel. One person turned the lathe by hand (while it was in neutral) in order to begin the process of wrapping the tube while a second person held the unwrapped fin tube and focused on achieving the desired pitch. The pitch must be approached gradually in order to orient the ends of the finned tube in the axial direction for assembly into the shell and inlet/outlet ports. During the wrapping process for Device A, the last 0.184 m (7.25 in) of finned tube became crimped and broke off. This reduced the overall length available for the heat exchanger but did not prevent the completion of the construction of the Device.

Though the finned tube has a very small diameter and wall thickness, it was found that this size tubing could be soldered to the gasket of a VCR gland in order to provide a robust and hermetic seal. This is illustrated in Figure 3.1.

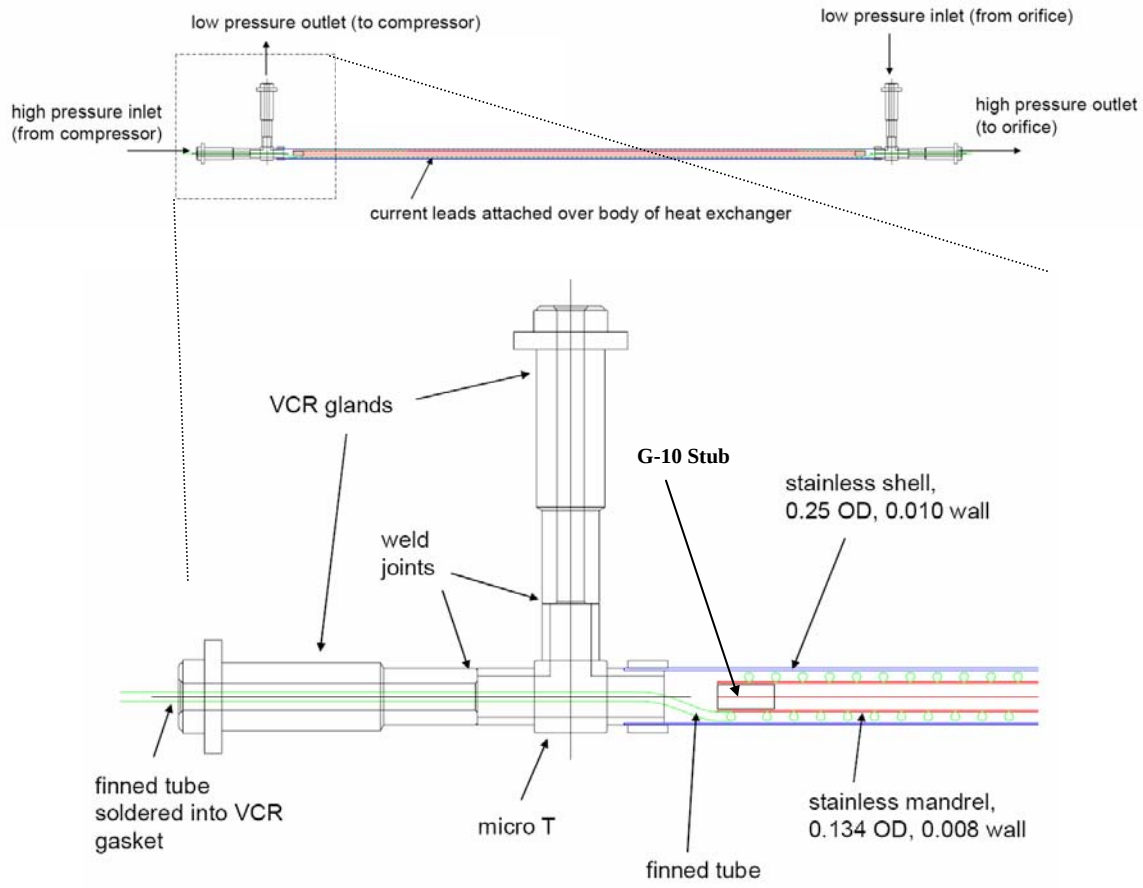

Figure 3.1: Design of Device A.

To seal the inner diameter of the mandrel from the working fluid, G-10 stubs were glued with Stycast into the ends of the mandrel. The remaining fabrication steps were accomplished by welding the stainless steel VCR glands, shell, and micro T's together. The length of the finned tube from the end of the mandrel to the VCR gasket is not considered part of the heat exchanger as was discussed in Chapter 2. This length is

approximately 0.076 m (3 in) on each end. The length of finned tube available for the heat exchanger was reduced from 1.32 m (51.8 in) to 1.14m (44.8 in) due to the length required by the assembly as well as the crimping loss.

Following assembly, the device was exposed to pressures that were 1.5x the maximum anticipated operating pressure in order to verify the integrity of the structure and joints. Subsequently, the device was cleaned and leak checked using a helium mass spectrometer. Both hot and cold sides were tested and found to be leak tight to within the sensitivity of the instrument.

To operate efficiently, the valve for the system must be capable of controlling a very small flow rate (on the order of 0.01 g/s). Additionally, due to the small refrigeration capacity of Device A, very little heat leak to the cold end can be tolerated. To operate at these target flow rates and to avoid the heat leak that would be associated with a valve handle, a fixed orifice expansion valve was assembled using orifices obtained from the Bird Precision Company. These orifices are made of ruby or sapphire and have very small, precisely cut holes through their centers. VCR gaskets were prepared that allowed the orifices to be inset and glued in place. The orifice diameters that were used ranged from 0.025 mm (0.001 in) to 0.381 mm (0.015 in). The drawback to the fixed orifice is that the process of changing the flow rate is relatively time consuming compared with a valve as the entire system must be warmed up and partially disassembled in order to replace the orifice.

3.2 Test Facility and Instrumentation

This section describes the facility that was utilized in order to carry out a component level test of Device A (i.e., a performance test of the heat exchanger that was independent of the JT cycle). The components utilized specifically for open and closed cycle operation will be discussed in their respective sections. The facility consists of a vacuum space, temperature and pressure sensors, a flow measurement device, and a liquid nitrogen bath. A schematic of the facility is shown in Figure 3.2.

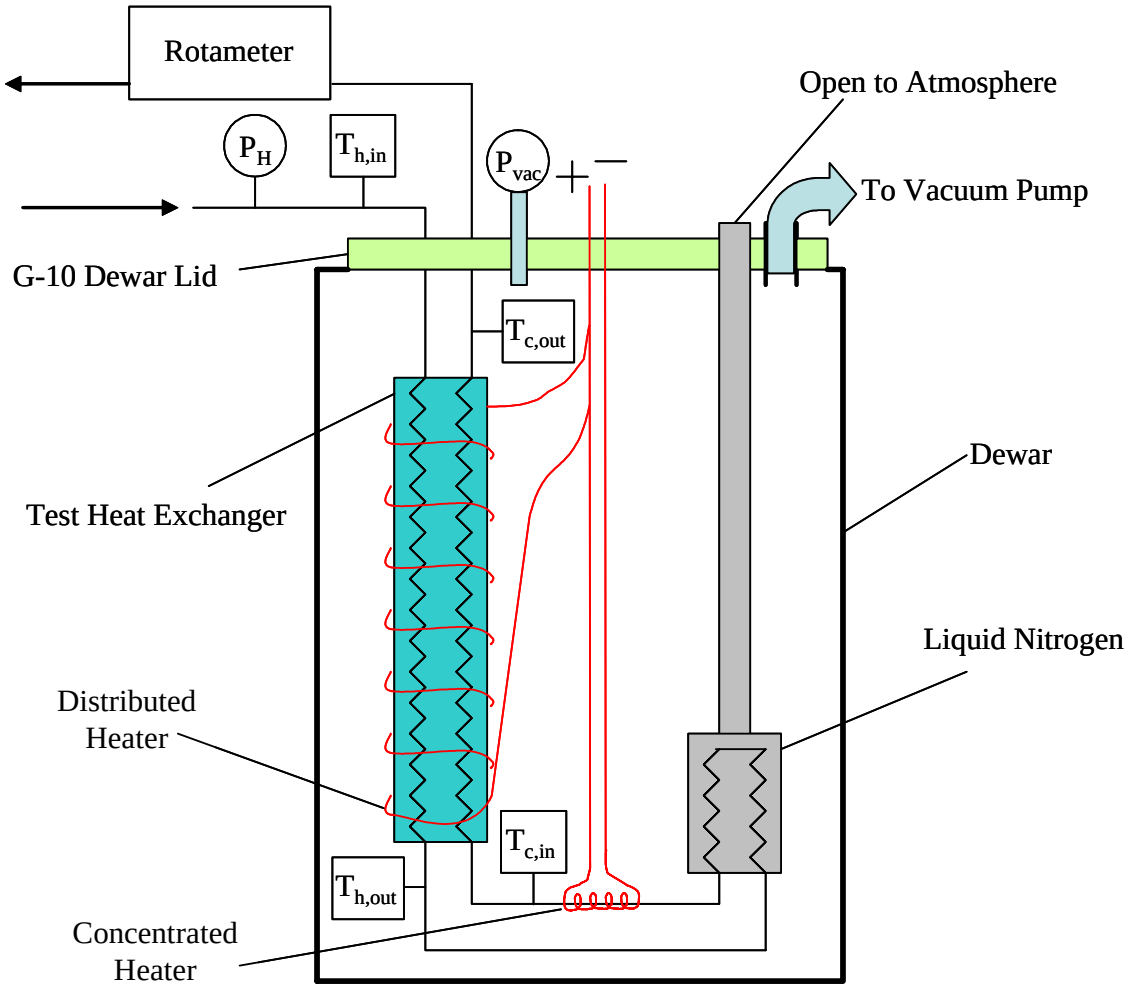

Figure 3.2: Test facility schematic.

The cryostat lid was fabricated from G-10, an epoxy/fiber composite, because of its low thermal conductivity and high strength. The circular cap was cut, free hand, out of 1 inch thick G-10 stock material on a vertical band saw and clearance holes were installed to affix the lid to the Dewar. The seal of the vacuum space is accomplished using an O-ring (12.5" ID, 0.25" cord width) between the G-10 lid and the top lip of the Dewar. During testing the vacuum space is maintained at a pressure of less than 1e-4 Torr (as measured by a Pirani gauge (P_{vac})) using a Leybold manufactured TOPS 151/361 Turbomolecular Pumping System (www.leybold.com). The flow rate was measured using a 0-50 SCFH Dwyer rotameter (model#: RMC-101-SSV) with an uncertainty of ± 2% full scale or ± 1 SCFH.

The fluid temperature measurements for both open and closed cycle testing were obtained using Platinum Resistive Temperature detectors (Platinum RTDs or PRTs, Model PT-111 uncalibrated PRTs, Lake Shore Cryotronics www.lakeshore.com). A polynomial function that yields temperature for a given resistance was generated using the standard PRT characteristic data. The accuracy of these devices can be improved by carrying out a simple, 2-point calibration of the PRTs prior to installing them in the facility. Liquid nitrogen at atmospheric pressure and a distilled ice bath were used as the two calibration temperatures. A 4-wire resistance measurement using a 1.0 milliamp current source and a Hewlett Packard 3468B Multimeter were used to carry out the calibration. Each of the PRTs was submerged in liquid nitrogen and distilled ice water; the discrepancy between the standard PRT curve and these data was corrected according to a linear function that was subsequently developed for each PRT. At a given resistance, this linear function is

the difference between the actual temperature and the temperature that is predicted based on the manufacturer's data; the correction can be incorporated into the original temperature-resistance polynomial to obtain a better approximation to the actual fluid temperature. All of the temperature measurements were recorded using a LabView Virtual Instrument (VI) integrated with a National Instruments PCI-6034E Data Acquisition card (DAQ).

The PRTs have VCR connections welded to them and therefore they can be directly connected to the heat exchanger's inlet and exit fluid ports which utilize matching VCR fittings. The PRTs are therefore not permanently attached to any one point in the test facility and can be moved depending on the type and size of the heat exchanger that is installed. Each PRT is inserted into the fluid stream and the effect of the wire heat leak is minimized using a thermal stand off from the flow tube. The four wires associated with each PRT exit the fluid space through an epoxy seal; a copper cap with a diameter that is larger than the tubing was filled with epoxy and the end of each tube was inserted into the cap after which the epoxy was allowed to harden. One of the temperature measurement fixtures is shown in Figure 3.3.

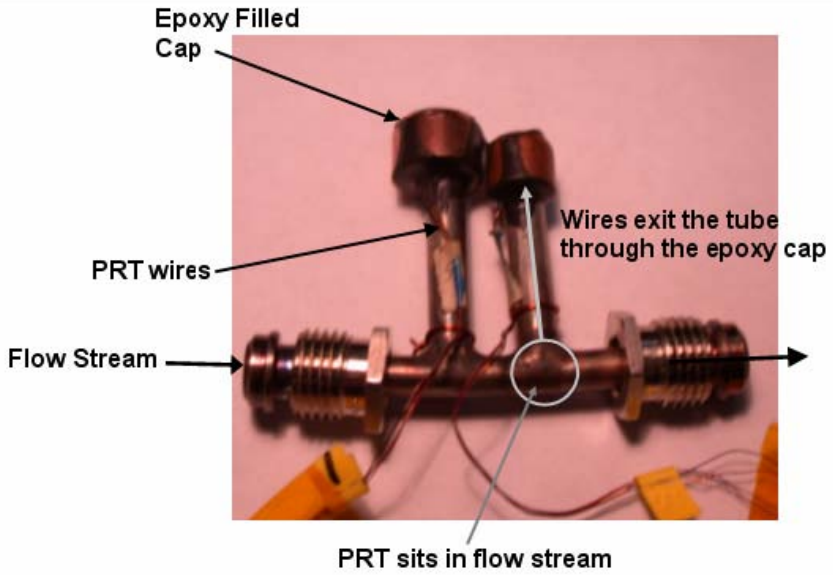

Figure 3.3: Temperature measurement fixture for PRT.

Two separate nichrome wire heaters (30 gauge) were installed within the facility; one at the cold end and the other distributed along the length of the heat exchanger. The maximum electric current which can be applied to this wire without failure is 1.8 Amps. For the lengths installed, this maximum current corresponds to a nominal maximum power of 71 W for the distributed heater and 34 W for the cold end heater. Finally, to minimize radiation heat leak, the heat exchanger, temperature fittings, and process tubing were encased in 10 layers of MLI.

The preliminary verification of the test facility was carried out using helium as the working fluid, in order to eliminate the uncertainty associated with the eventual multicomponent, multiphase flow required by the JT system. In addition, a tube-in-tube heat exchanger is employed in place of Device A to allow the performance of the test facility (i.e., the ability to take precise measurements and limit the parasitic heat load) to

be evaluated in isolation from the heat exchanger. The tube-in-tube heat exchanger is composed of stainless steel tubing purchased in the standard sizes shown in Table 3.1.

Table 3.1: Tube-in-tube dimensions

Tube	OD	Wall thickness	Length
Inner tube	4.76 mm (0.188 in)	0.89 mm (0.035 in)	unknown
Outer tube	7.94 mm (0.313 in)	0.89 mm (0.035 in)	0.50 m (19.7 in)

After placing the headers on the outer tube, the effective length for heat transfer is nominally 0.48 m (18.9 in). The end of the heat exchanger with VCR fittings welded in place is shown in Figure 3.4 (the MLI has been removed for the picture).

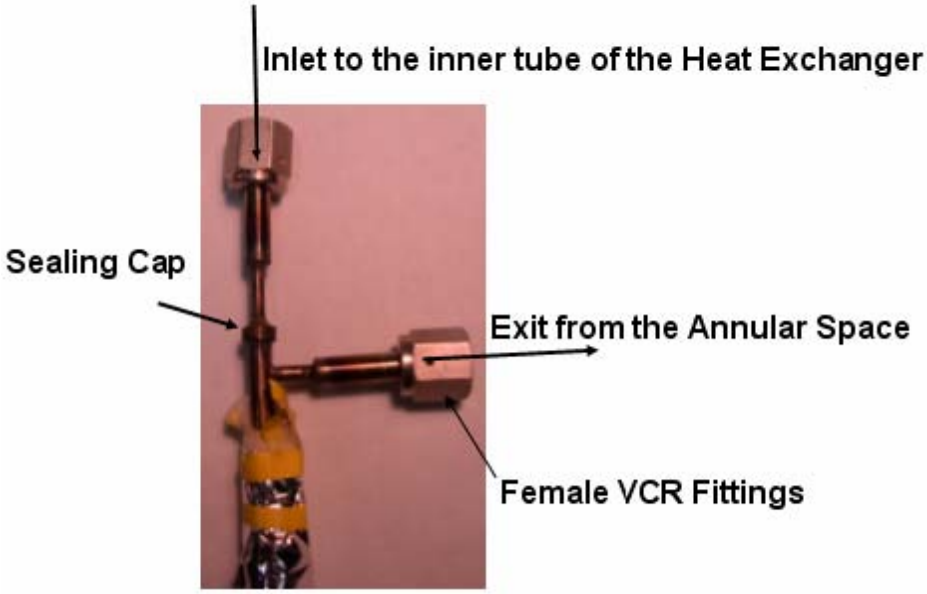

Figure 3.4: One end of the tube-in-tube heat exchanger used for the shake-down testing.

The liquid nitrogen bath was filled so that the cold inlet temperature is between 80 and 100 K depending on flow rate. Data were taken over a range of flow rates at steady state conditions. The data are summarized in Table 3.2.

Table 3.2: Data from Tube-in-Tube testing

Measurement	Unit	Data Point			
		1	2	3	4
$T_{hot,in}$	K	291.50	292.87	293.39	293.16
$T_{hot,out}$	K	116.1	123.9	135.9	150.6
$T_{cold,in}$	K	94.1	84	81.53	80.19
$T_{cold,out}$	K	269.91	256.02	241.13	224.53
$\dot{V}$	SCFH	4.6	9.3	14.2	20.5

These data provide a check on the ability of the test facility to make accurate measurements. The rotameter reading is used to calculate the mass flow rate ($\dot{m}$). The heat transferred from the hot stream to the cold stream can be computed based on an energy balance carried out on the hot fluid ($\dot{Q}_{hot}$ and $\dot{Q}_{cold}$, respectively). An energy balance on the hot side leads to

$$\dot{Q}_{hot} = \dot{m}\, c_P \left(T_{hot,in} - T_{hot,out} \right) \tag{3.1}$$

where c_P is the constant pressure specific heat capacity of helium gas. An energy balance on the cold side using the measured cold exit temperature leads to

$$\dot{Q}_{cold} = \dot{m}\, c_P \left(T_{cold,out} - T_{cold,in} \right) \tag{3.2}$$

The agreement of these energy flows represents the degree to which parasitic heat transfers have been controlled within the test facility and the accuracy of the temperature measurements. The difference between these energy transfers is reported in Table 3.3 and represents about 1% of the total heat transferred. The maximum possible heat transfer rate that can be achieved ($\dot{Q}_{max}$) with helium as the working fluid is:

$$\dot{Q}_{max} = \dot{m}\, c_P \left(T_{h,in} - T_{cold,in} \right) \tag{3.3}$$

The effectiveness, defined as the ratio of the heat transferred between the streams to this maximum possible heat transfer, can be calculated using each of the energy balances; these values are also reported in Table 3.3.

Table 3.3: Reduced data for Tube-in-Tube heat exchanger.

Measurement	**Unit**	**Data Point**			
		1	2	3	4
$\dot{m}$	g/s	0.016	0.0322	0.049	0.071
$\dot{Q}_{hot}$	W	14.55	28.35	40.35	52.72
$\dot{Q}_{cold}$	W	14.59	28.86	40.88	53.38
ε_{hot}	-	0.888	0.808	0.743	0.669
ε_{cold}	-	0.890	0.823	0.753	0.677
Energy Balance Error	W	0.04	0.51	0.53	0.66
Energy Balance Error	%	0.2	1.7	1.3	1.3

The tube-in-tube heat exchanger was replaced with Device A and the same tests were performed in order to obtain 11 steady state data points. The inlet pressure was measured using a 0-2000 psig (0-13.79 MPa) pressure gauge with an uncertainty of ±20 psig (137.9 kPa). The data are shown in Table 3.4 below.

Table 3.4: Flow rate and temperature data from helium testing with Device A.

$\dot{m}$	$T_{hot,in}$	$T_{hot,out}$	$T_{cold,in}$	$T_{cold,out}$
(g/s)	(K)	(K)	(K)	(K)
0.004911	287.7	160.9	125.8	282.1
0.00912	287.9	144.4	116.2	282.4
0.01087	288.6	131.4	104.3	283.4
0.01508	292.9	104	89.81	288.6
0.01614	292.4	125	101	288.3
0.0214	294.3	106.1	90.67	289.9
0.02175	294.4	111.8	93.24	289.9
0.02876	293.1	99.71	86.48	289.3
0.03087	293.2	93.85	83.02	288.2
0.03297	294.9	97.48	84.81	289.8
0.03683	295.1	95.82	83.58	289.7

Figure 3.5 illustrates the measured effectiveness (based on the cold side heat transfer) as a function of the mass flow rate. Note that the ineffectiveness first decreases with mass flow rate as the heat transfer rate overcomes axial conduction and then increases as the number of transfer units in the heat exchanger decreases. This is the expected behavior of the heat exchanger as it exhibits a very low ineffectiveness which is necessary for the actively cooled current lead device.

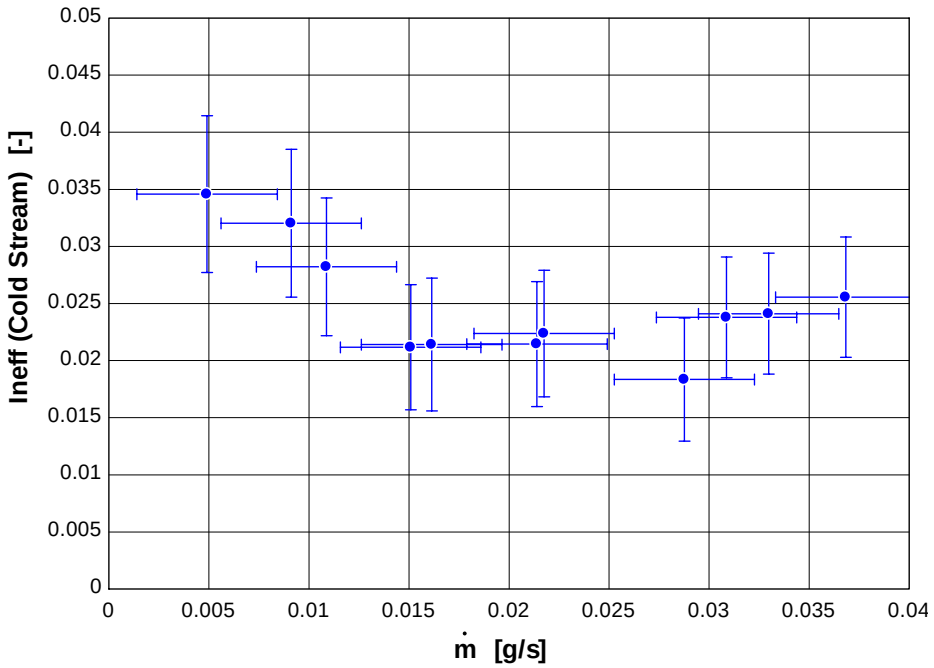

Figure 3.5: Ineffectiveness based on the cold stream heat transfer rate as a function of the mass flow rate for Device A while operated with pure helium and cooled with liquid nitrogen.

The energy balance error for Device A is shown in Figure 3.6 as a function of mass flow rate. From this figure, we see that the parasitic heat load on Device A is nominally 1.25W.

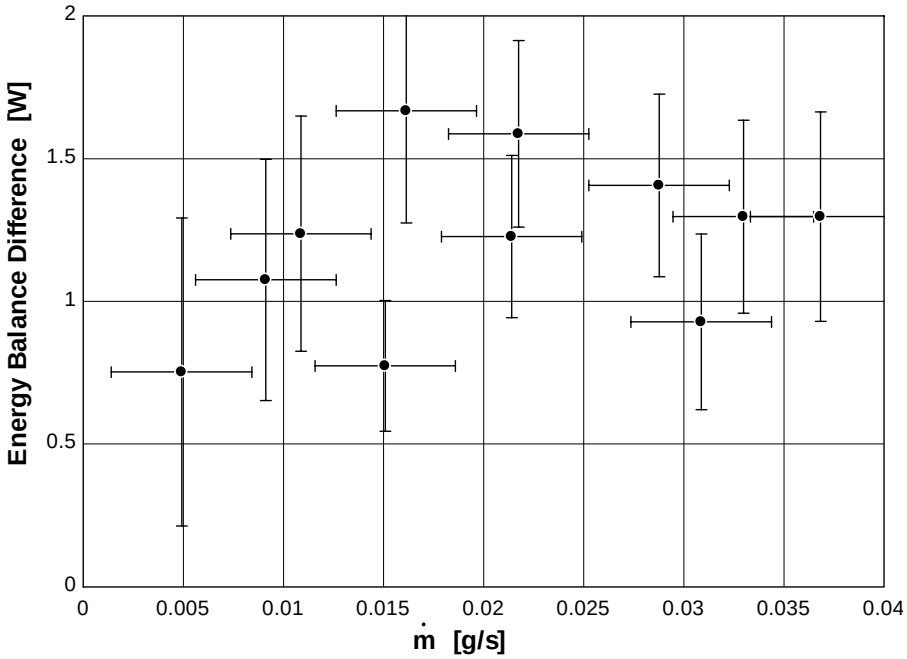

Figure 3.6: Difference between measured cold and hot stream heat transfer rate as a function of the mass flow rate for Device A while operated with pure helium and cooled with liquid nitrogen.

In addition, the data from these helium tests can be used to directly compare the conductance of the heat exchanger with predictions from the detailed model. The *ε-NTU* portion of the cycle performance model is utilized to infer the heat exchanger conductance. The low pressure of the cold stream was not measured during the helium tests so it is assumed to be 101.325 kPa (14.7 psia) as there should be very little flow resistance on the cold side of the heat exchanger at these flow rates. Figure 3.7 shows this comparison as a function of mass flow rate.

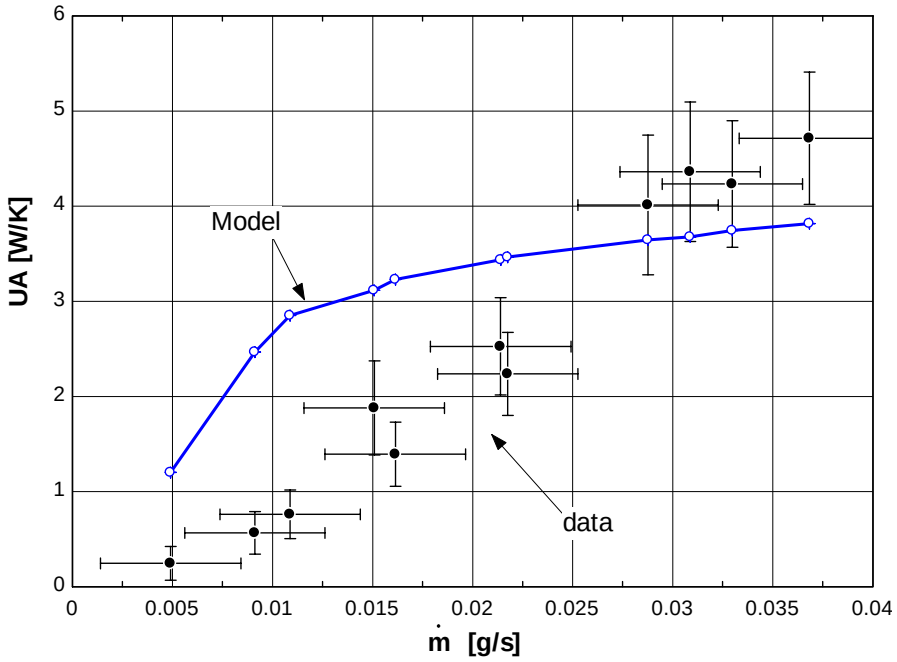

Figure 3.7: Heat exchanger conductance as predicted be the detailed model and based on the cold stream heat transfer rate from the helium test data.

The greatest discrepancy between the model and the data is at lower flow rates (less than 0.02 g/s). In examining the results of the detailed model, the cold stream Reynolds number for the temperature range of the heat exchanger is below 300 [-] for all mass flow rates and therefore, the heat transfer correlation used by the model throughout the heat exchanger is Nu_c = 3.66. The hot stream Reynolds number is shown in Figure 3.8 for a number of the mass flow rates associated with the experiment. Note that all of the model predictions for mass flow rates greater than 0.005 g/s employ a turbulent heat transfer correlation (see Table 2.4) as the Re_h is greater than 2,300.

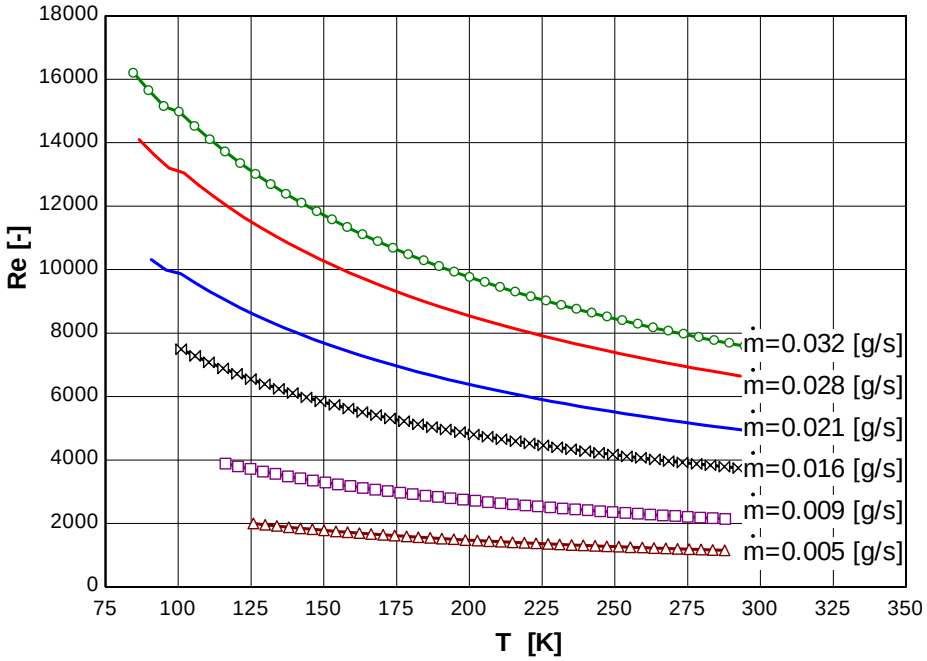

Figure 3.8: Predicted hot stream Reynolds number as a function of the assumed linear temperature profile and mass flow rate for Helium test data.

Employing a more conservative correlation for the hot stream low Reynolds number range (2,300 < Re < 10,000) by Gnielinski (Incorpera and DeWitt, 2004),

$$Nu_h = \frac{(f/8)(Re_h - 1000)Pr}{1.07 + 12.8(f/8)^{1/2}\left(Pr^{2/3} - 1\right)} \tag{3.4}$$

where f is the friction factor defined as,

$$f = \left(0.790\ln(Re) - 1.64\right)^{-2} \tag{3.5}$$

provides better agreement for the lower mass flow rates, as seen in Figure 3.9

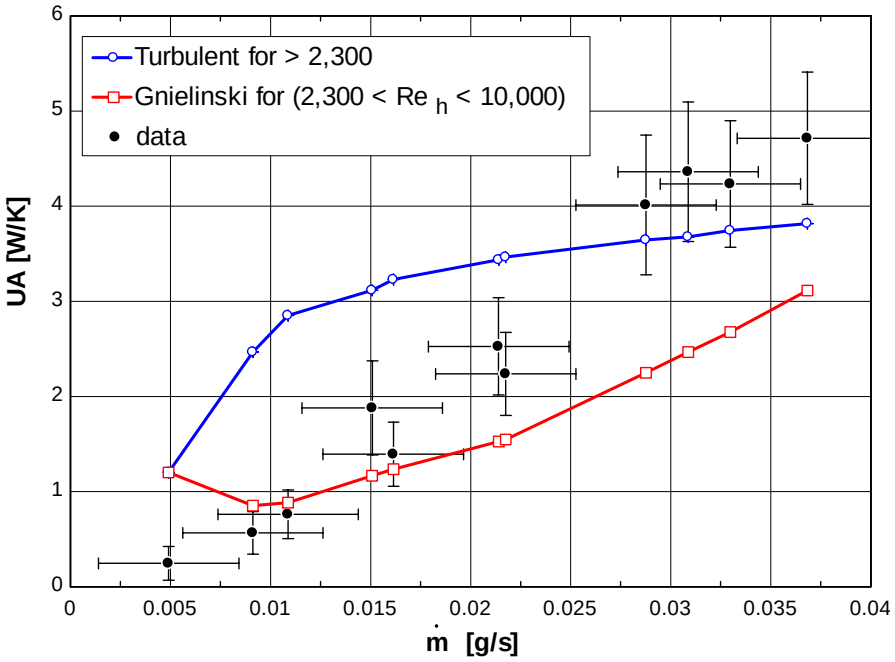

Figure 3.9: Heat exchanger conductance correlation comparison.

Though the original detailed model over-predicts the heat exchanger conductance for single-phase heat transfer the prediction is likely still an under-estimate of the heat transfer for a two-phase mixture. Therefore, the model will continue to use the turbulent correlation, until mixture data shows that it is inappropriate.

It is suspicious that for the mass flow rate of 0.005 g/s, the model prediction of the heat exchanger conductance is still an over-estimate, even though the model employs the laminar Nusselt correlation of $Nu = 3.66$ for both streams over the entire temperature range. Inspecting the parasitic heat load predicted by the energy balances of Eq. (3.1) and (3.2) for the helium data, the parasitic heat load represents a larger percentage of the heat transferred for the low mass flow rate cases, as seen in Figure 3.10, and therefore it

is likely that the discrepancy is related as much to measurement error as modeling inaccuracy.

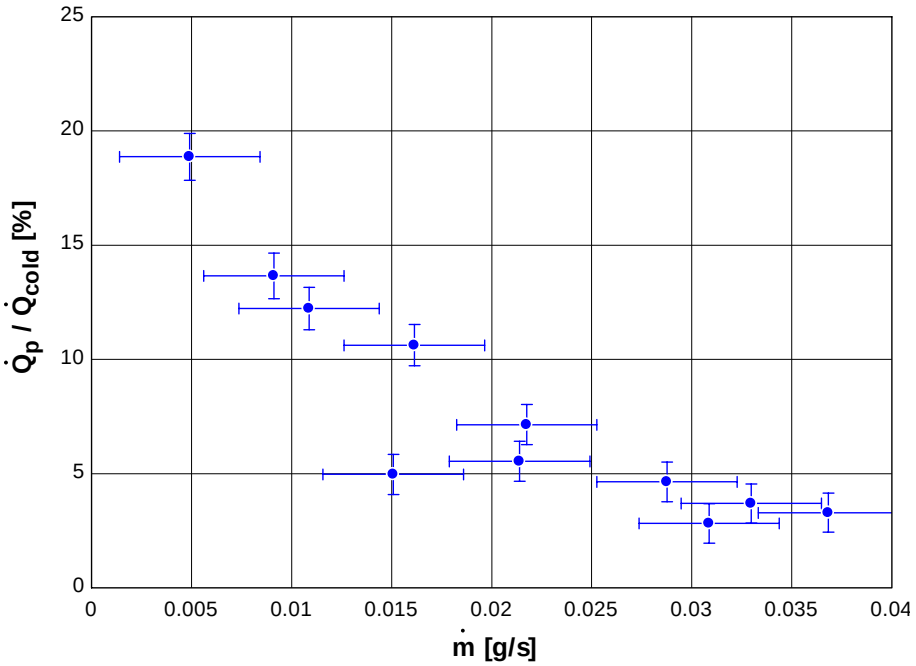

Figure 3.10: Percentage of the parasitic heat load relative to the cold stream heat transfer.

Further Helium data were taken to compare the hot stream pressure drop to the pressure drop prediction of the detailed model. The 0-10 SCFH rotameter was replaced by a Dwyer 0-10 SCFH rotameter (Model#: RMC-121) with an accuracy of 2% full scale or 0.2 SCFH. The inlet pressure was measured with a (0-300 psig) gauge with an accuracy of 2% mid-scale or 3 psig (21 kPa). Again, the low pressure of the cold stream was assumed to be near atmospheric pressure (14.7 psia). The data and the model prediction are shown in Figure 3.11.

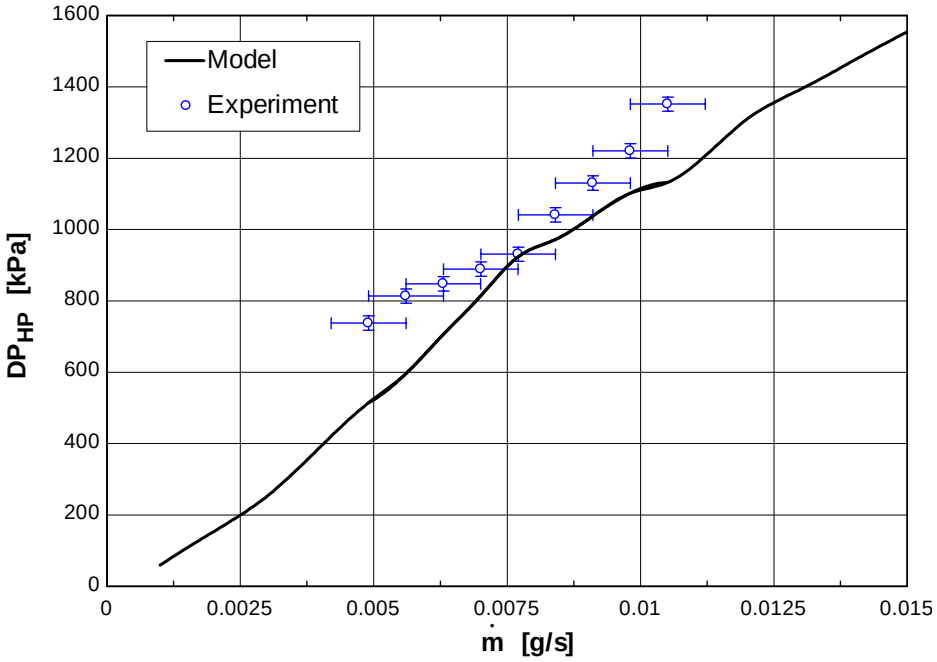

Figure 3.11: Hot stream pressure drop as a function of mass flow rate for Helium test data.

The model slightly under-predicts the pressure drop, as is expected considering that there will be some pressure drop due to the miscellaneous fittings associated with the test. Otherwise, the detailed model successfully captures the relationship between mass flow rate and pressure drop through the finned tube. In addition, the data shows that Device A has been correctly integrated and no blockage exists related to its construction.

3.3 Open JT Cycle Argon Testing

Encouraged by the low ineffectiveness measured for Device A as well as with the agreement between measured and predicted performance, the heat exchanger was tested with high pressure (1400 psig or 9.754 MPa), pure argon (99.999%) in an open JT cycle by replacing the liquid nitrogen bath with one of the 76.2 μm (0.003 in) diameter orifices that was discussed in section 3.1. A schematic of the facility for these tests is shown in Figure 3.12.

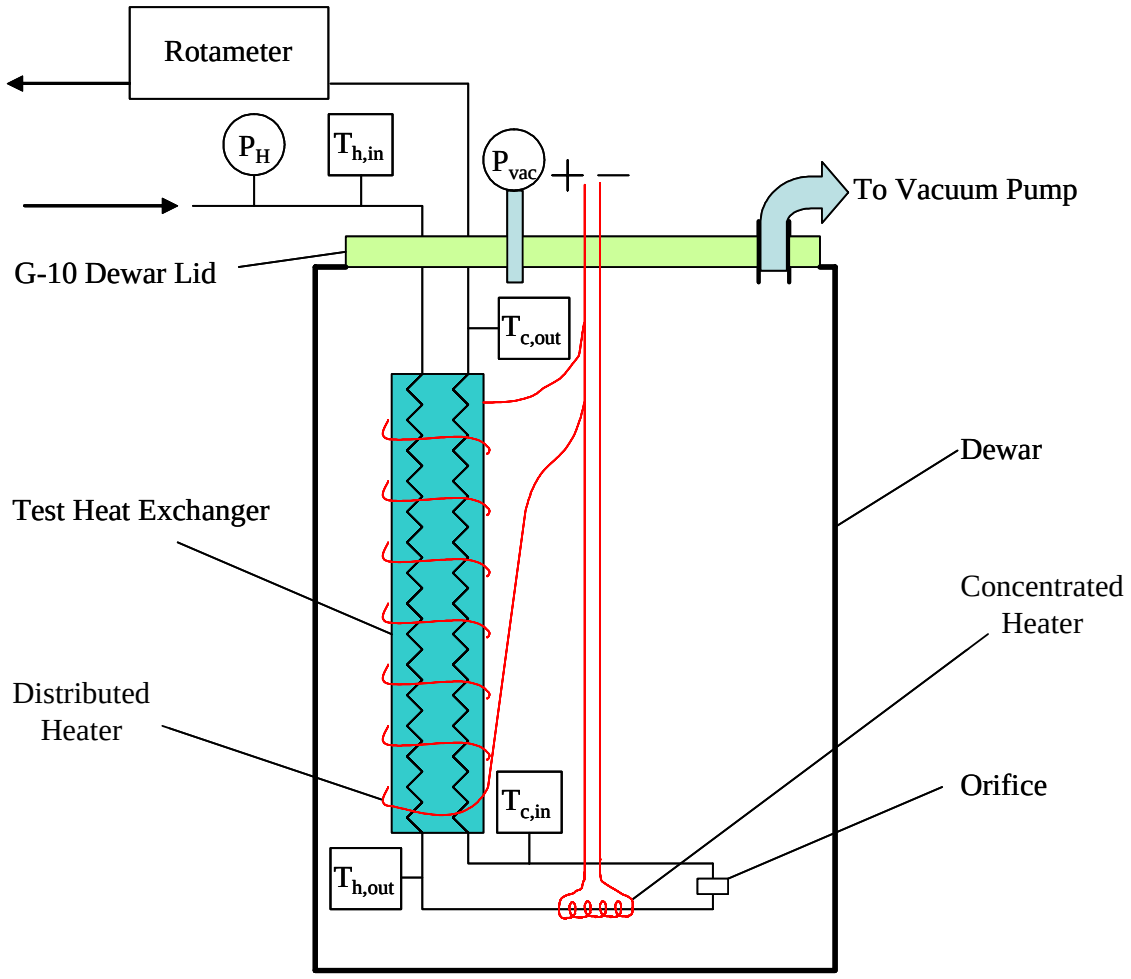

Figure 3.12: Facility schematic for open JT cycle experiments with pure argon.

The small diameter of the orifice placed a stringent constraint on the purity of the argon used for the tests. Several test runs had to be completely abandoned after the orifice became partially or completely blocked by contaminants in the gas stream. In order to remove the blockage, the facility had to be disassembled, and the blockage removed before testing could resume. Surviving these blockages were five steady state measurements with cold end heat loads varying from 0 W to 2.67 W. Since all of the runs employed an inlet pressure of 1400 psig (9.754 MPa) the mass flow rate for every run was 18 SCFH of air or 0.2 g/s of argon. The data and the model prediction are shown in Figure 3.13 as a function of the cold inlet temperature to the heat exchanger.

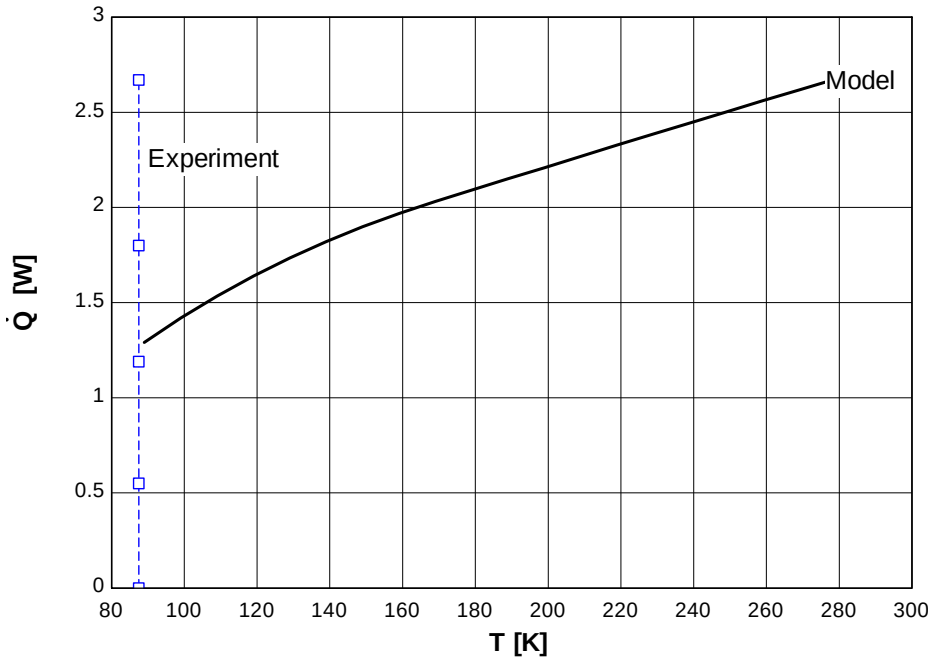

Figure 3.13: Cold end heat load as a function of the cold inlet temperature for open cycle argon tests employing 76.2 μm (0.003 in) orifice.

The model under-predicts the cooling power of Device A as it is operated with pure argon at this flow rate. Therefore, even though the helium tests showed that the model over-predicted the heat exchanger conductance for a single-phase working fluid, these

tests show that the model predictions are still an under-estimate of two-phase heat transfer. The argon test data is reported in Table 3.5.

Table 3.5: Steady state argon test data with 76.2 μm (0.003 in) orifice.

$\dot{Q}_{Load,cold}$ (W)	$T_{hot,in}$ (K)	$T_{hot,out}$ (K)	$T_{cold,in}$ (K)	$T_{cold,out}$ (K)	P_{inlet} (MPa)	$\dot{m}$ (g/s)
0	292.1	88.15	87.5	269	9.754	0.20
0.55	292.2	88.2	87.5	271.5	9.754	0.20
1.19	292.2	88.23	87.5	277.8	9.754	0.20
1.8	292.2	88.83	87.2	283	9.754	0.20
2.67	292.2	104.3	87.5	287.8	9.754	0.20

The heater power was nearly 2 W before the hot outlet temperature was raised significantly from 88.1 K. The ability of the system to receive this heat load and remain at 87.5 K at the cold inlet indicates that the quality of the working fluid at the cold inlet to the heat exchanger must be fairly low. This makes sense considering that the fluid will be a saturated liquid at the inlet to the orifice for the temperature and pressure of the hot outlet stream (see the T-h diagram in Figure 3.14). By taking the enthalpy difference at the hot end of the heat exchanger, the refrigeration provided by the argon test run is estimated.

Table 3.6: Enthalpy at heat exchanger ports and refrigeration estimate.

$h_{hot,in}$ (J/g)	$h_{hot,out}$ (J/g)	$h_{cold,in}$ (J/g)	$h_{cold,out}$ (J/g)	$h_{cold,out} - h_{hot,in}$ (J/g)	$\dot{Q}$ (W)
-21.87	-267.4	unknown	-15.4	6.467	1.289
-21.8	-267.3	unknown	-14.1	7.706	1.536
-21.8	-267.3	unknown	-10.8	11.01	2.196
-21.8	-266.6	unknown	-8.1	13.71	2.732
-21.8	-249.8	unknown	-5.6	16.2	3.229

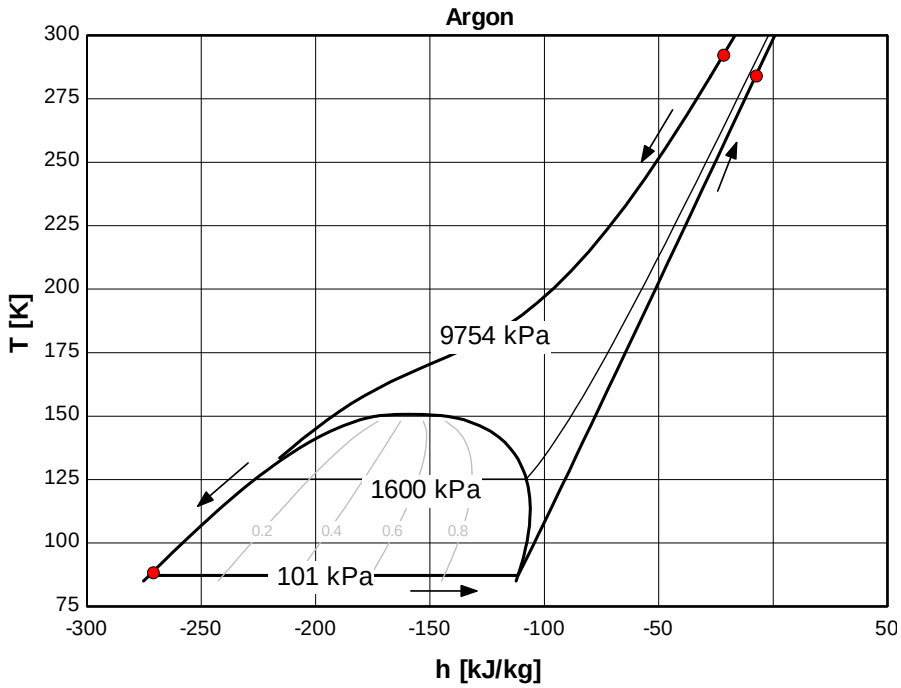

Figure 3.14: T-h diagram for argon and the approximate operating conditions of the open cycle.

In the hopes of reducing the common occurrence of contaminant blockage, the 76.2 μm (0.003 in) orifice was replaced with a 152.4 μm (0.006 in) orifice and a Swagelok filter (Model#: SS-4FW-VCR-2) was installed immediately upstream of the orifice. The filter contains a pleated mesh which removes 95% of the particles larger than the 2 μm pore size of the filtering element. The rated pressure drop for the filter is 10 psig for a flow rate of 10 SCFM of air. Therefore, the filter is not expected to interfere with the cycle in any significant way. Unfortunately, these efforts did not alleviate the occurrence of contaminant blockage and further consistent steady state data was not obtainable.

During the final testing with argon, high frequency electrical noise began interfering with the voltage signals from the PRT's. In an effort to determine the source of the interference, the test facility was moved to another building (Engineering Hall) and electrically re-connected to the same data acquisition system and the interfering signal was not found. From this it was concluded that the interference was not due to the integrity of the test facility and a new LabView Virtual Instrument (VI) was programmed to digitally filter the data from the PRTs in order to remove the high frequency noise.

3.4 Closed JT Cycle Testing

Following the pure argon tests, the facility was integrated with an APD compressor (model#:HC-2) and gas handling equipment to allow closed cycle testing with hydrocarbon mixtures to begin. In addition to these changes, the 0-50 SCFH rotameter was replaced by a 0-50 SLPM flow controller, a 0-800 psig pressure gauge replaced the 0-2000 psig pressure gauge at the inlet to the cryostat, and a (-14.7-200) psig pressure gauge was installed at the suction side of the compressor to measure the low pressure (P_L) of the system. Table 3.7 provides the specifications for these instruments. The mass flow controller is used only as a mass flow meter and was preferred because it could withstand higher pressures than the rotameter (500 psig rather than 100 psig).

Table 3.7: Pressure gauges for closed cycle testing.

Device	Range	Make	Uncertainty
P_H	0-800 psig	US Gauges	±1% (800 psig) = 8 psig
P_L	-14.7-200 psig	Wikai	±1% (200 psig) = 2 psig
Flow controller	0-50 SLPM	AALBORG (Model-GFC 37)	±2% (50 SLPM) = 1 SLPM

To operate the system in a closed cycle, the system must be filled with the desired working fluid to an intermediate pressure called the ‘charge pressure’. When compressor operation begins, the compressor discharges at higher pressure (less than 380 psig for this compressor) to the inlet of the cryostat and pulls a lower pressure at the outlet of the cryostat to force the fluid through the system. The compressor has two internal relief valves; one vents to the atmosphere if the pressure in the system exceeds 380 psig and the other opens if the pressure differential between the discharge and suction lines of the compressor exceeds 210 psig. The mixture components were assumed to be ideal gases

during the mixture build process; that is, the total charge pressure was reached by filling the system partially with each constituent according to its desired molar fraction. A schematic of the gas handling equipment is shown in Figure 3.15 (with the valves numbered 1-7).

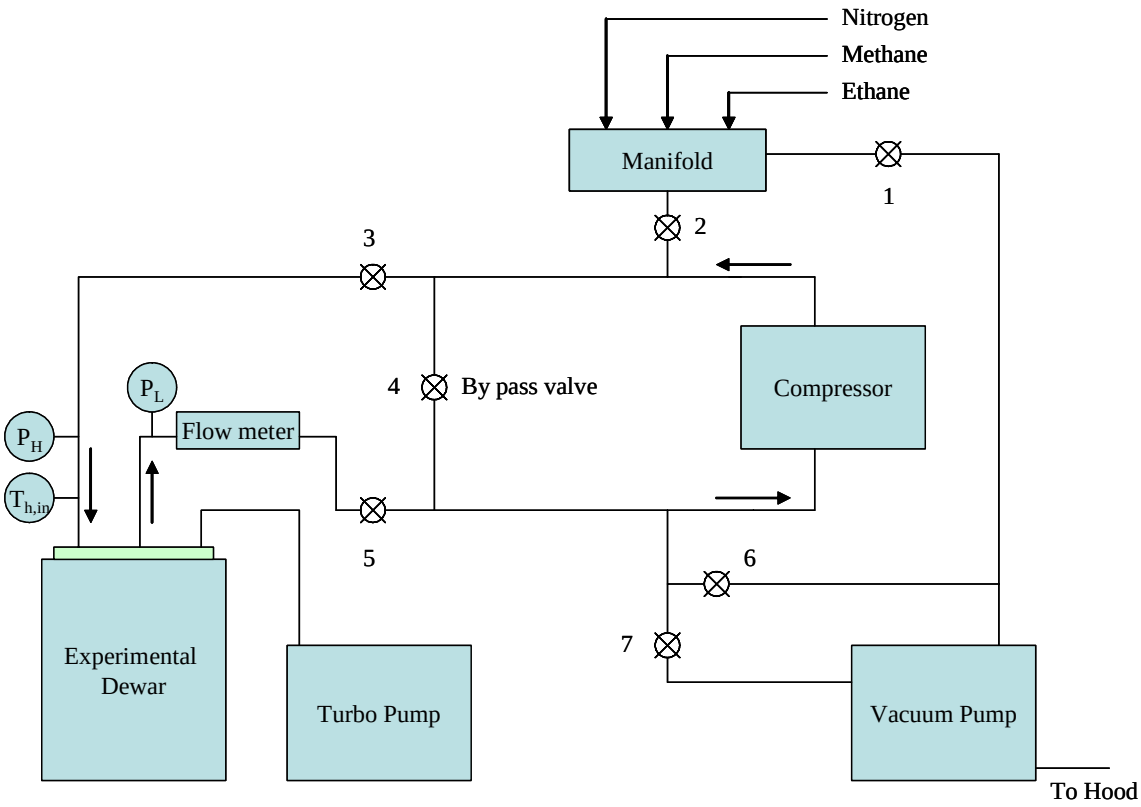

Figure 3.15: Gas handling equipment integrated with test facility.

Initial closed cycle operation with pure argon (99.999%) demonstrated that particulate contamination was not a constraint as it had been with open cycle testing. This was concluded after the system ran for several days without any blockage occurring.

3.4.1 Oct 26 – Nov 28, 2005

Three initial tests were performed with the design mixture (39% Nitrogen, 6% Methane, 55% Ethane) to determine the appropriate orifice size and charge pressure to enable the system to operate at the target pressures and mass flow rate. Ethane was found to be very soluble in the compressor oil, such that when the system was filled with ethane, the compressor oil absorbed enough ethane to substantially decrease the charge pressure. Therefore, the time required for the ethane charge pressure to stabilize was also determined during these initial test runs. Table 3.8 provides the specific operating conditions of the three test runs.

Table 3.8: Operating conditions for initial test runs using the design mixture.

Orifice size	P_{charge} (psig)	$\dot{V}$ (slpm)	P_H (psig)	P_L (psig)	$\dot{m}$ (g/s)
152.4 μm (0.006 in)	160	2.3	255	-10	0.039
101.6 μm (0.004 in)	160	2.1	255	-6	0.036
63.5 μm (0.0025 in)	236	0.8	315	65	0.014

After the first two runs, the pressure regulator on the ethane bottle was replaced to allow a higher charge or mixture pressure to be reached so that the low pressure of the system would still be above atmospheric pressure. The charge pressure of the ethane was found not to deviate significantly if three, thirty minute “mixing cycles” were accomplished during the building of the design mixture. This entailed charging the system with ethane, running the compressor for 30 minutes and then refilling to make up for the drop in charge pressure due to mixing of the ethane with the compressor oil. The flow rate for the 63.5 μm (0.0025 in) orifice was closest to the predicted optimum flow rate of 0.018

g/s (seen in Figure 2.31), therefore, this orifice was selected for further testing. The temperature data for each run is shown in Figure 3.16 through Figure 3.18.

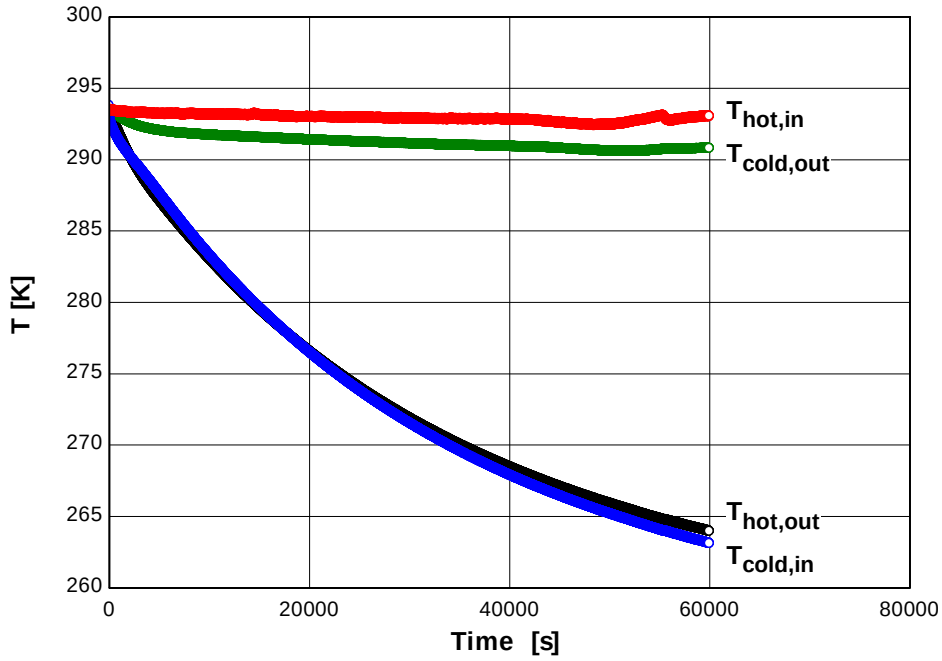

Figure 3.16: Temperature data for 152.4 µm (0.006 in) orifice.

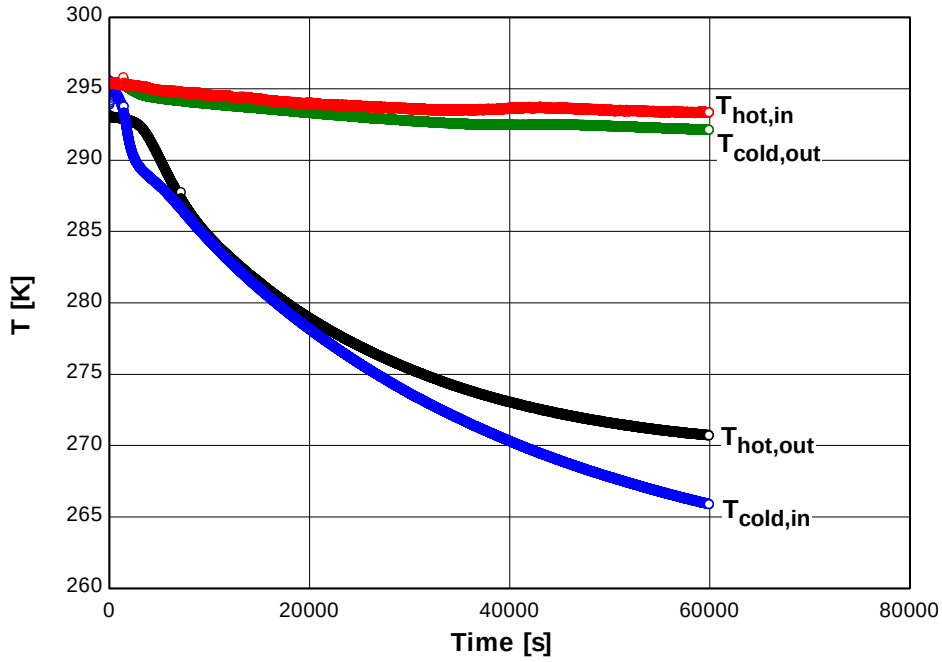

Figure 3.17: Temperature data for 101.6 µm (0.004 in) orifice.

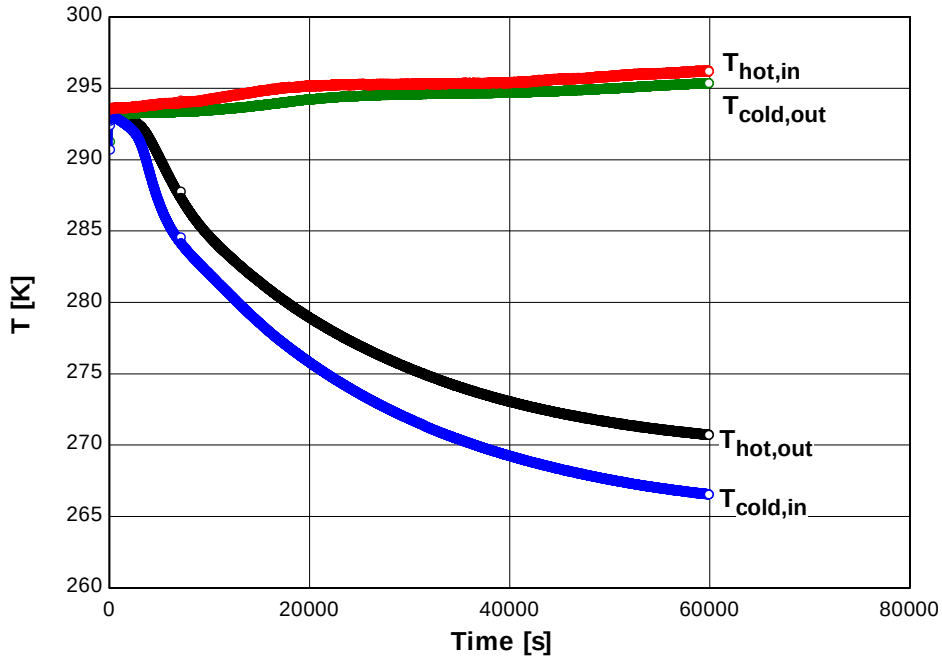

Figure 3.18: Temperature data for 63.5 μm (0.0025 in) orifice.

None of the test runs reached temperatures below 260 K. The parasitic heat load on the heat exchanger was too great for the refrigeration capacity of the device (100 mW). After obtaining this data, pressure gauges were installed at the inlet and outlet of the orifice to ensure that the pressure drop of the design mixture was not significantly different than what was observed for pure substances. These gauges are summarized in Table 3.9.

Table 3.9: Pressure gauges near orifice.

Pressure	Range	Make	Uncertainty
P_{H2}	0-800 psig	US Gauges	±1% (800 psig) = 8 psig
P_{L2}	0-100 psig	Setra transducer Model C204	±1% (100 psig) = 1 psig

In addition, it was concluded that to better isolate Device A from the parasitic heat load, the outer jacket of the experimental Dewar would be filled with liquid nitrogen. The ports for this jacket and the instrumentation discussed so far are shown in Figure 3.19.

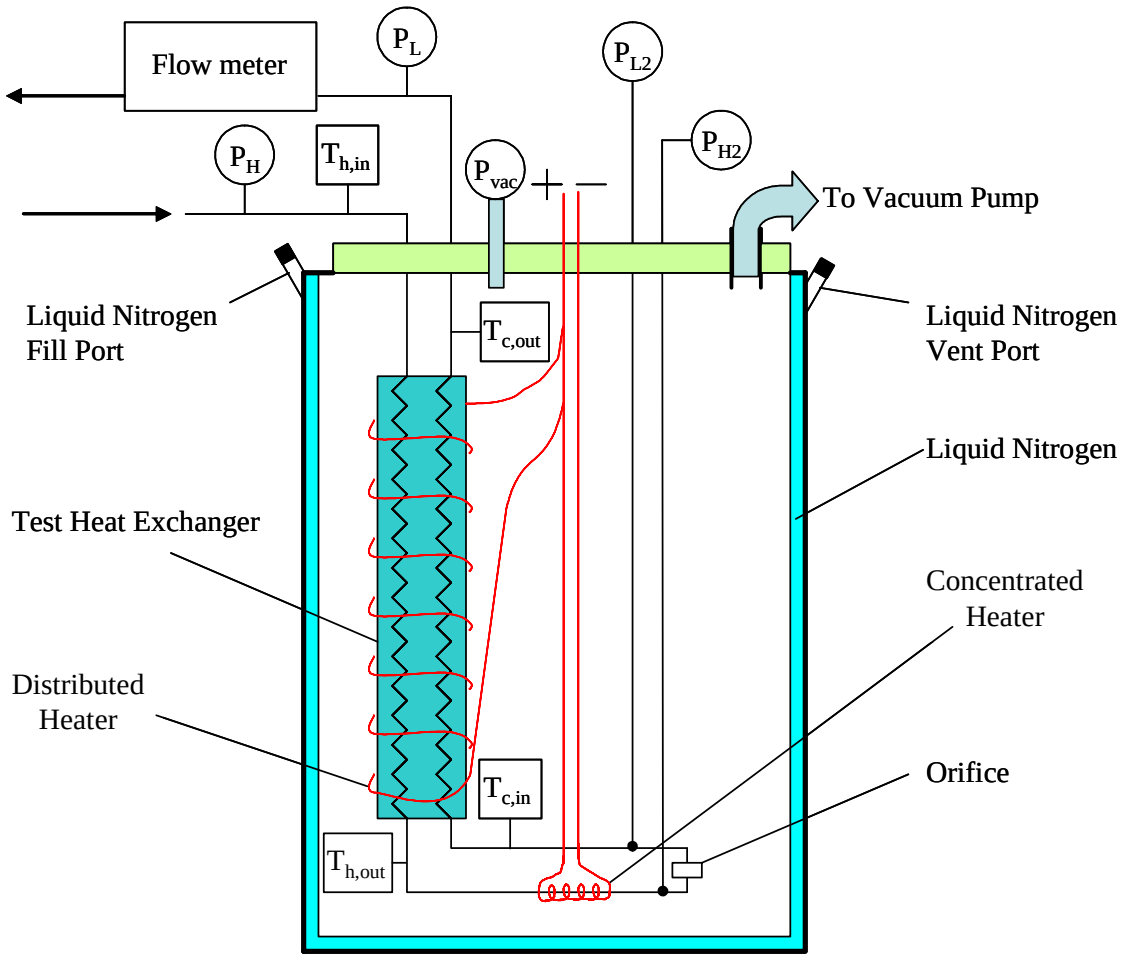

Figure 3.19: Facility schematic after initial closed cycle testing with design mixture.

Following these changes, another test was initiated on 11-21-05. (Due to the number of tests referred to in the remaining text, the tests will now be referred to by the date the test was initiated). The operating conditions for test run 11-21-05 are shown in Table 3.10 and the temperature data is shown in Figure 3.20.

Table 3.10: Initial operating conditions for Test 11-21-05.

Fluid	Design Mixture
Orifice size	63.5 μm (0.0025 in)
Charge Pressure	236 psig
$\dot{V}$	0.8 SLPM
P_H	315 psig
P_{H2}	267 psig
P_{L2}	65 psig
P_L	65 psig

The test began with the cold end temperatures near 270 K because the jacket was filled with liquid nitrogen before the test began. Due to the time required for the previous tests, Test 11-21-05 was run through the night as were most of the remaining test runs. The temperature data was recorded every 100 seconds.

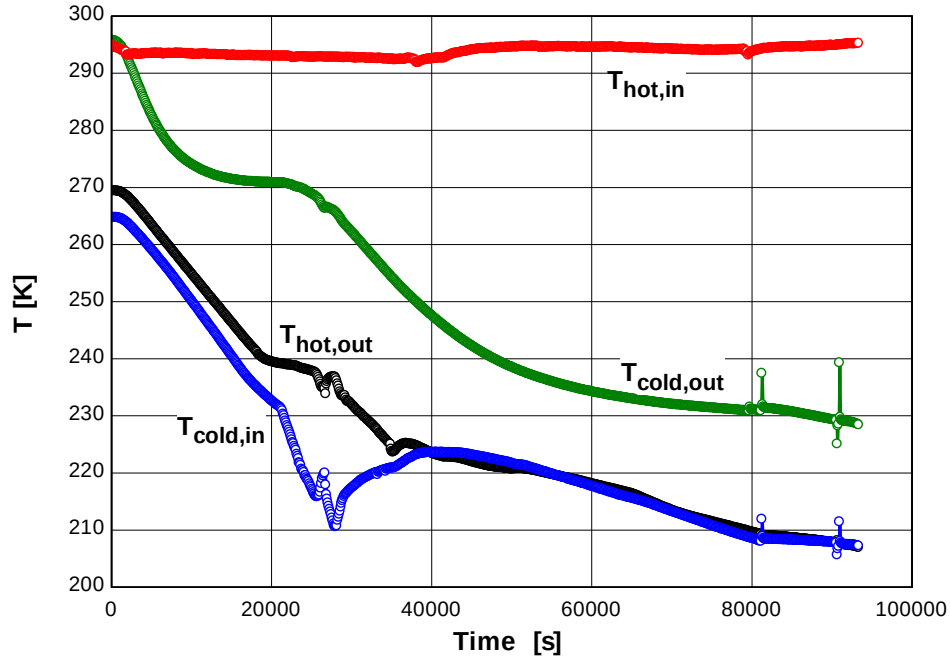

Figure 3.20: Temperature data for 11-21-05 test run.

The morning after the test began (11-22-05), the flow meter indicated that there was no flow. The compressor was cycled off and on with no effect on the flow rate (this is the

cause of the temperature spikes near 80,000 and 90,000 seconds). Considering the temperature profile of the cold inlet to the heat exchanger, the flow rate was most likely blocked near 30,000 seconds. Due to previous experience with particulate blockage during the pure argon tests, it was assumed that some contaminant was blocking the small 63.5 µm (0.0025 in) orifice. Therefore, the facility was disassembled and the larger 152.4 µm (0.006 in) orifice was installed after which another test was initiated. The operating conditions for test 11-28-05 are shown in Table 3.11.

Table 3.11: Initial operating conditions for Test 11-28-05

Fluid	Design Mixture
Orifice size	152.4 µm (0.006 in)
Charge Pressure	272 psig
$\dot{V}$	2.2 SLPM
P_H	352 psig
P_{H2}	212 psig
P_{L2}	98 psig
P_L	98 psig

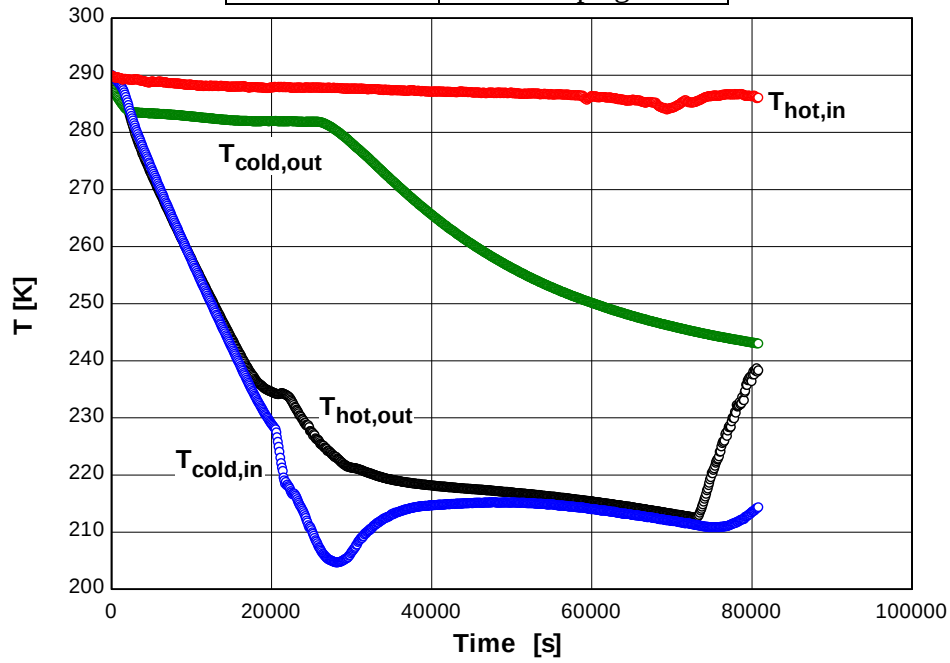

Figure 3.21: Temperature data for 11-28-05 test run.

Again, the flow rate was blocked during the run; most likely near the time that the temperature of the cold outlet of the heat exchanger began decreasing. Though the time of the blockage event is close to 30,000 seconds as test 11-21-05 was, the temperature of the cold inlet stream did not abruptly increase as it did during the 11-21-05 test run, but rather slowly bottomed out and then increased. The flow reduction event appears to have been much more gradual for 11-28-05 than test run 11-21-05.

The increase in the hot outlet temperature near the end of the test occurred because the cold end load heater was energized to accelerate the warm-up of the heat exchanger. The temperature of the cold outlet of the heat exchanger is higher during this run (282 K instead of 271 K for 11-21-05) because during the disassembly of the facility to replace the orifice, 10 additional layers of MLI were placed over the process tubing at the hot end of the heat exchanger. Due to the differences between this test run and 11-21-05, it was decided that a pure substance would be used to investigate the cause of the termination of the flow rate.

3.4.2 Dec 1, 2005 – Jan 5, 2006

Three methane (Grade 1.3) tests were performed to investigate the cause of the blockage. The operating conditions for the first test (Test 12-1-05) is detailed in Table 3.12 and the temperature data is shown in Figure 3.22

Table 3.12: Initial operating conditions for Test 12-01-05

Fluid	Methane
Orifice size	152.4 µm (0.006 in)
Charge Pressure	170 psig
$\dot{V}$	2.2 SLPM
P_H	240 psig
P_{H2}	145 psig
P_{L2}	5.2 psig
P_L	5 psig

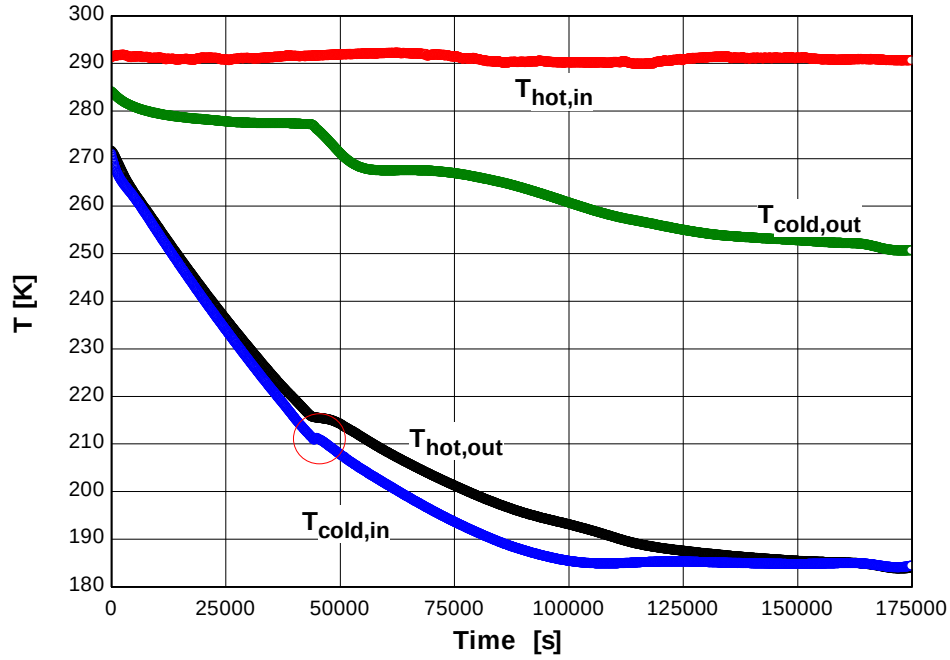

Figure 3.22: Temperature data for Test run 12-01-05.

During this test we observed flow reduction from 2.2 SLPM to 0.5 SLPM when the cold inlet temperature was near 210 K. It remained at 0.5 SLPM from 50,000 to 75,000 seconds (notice that this is the same time frame for which the cold outlet temperature of the heat exchanger remained level). Eventually the flow rate became fully blocked. Also note that the time that the test run took to reach 210 K was approximately twice as long

as the mixture run on 11-28-05. This is due to the smaller refrigeration performance of the methane as compared to the mixture.

Two major facility changes were made after this test run. First, a 0.05 m (2 in) tall, 0.2-2.5 SLPM (Omega FL-2012) flowmeter was installed in parallel with the flow meter to allow the reading of the flow meter to be checked. The uncertainty of this rotameter is 5% of full scale or ±0.125 SLPM. The rotameter's accuracy is approximately 6% of the commonly measured (2.2 SLPM) flow rate for the mixture runs. Second, the output of the flow controller was connected to the data acquisition system to allow the flow rate to be recorded simultaneously with the temperatures. Finally, to test whether the blockage was related to temperature only and not the duration of the test run, the Dewar jacket was filled with liquid nitrogen several hours before the experiment began. The operating conditions for test run 12-07-05 are shown in Table 3.13 and the temperature data is shown in Figure 3.23.

Table 3.13: Initial operating conditions for Test 12-07-05

Fluid	Methane
Orifice size	152.4 μm (0.006 in)
Charge Pressure	200 psig
P_H	271 psig
P_{H2}	172 psig
P_{L2}	27.3 psig
P_L	28 psig

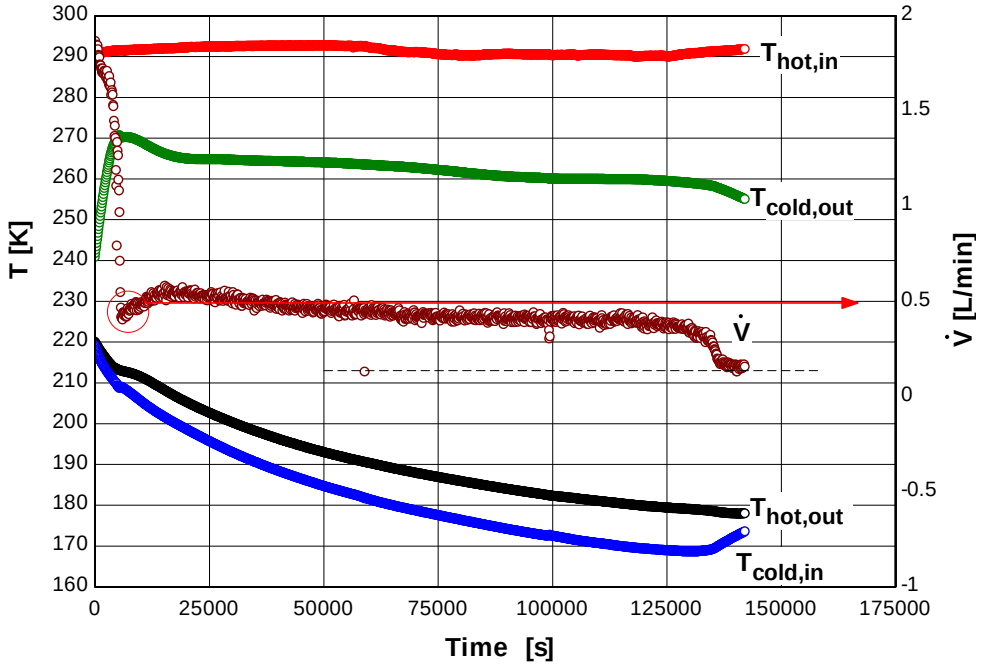

Figure 3.23: Temperature and flow rate data for Test run 12-07-05.

The flow rate was reduced from 1.8 SLPM at the beginning of the test to 0.5 SLPM once the cold inlet temperature reached 210 K. Additionally, the flow rate was at 0.5 SLPM for a much longer duration of the test before it was fully blocked. Near 60,000 seconds the flow was switched to the rotameter and the flow rate was checked and verified. Finally, when the cold outlet was near 170 K the flow rate was completely diminished and the test was terminated. These two runs are shown together in Figure 3.24 for clarity. Note that the flow rate for both test runs were initially diminished to 0.5 SLPM and then eventually fully blocked.

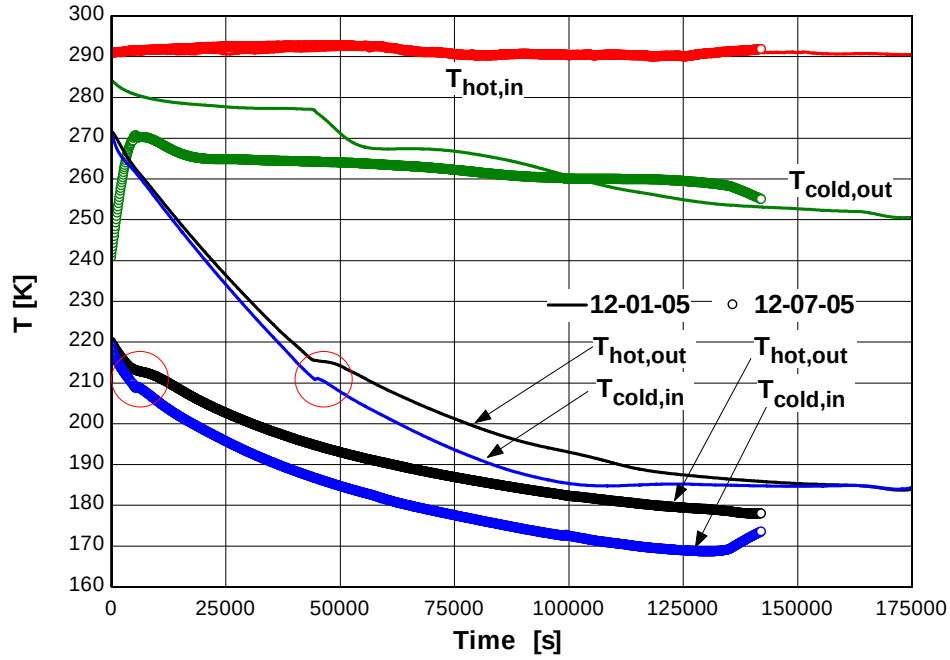

Figure 3.24: Temperature data for test runs 12-01-05 and 12-07-05.

From these results, a contaminant which freezes at 210 K was identified as the cause of flow blockage. To remove this contaminant, a liquid nitrogen trap was designed to be placed before the inlet to the cryostat. The trap consists in a volume of liquid nitrogen surrounding a tube through which the working fluid flows; this allows the contaminants to be frozen out of the gas stream. The trap must contain a sufficient volume of liquid nitrogen to allow 15 hours of operation. Additionally, as the working fluid passes through the trap, it must reach significantly below 210 K, but not below the freezing temperature of any of the constituents of the mixture (nitrogen (63.2 K), methane (90.7 K), ethane (90.4 K)).

Due to the small flow rate of the experiment and the high heat transfer associated with the boiling nitrogen on the outer surface of the tubing (within the trap), the length of tubing

exposed to the liquid nitrogen must be very short. To determine this length, a test was performed using a 0.25 in OD copper U-tube with PRT's attached to each end. The U-tube was connected to the experiment between the compressor and the inlet to the cryostat. The system was then charged with methane and the compressor was energized. The U-tube was then dipped into a small liquid nitrogen bath at varying depths. Once a suitable length was determined, the test was continued and the liquid nitrogen was replenished to maintain the test conditions for several hours. From this test a 0.051 m (2 in) sub-merged pass through length was found to be sufficient.

Initial estimates of the volume of liquid nitrogen needed were made by calculating the boil-off rate that would result from the axial conduction through the pass through tube. Following this estimation, a 20.25 in x 19.88 in x 20.5 in igloo (model: Ice Cube Marine Ultra Roller) cooler was purchased and the drain plug and copper U-tube were sealed with Stycast. Following the installation of the trap at the inlet to the cryostat, a nichrome heater was placed onto the outlet of the trap to provide an added protection against freezing in the trap and allow for more control over the cryostat inlet temperature. Figure 3.25 shows the trap in operation.

Figure 3.25: Liquid Nitrogen Trap.

Following trap installation, test run 12-23-05 began and ran until 12-26-05. The operating conditions for test run 12-23-05 are shown in Table 3.14 and the temperature data is shown in Figure 3.26.

Table 3.14: Initial operating conditions for test 12-23-05

Fluid	Methane
Orifice size	152.4 µm (0.006 in)
Charge Pressure	200 psig
P_H	272 psig
P_{H2}	165 psig
P_{L2}	31.3 psig
P_L	31 psig

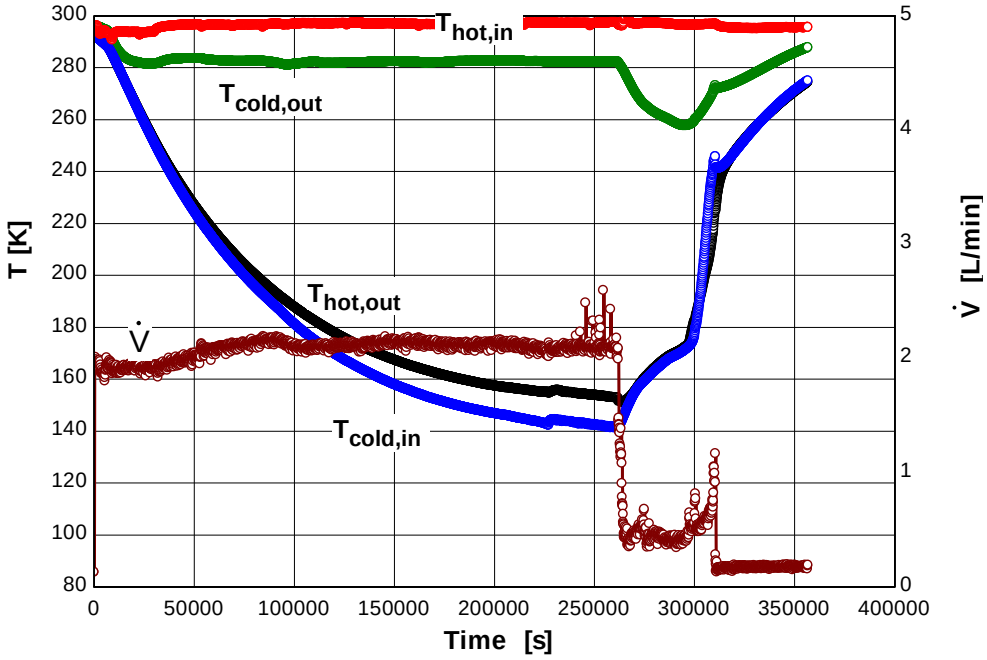

Figure 3.26: Temperature and flow rate data for test run 12-23-05.

Due to the long duration of the test run, there was a concern that the "capacity" of the nitrogen trap was overcome such that some of the freezing contaminant made it through the trap to cause the partial blockage after 250,000 seconds. This hypothesis is supported by the fact that the flow rate was reduced to 0.5 SLPM (the same as the partial blockage of the earlier methane runs). In addition, during the low flow rate time period, the pressure at the inlet to the cryostat was 255 psig while the pressure at the inlet to the orifice (after the finned tube) was 100 psig. This may have indicated blockage within the finned tube itself. On the other hand, the flow rate did begin to oscillate before the blockage event; and this is indicative of the working fluid boiling.

The rise of the cold end temperatures while the flow rate was 0.5 SLPM was due to the lower refrigeration power available at lower flow rates. But the steeper climb in these temperatures after 300,000 seconds was caused by applying heat with the cold end heater, to see if full flow rate conditions could be incurred by raising the cold end temperature. Unfortunately, the flow rate was not fully restored with the increase of the cold end temperature to 240 K. Therefore, the heater was turned off and the experiment allowed to warm to room temperature.

Concluding that, for the majority of the test, the trap had successfully removed the contaminant which had been manifested in the design mixture runs (11-21-05 and 11-28-05). Another attempt was made to use the design mixture to reach cryogenic temperatures with test run 12-28-05. Before the test run, the heater on the outlet of the trap was energized and the pressure of the compressor loop and experimental tubing was evacuated to a vacuum pressure near -12.3 psig for several days to "burn-off" what might remain in the tubing of the trap. Table 3.15 shows the operating conditions and Figure 3.27 shows the temperature data of the test run.

Table 3.15: Initial operating conditions for Test 12-28-05

Fluid	Design Mixture
Orifice size	152.4 µm (0.006 in)
Charge Pressure	255 psig
P_H	330 psig
P_{H2}	200 psig
P_{L2}	82.3 psig
P_L	82 psig

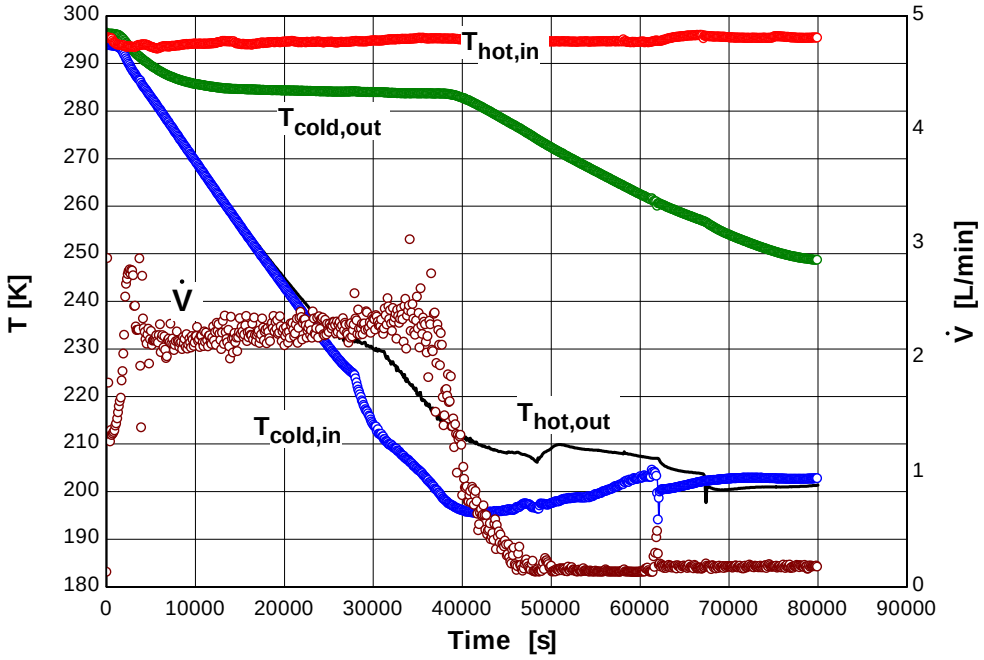

Figure 3.27: Temperature and flow rate data for test run 12-28-05.

The initial oscillations of the mass flow measurement are due to nitrogen boil off from the Dewar jacket being filled at the beginning of the test run. Unlike the design mixture test runs 11-21-05 and 11-28-05, the system cools below 210 K. Below this temperature, the flow rate behaves much like the 12-23-05 methane test run in that there are flow oscillations preceding the flow reduction. The reduction is also more gradual, which is not consistent with a particulate blockage or the formation of a freezing substance which would more abruptly halt the flow rate. The results of this test run provided more confidence that the nitrogen trap was performing sufficiently and that the current flow reduction restraint might be due to the formation of liquid at the orifice. In order to determine if this is a possible explanation, the saturation temperatures for the working fluid needed to be compared with the test runs. For convenience, Figure 3.28 illustrates the saturation temperature of methane and ethane as a function of gauge pressure.

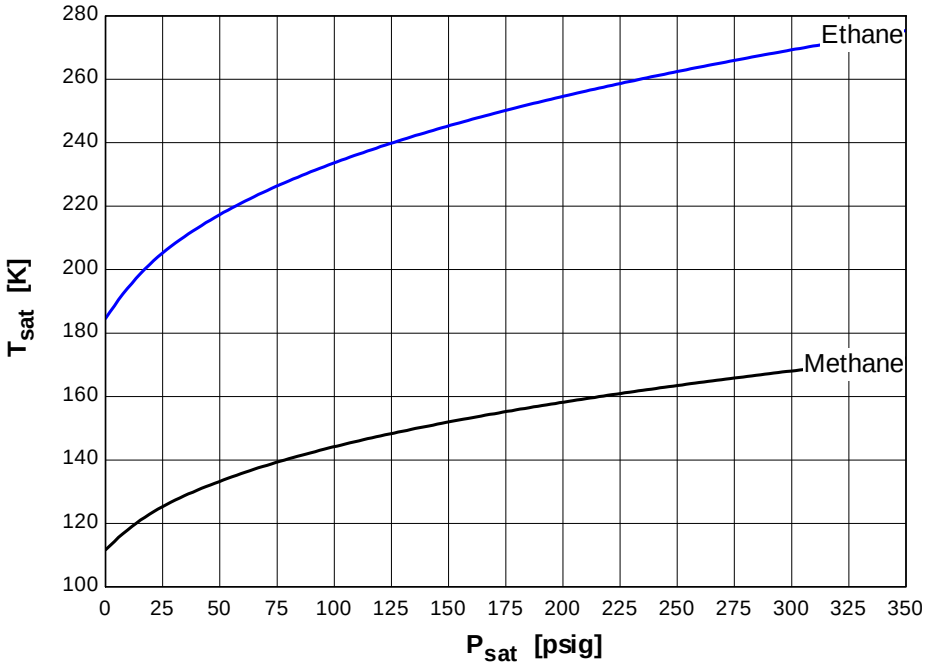

Figure 3.28: Component saturation temperature as a function of gauge pressure.

According to Table 3.14, the pressure at the inlet to the orifice was 165 psig for the 12-23-05 methane test run. Using this pressure, and Figure 3.28, the saturation temperature is approximately 155 K. Examining Figure 3.26, we see that the hot outlet temperature (corresponding to the pressure at the inlet of the orifice) is quite near 155 K when the oscillations appear to have begun. Considering the proximity of these temperatures, it was determined that ethane would be tested to see if similar correspondence with its saturation temperature could be found. The test conditions for this test run are shown in Table 3.16 and the temperature data is shown in Figure 3.29.

Table 3.16: Initial operating conditions for Test 12-30-05

Fluid	Ethane
Orifice size	152.4 μm (0.006 in)
Charge Pressure	215 psig
P_H	265 psig
P_{H2}	175 psig
P_{L2}	25.9 psig
P_L	26 psig

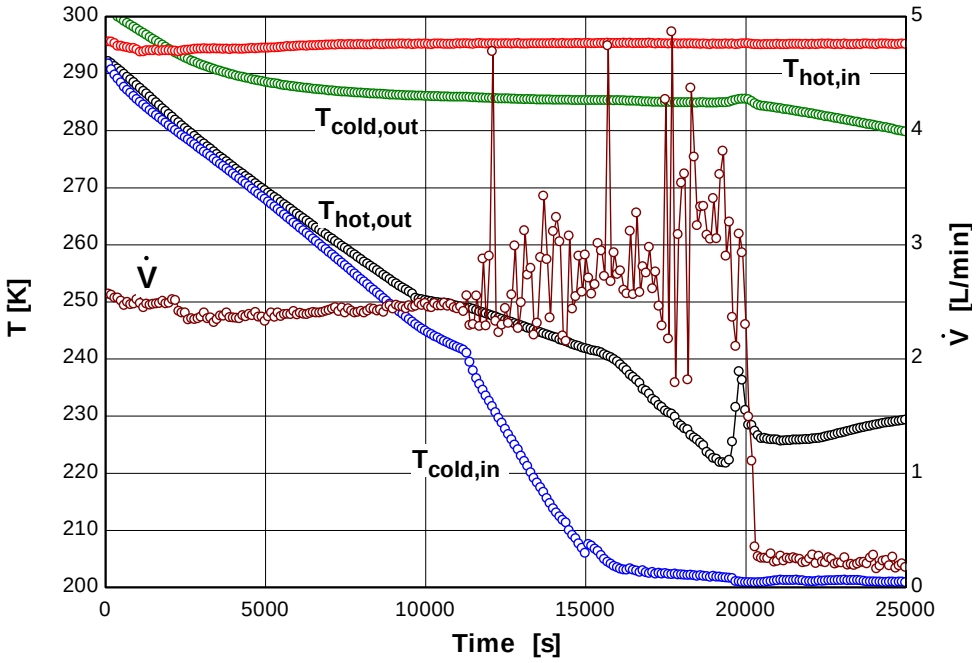

Figure 3.29: Temperature and flow rate data for test run 12-30-05.

As soon as the cold inlet temperature reaches 241 K, the flow rate began oscillating greatly. Although the change in the temperature of the cold inlet stream is more noticeable, at this same time the hot outlet temperature was 249 K. For the pressures outlined in Table 3.16, we see that for the high pressure of 175 psig, the saturation temperature is 250.2 K, while for the low pressure of 26 psig it is 205.8 K. Therefore, the initiation of flow oscillation is more likely due to liquid formation on the inlet side of the

orifice rather than the outlet side. There is a slight glide to the hot outlet temperature (between 249 K and 240 K), but it is clearly not changing as rapidly as the cold inlet temperature or as quickly as it was previous to the flow oscillations. After the hot outlet temperature nears 240 K, the cold inlet temperature levels out near 202 K and remains there until the flow reduction. The reduction in flow rate happens rather abruptly, immediately corresponding to a peak of the hot outlet temperature at 238 K.

Data taken from this point forward, showed that the hot outlet temperature continued to cool toward 200 K, while there was no flow. This is due to the cooling provided by the liquid nitrogen in the Dewar Jacket. The steady state temperature of the cold end of the heat exchanger with no flow is approximately 200 K (± 5 K). The refrigeration power of the ethane is several times larger than methane or even the design mixture. Therefore, a second ethane test run was prepared with no liquid nitrogen within the Dewar jacket. In addition, the time step of the recording scan for the data acquisition system was decreased from 100 to 10 seconds and the test was prepared to run through the day (considering the faster cool down time of the ethane). The operating conditions for test run 01-03-06 are shown in Table 3.17 and the temperature data is shown in Figure 3.30.

Table 3.17: Initial operating conditions for Test 01-03-06

Fluid	Ethane
Orifice size	152.4 μm (0.006 in)
Charge Pressure	200 psig
P_H	255 psig
P_{H2}	155 psig
P_{L2}	18.5 psig
P_L	18 psig

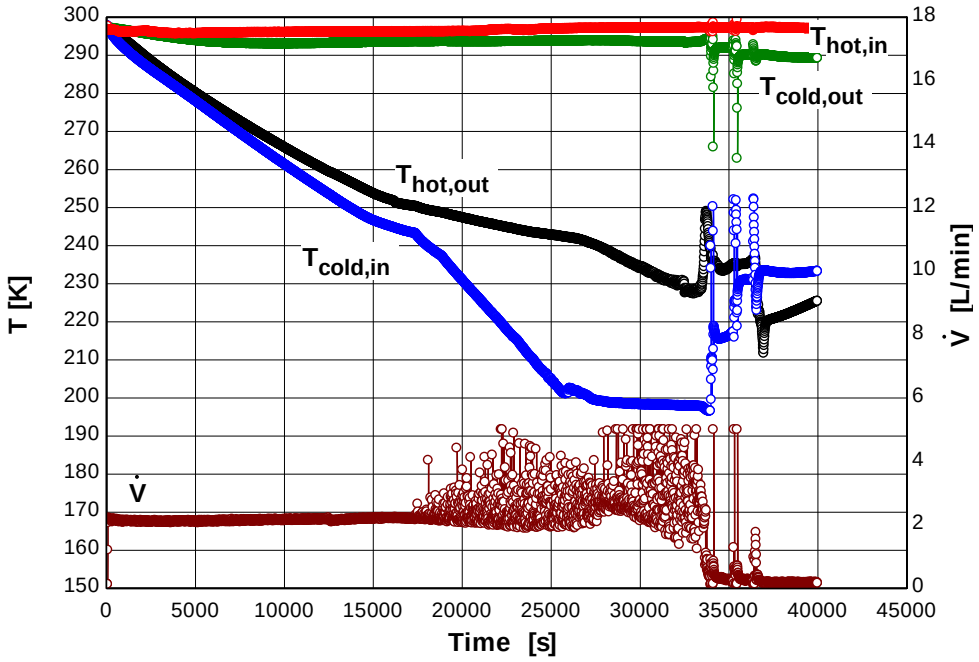

Figure 3.30: Temperature and flow rate data of test run 01-03-06.

The test run is very similar to the previous ethane run. Flow oscillations begin at the hot outlet temperature of 250.3 K. After the cold inlet temperature levels out, the hot outlet temperature cools further to 228 K. To better display the flow reduction event, Figure 3.31 shows only the hot outlet and cold inlet temperatures from time 33,000 seconds to 38,000 seconds.

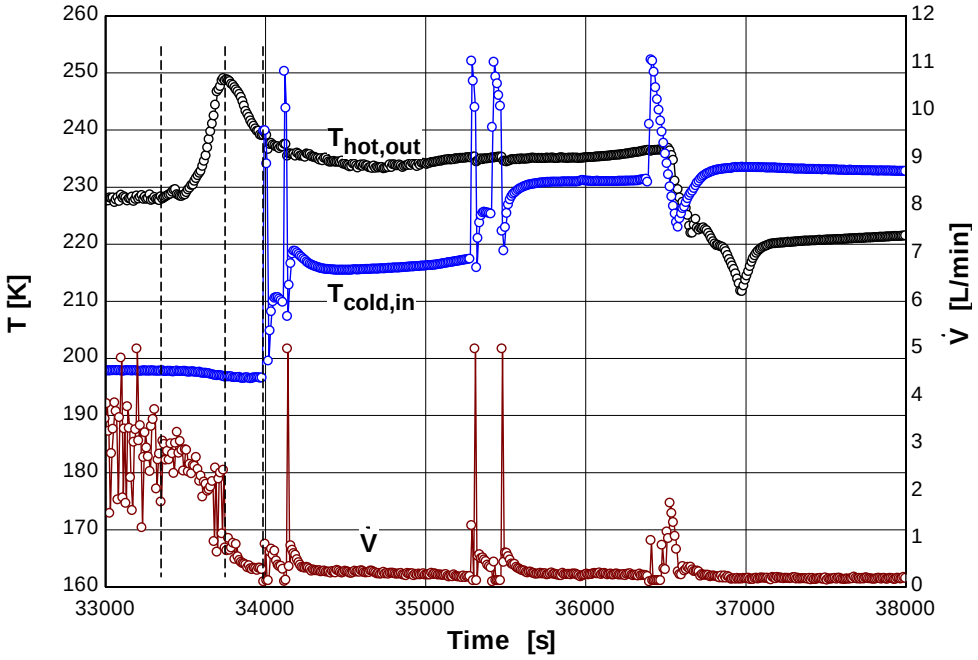

Figure 3.31: Cold end temperatures for test run 01-03-06.

Three dashed lines have been overlaid on Figure 3.31 to indicate the apparent stages of the flow reduction. As the flow rate initially diminishes, the hot outlet temperature begins to rise; peaking at 249 K. Following this peak the temperatures drop as the flow rate gradually diminishes to zero. The next four spikes in the temperature and flow rate are due to the compressor being cycled off and on. Notice that the cold inlet temperature comes much closer to the hot outlet temperature during the cycling. The last spike in the mass flow rate is due to turning the compressor off and subsequently dumping the ethane. Note that the mass flow rate increased for a time and the hot outlet temperature dropped nearly 25 K from 236 K to 211 K before rising again. This behavior is indicative of liquid ethane boiling at the inlet of the orifice. In addition to this data, the pressures at the inlet and outlet of the orifice were recorded from the pressure gauges and are shown in Figure 3.32 and Figure 3.33.

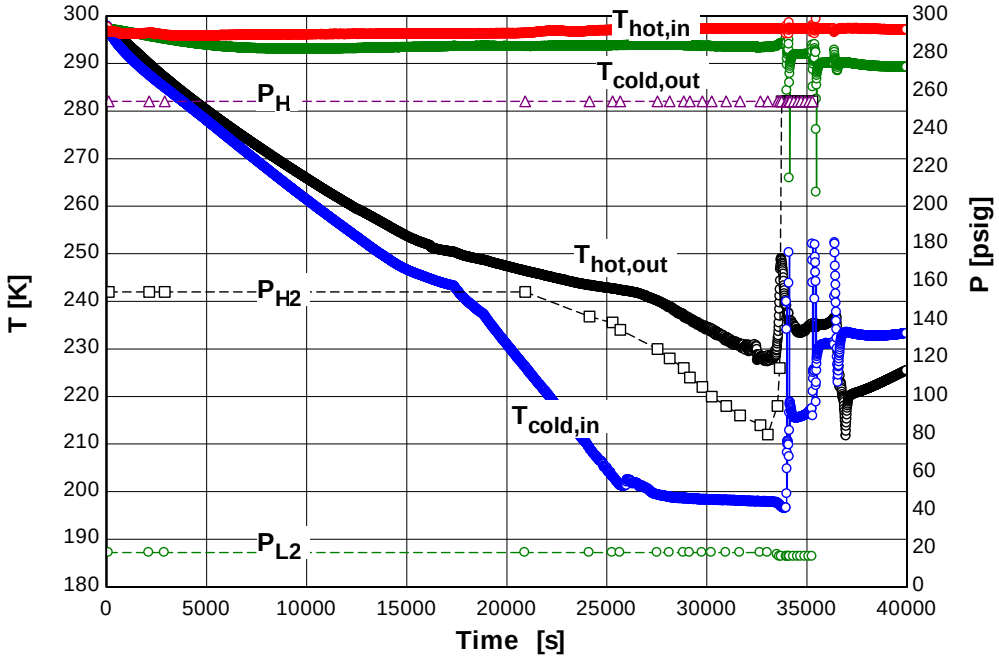

Figure 3.32: Temperature and pressure data for test run 01-03-06.

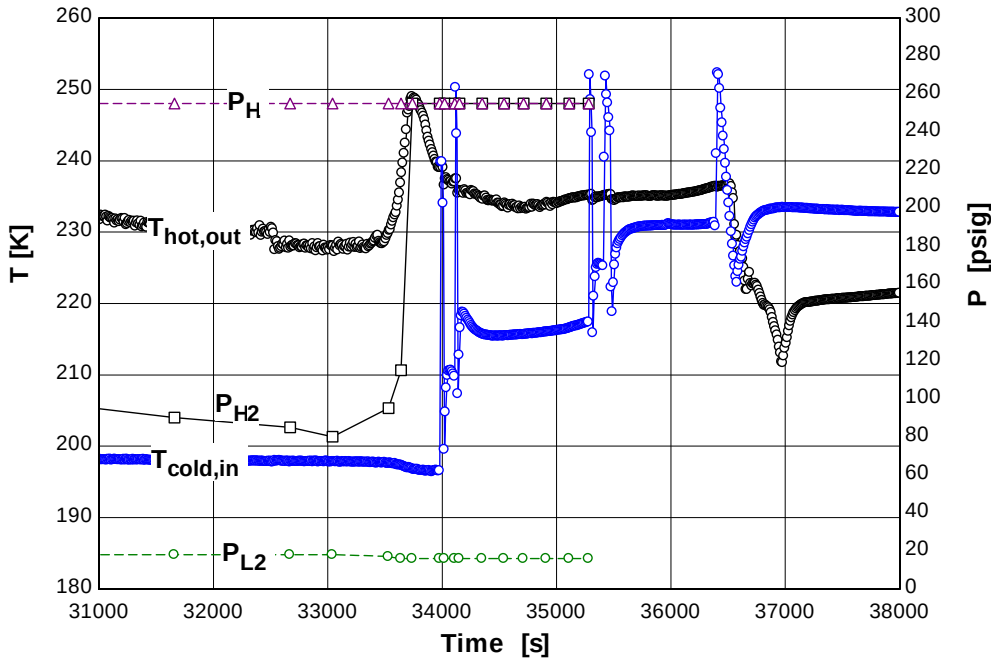

Figure 3.33: Flow reduction event for test 01-03-06.

While the inlet and outlet pressures of the cryostat remain nearly constant, the pressure at the inlet of the orifice slowly drops, then rises sharply at the moment that the hot outlet temperature peaks near 249 K. A P-h diagram for ethane is shown in Figure 3.34. Using the hot outlet and the cold inlet pressures and temperatures recorded between 34,000 and 35,000 seconds, the enthalpy values for the experiment are overlaid the P-h diagram. For this time span, the flow was fully blocked, and it appears from the recorded temperatures and pressures that the hot outlet of the heat exchanger was fully liquid and the cold inlet port was fully vapor.

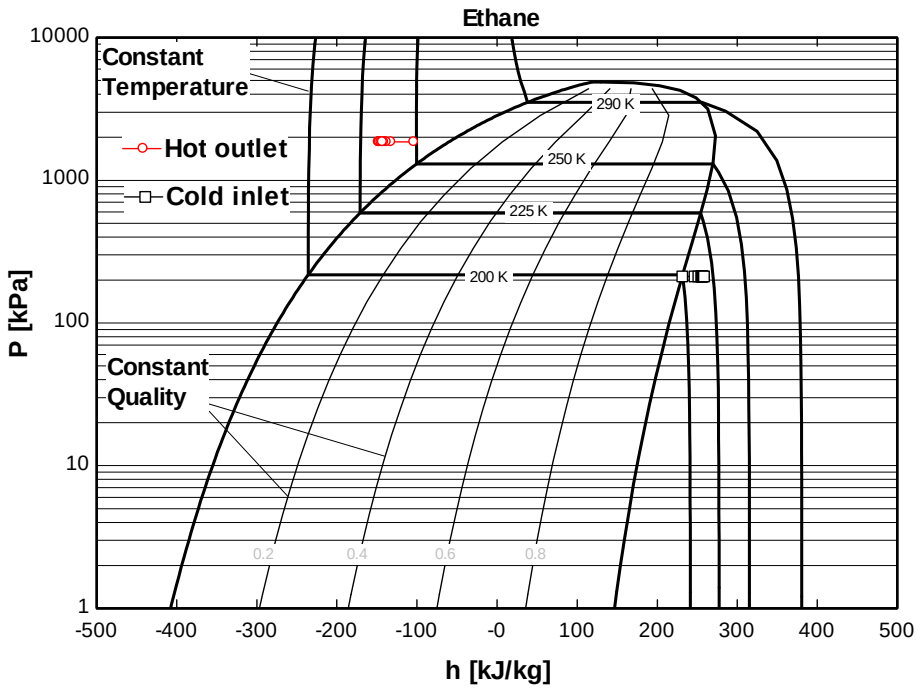

Figure 3.34: P-h diagram for ethane and some test data from test run 01-03-06.

This test conclusively demonstrates that the presence of liquid at the inlet to the orifice is the cause for the flow reduction seen after the nitrogen trap was installed. This presents another constraint to the design of low power MGJT systems employing fixed orifices,

which has not been previously documented. The remainder of the tests performed for this project were focused on exploring this fluid management constraint.

From the previous test run (test 01-03-06), it is not apparent what tolerance there is for the amount of liquid formed at the orifice. Therefore, a different mixture of ethane and nitrogen was selected (Nitrogen 71%, ethane 29%) which maintained a higher vapor quality throughout the temperature range of the heat exchanger. With this mixture, the vapor quality at the cold end should be no greater than 70% at 95 K. At 95 K, the ideal refrigeration power provided by the mixture is 4.9 J/g. For reference, this is less than half of the ideal refrigeration provided (11.4 J/g) by the design mixture at 85 K.

The operating conditions for this test run (01-05-06) are shown in Table 3.18 and the temperature data is shown in Figure 3.35. In light of the smaller refrigeration capacity of the mixture, the liquid nitrogen Dewar was again implemented for this test and continued to be used for the remainder of the test runs.

Table 3.18: Initial operating conditions for Test 01-05-06

Fluid	29 %	Ethane
	71 %	Nitrogen
Orifice size	152.4 μm (0.006 in)	
Charge Pressure	200 psig	
P_H	285 psig	
P_{H2}	185 psig	
P_{L2}	38.9 psig	
P_L	38 psig	

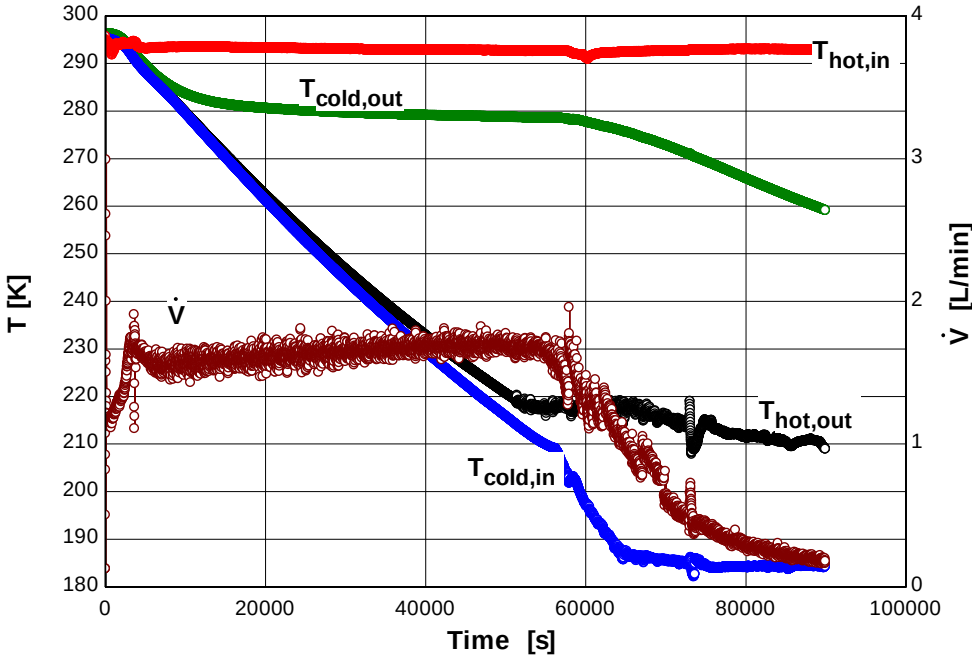

Figure 3.35: Temperature and flow rate data for test run 01-05-06.

The flow reduction was much more gradual for this test mixture than for the design mixture, but fluid blockage eventually resulted. Using the EESNIST4 property database, the predicted vapor quality of the "high quality" mixture at the hot outlet and cold inlet ports is no less than 95 % for all the data from 60,000 to 80,000 seconds. Therefore, the tolerance for the formation of liquid at the orifice appears to be very low and depends on the mixture composition.

3.4.3 Jan 10– March 20, 2006

Two other test runs were performed to determine if cryogenic temperatures could be reached by using a mixture of argon and methane, or simply pure methane. First, a pure argon test run was initiated with the operating conditions shown in Table 3.19. This resulted in a steady state temperature of no less than 185 K.

Table 3.19: Initial operating conditions for argon Test 01-10-06.

Fluid	Argon
Orifice size	152.4 µm (0.006 in)
Charge Pressure	200 psig
$\dot{V}$	0.7 SLPM
P_H	275 psig
P_{H2}	175 psig
P_{L2}	28.5 psig
P_L	28 psig

Subsequently, some of the argon was bled from the system and the remaining argon was diluted with methane such that the resulting mixture was approximately 20% methane. The test was continued with the resulting steady state temperature of 175 K. Although dilution with methane provided a lower cold end temperature, the increase in refrigeration power was not substantial enough to warrant further dilution testing with methane and the test was ended.

Subsequently, the system was charged with pure methane and a low pressure test run (01-16-06) was initiated to take advantage of the low saturation temperature of methane at low pressures. The operating conditions for the test are shown in Table 3.20.

Table 3.20: Initial operating conditions for methane Test 01-16-06.

Fluid	Methane
Orifice size	152.4 µm (0.006 in)
$\dot{V}$	2 SLPM
P_H	245 psig
P_{H2}	115 psig
P_{L2}	0.8 psig
P_L	0 psig

No blockage was experienced during this test run as the saturation temperature for the low pressure of the system (112.3 K) was never reached. Instead the device reached a steady state cold end temperature of 114 K after several days of operation. Therefore, if liquid was avoided, the system could reach cryogenic temperatures with methane, though the cooling power was very low.

The remaining tests focused on determining if the functional dependence of the quality at the orifice inlet and outlet could be effectively varied by varying the operating pressures of the system. The system was filled with the design mixture to a high charge pressure (272 psig) and a test run was executed until full blockage was complete. The liquid nitrogen in the trap and jacket was allowed to boil off and the experiment was returned to room temperature. After thermal equilibrium was achieved, the compressor was turned on and the mixture was allowed to mix for 10 minutes to ensure that the constituents were well mixed before bleeding 10 psig from the system pressure. Table 3.21 shows the initial operating conditions for the first three test runs.

Table 3.21: Initial operating conditions for first three variable charge pressure tests.

Test Run	02-01-06	02-06-06	02-08-06
Orifice size	152.4 μm (0.006 in)	152.4 μm (0.006 in)	152.4 μm (0.006 in)
Charge Pressure	272 psig	265 psig	245 psig
P_H	345 psig	340 psig	325 psig
P_{H2}	245 psig	225 psig	225 psig
P_{L2}	96.6 psig	85.7 psig	73 psig
P_L	94 psig	84 psig	75 psig

After the fourth test run was prepared and initiated, the bottom of the igloo nitrogen trap cracked. This prevented any further data from being gathered until the trap could be

repaired. An attempt at applying Stycast to seal the bottom of the trap container was unsuccessful; therefore, a more permanent design was constructed using stainless steel plate as shown in Figure 3.36.

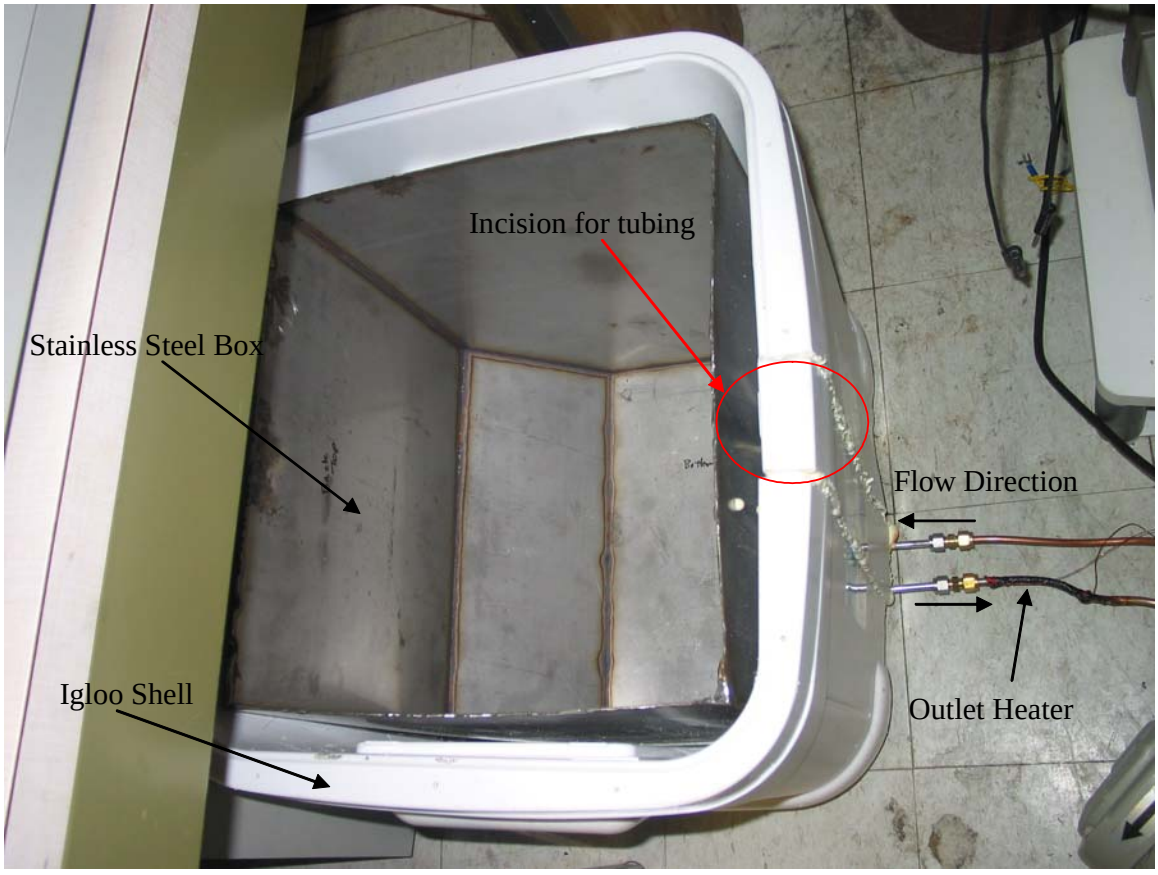

Figure 3.36: Stainless steel liquid nitrogen trap.

Following installation, another set of tests were initiated with the same initial charge pressure. The initial operating conditions for these tests are outlined in Table 3.22.

Table 3.22: Initial operating conditions for variable charge pressure tests following steel trap installation.

Test Run	P_H (psig)	P_{H2} (psig)	P_{L2} (psig)	P_L (psig)	$\dot{V}$ (SLPM)
02-23-06	349	235	99.3	97	2.1
02-25-06	335	235	92	86	2.1
02-27-06	330	230	81.9	80	2.1
03-01-06	320	225	75.2	75	2.1
03-06-06	310	215	66.1	65	2.1
03-08-06	300	205	53.4	54	2.1
03-13-05	290	195	39.9	42	2.1

The flow rate was the same for all runs regardless of the pressures because the compressor is operating with a pressure differential valve which ensures that the pressure differential between the cryostat inlet and outlet is not more than 250 psig. To inspect the data for a trend related to the operating pressures of the system and the flow reduction caused by fluid formation at the orifice, the hot outlet and cold inlet temperature of the heat exchanger were obtained at the time when the flow rate was half the full flow rate. This is considered a more reliable method for tracking the flow reduction event rather than trying to determine its initiation or completion, as these are more gradual and oscillatory. The full flow rate value was chosen arbitrarily as the flow rate at 10,000 seconds during the test run.

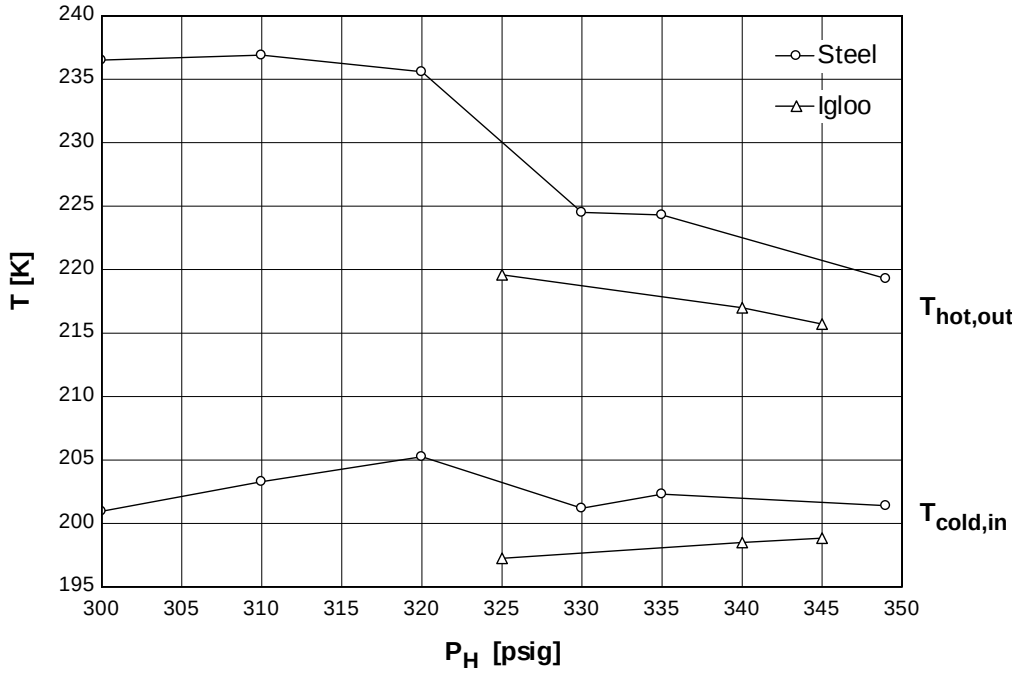

Figure 3.37: Heat exchanger hot outlet and cold inlet temperature as a function of initial inlet pressure for the test runs in **Table 3.21** and **Table 3.22**.

Although the initial "igloo" trap data appears to follow a linear trend, there are only three data points to make use of. The "steel" trap data does not follow a predictable trend at all. There may be an operational reason for this. During the "igloo" trap tests, the pressures at the orifice were always at the pressure of the inlet to the cryostat when the test concluded. This means that the mixture did not freeze in the trap even though the flow rate was stopped. For the "steel" trap data, the pressures at the inlet to the cryostat and at the inlet to the orifice were significantly lower than the discharger pressure from the compressor.

It is likely that for the "steel" trap tests, freezing in the trap began during the flow reduction event, accelerating the reduction of the flow rate and compounding the actual

temperatures which would be reached if the pressures of the system were not altered by freezing within the trap. This can be viewed qualitatively by considering the difference between the flow rate data of test run 03-01-06 (the fourth run of the "steel" data set) and test run 02-08-06 (the third run of the "igloo" data set) shown in Figure 3.38. Notice that the flow rate diminishes more gradually for the "igloo" trap test run. The sharp descent of the flow rate for 03-02-06 is attributed to the design mixture freezing during the fluid blockage event. The flow rate spikes of test run 03-01-06 (as well as the more gradual flow oscillations of test 02-08-06) are not due to compressor operation but due to cyclical freezing in the trap.

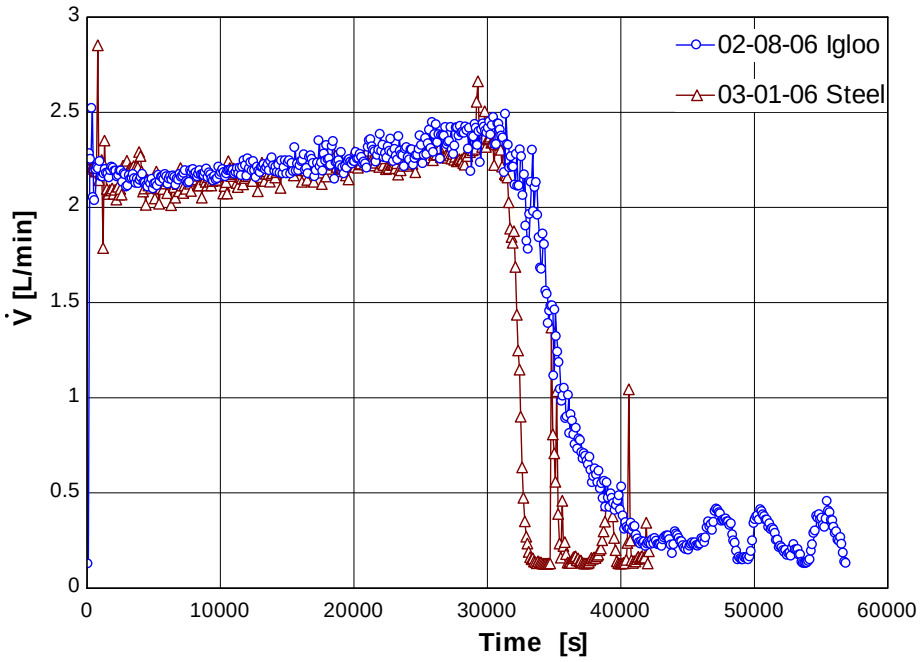

Figure 3.38: Flow rate data comparison of design mixture test runs 02-08-06 and 03-01-06.

These tests do not sufficiently determine the conditions which must be present for this fluid management constraint to be seen in MGJT systems. Presumably such a restriction is only seen at low flow rates where the velocity of the vapor is very low. Further testing

with higher mass flow rates could enable a more thorough exploration of the functional dependence of this restraint.

3.5 Testing Summary

Sections 3.1 to 3.4 are reviewed here to summarize the test results. All of the tests performed with Device A can be segregated into seven categories:

- facility shakedown testing with helium
- heat exchanger testing with helium
- open cycle JT testing with argon
- initial closed cycle JT testing with design mixture
- contamination identification
- fluid blockage identification
- testing to avoid liquid accumulation and efforts to study it

These tests demonstrate that low power, single-stage MGJT systems require particular attention to controlling contaminants and managing the accumulation of liquid at fixed orifice expansion valves. The rationale for each stage of this testing is now reviewed.

The test facility implemented in this project contains a liquid nitrogen bath which permitted preliminary cryogenic testing of the facility outside the context of the JT cycle using helium as the working fluid. To allow the integrity of the test facility (i.e., the ability to take precise measurements and limit the parasitic heat load) to be evaluated in isolation from the heat exchanger, a tube-in-tube heat exchanger was employed in place of Device A. Following verification that the test facility was operating properly, Device A was installed and tested with helium to obtain several steady state measurements for mass flow rates between 0.005 g/s and 0.037 g/s.

Measurements from these helium tests were used to calculate the experimental heat exchanger ineffectiveness (≈ 3%), the parasitic heat load on Device A (≈ 1.25 W), the heat exchanger conductance (*UA*), and the hot stream pressure drop (DP_h). The predictions of the detailed model were compared with these results and reasonable correspondence was found. Replacing the liquid nitrogen bath with a fixed orifice, Device A was subsequently tested in an open JT cycle using high pressure (9.745 MPa) pure argon. The cooling power of the device in this configuration was sufficient to reach the 87.5 K, (approximately the saturation temperature of argon at atmospheric pressure) even while applying 2.67 W to the system with the cold end heater. This confirmed that the heat exchanger performed adequately in this mode of operation, even with obvious accumulation of fluid in the cold end.

Following open cycle testing, the test facility was integrated with an APD compressor and preliminary closed cycle testing was initiated to determine the appropriate orifice size and the pressures for the operation of the cycle. The parasitic heat load was too large for the cooling power of the device (100 mW) to reach a temperature lower than 260 K. Therefore, to insulate the device further from the environment, the outer jacket of the experimental Dewar was filled with liquid nitrogen. In addition, pressure gauges were installed at the inlet and outlet of the orifice to ensure that the pressure drop of the mixture was not significantly different than what was observed for pure substances.

Two additional mixture runs were performed using different orifice diameters (0.0025 in and 0.006 in), and both experienced flow blockage, yet the response of the system to the

blockage event appeared very different in nature. To investigate the blockage event, two pure methane runs were executed which identified a freezing contaminant (210 K) as a cause of flow blockage. After the installation of a liquid nitrogen trap, a follow-up methane run reached a cold end temperature of 150 K, but then experienced flow blockage. Considering that trap was successful at removing the freezing contaminant for the majority of the test, the design mixture was tested again, and the flow rate showed a gradual flow reduction. To determine if the flow blockage being observed at this time was due to fluid accumulation in the cold end, two pure ethane test runs were performed. The flow reduction event observed during these two tests tracked very closely with the saturation temperature of ethane at the operating pressures of the system. This conclusively demonstrated the existence of a fluid management constraint relative to the operation of fixed orifice expansion valves at low flow rates.

In an effort to limit the amount of liquid accumulating at the cold end, a nitrogen and ethane mixture (Nitrogen 71%, ethane 29%) was selected which provided less refrigeration, but had a much higher vapor quality throughout the temperature range of the heat exchanger. During the test run, full fluid blockage resulted, even though the vapor quality at the inlet and outlet of the orifice was calculated to be above 95% for the pressures and temperatures recorded. This showed that the system was very sensitive to even small amounts of liquid.

Two other test runs were designed for all gas operation. First, an argon test run was initiated and later diluted with methane (18%). The refrigeration power of this mixture

was only sufficient to bring the cold end temperature to 175 K with little hope of reaching below 120 K, therefore, this mixture was abandoned. Second, a pure methane test run was implemented such that the low pressure of the compressor was very near atmospheric pressure. This ensured that liquid formation would only take place at a low temperature (as the saturation temperature is 112.5 K). This test run successfully reached 114 K, but only after several days of operation due to the low refrigeration power of methane at these conditions.

Finally, an attempt was made to characterize the pressure dependence of the fluid management constraint, by incrementally decreasing the operating pressures of the system. The results of these tests showed no predictable trend. The cause of this experimental ambiguity is presumed to be due to freezing of the design mixture within the nitrogen trap during the flow reduction event, compounding the relationship between operating pressures and temperatures.

Chapter 4 Summary

Mixed gas Joule-Thomson systems can provide increased refrigeration power and higher efficiency for a larger temperature range as compared with Joule-Thomson systems using single-component working fluids. This thesis describes the development of a set of modeling tools that are useful for the design of the recuperative heat exchanger within a single-stage, low power MGJT cycle. Preliminary experimental test results are presented which indicate an important design constraint relative to the formation of liquid at fixed orifice expansion valves; this constraint was not previously observed for operation at higher vapor velocities and may be an issue that is somewhat unique to the low power, high efficiency device considered here.

The mixture optimization model employed during this project provides a flexible and robust tool for selecting mixtures for a MGJT cycle. Following mixture selection, the influence of the heat exchanger loss factors on the ideal performance of the MGJT cycle were considered using a modified version of the optimization model in order to identify appropriate target values for performance given the specific application under consideration. A detailed model of the Hampson style heat exchanger was developed to allow the design of a demonstration device.

The demonstration device was fabricated and integrated with a test facility in order to allow component-level testing of the heat exchanger, as well as open and closed cycle operation. Testing with helium outside of the context of a JT cycle enabled the heat

exchanger design tools to be verified. The test facility was altered to permit open cycle testing with pure argon and a heat load curve was measured, confirming that the heat exchanger performed adequately in this mode of operation. The test facility was integrated with a compressor and closed cycle operation revealed the presence of a freezing contaminant in the gas stream. After the installation of a liquid nitrogen trap, pure and mixed gas tests revealed a liquid management constraint relative to low mass flow rate fixed orifice systems. Further study of this constraint with could permit the liquid management issue to be characterized more rigorously; specifically a correlation of the vapor velocity below which liquid will collect for a given quality/density/etc. combination would be extremely valuable as this constraint could be integrated into future design methodologies for this type of system.

Recommendations for Future Work

To obtain a more complete characterization of the liquid build-up phenomena that was observed in the experiments presented in this thesis it is necessary to build a larger recuperative heat exchanger. This larger heat exchanger would provide more cooling power and therefore allow the test facility to operate without using the liquid nitrogen jacket; additionally, the system could operate at higher mass flow rates which would, presumably, alleviate the liquid management issue. Such a system would allow several factors to be studied parametrically:

- the critical orifice size for fluid blockage (or, the critical vapor velocity),
- the dependence of fluid blockage on orifice inlet pressure,
- the influence of fluid properties on fluid blockage, and
- the possible control of fluid blockage using an adjustable valve.

The factors mentioned above are most likely inter-related. However, a full description of how these factors influence fluid blockage would accomplish much toward the development of low power MGJT cycles for cooling distributed loads.

References

Alexeev, A., Haberstroh, Ch., Quack, H., "Further Development of a Mixed Gas Joule Thomson Refrigerator", *Advances in Cryogenic Engineering*, Vol 43, pp. 1667-1674, (1997).

Alfeev, V. N., et al., Great Britain Patent, No. 1,336,892, (1973).

Automation Creations, Inc. (ACI), *MatWeb-Material Property Data*, April 1, 2006, http://www.matweb.com (November, 2005).

Boiarski, M., et al., "Design Optimization of the Throttle-Cycle Cooler with Mixed Refrigerant", *Cryocoolers 10*, Kluwer Academic, New York, pp. 457-465, (1998).

Chien, Chen, and Chou, "A study on the transient characteristics of a self-regulating Joule-Thomson cyrocooler", *Cryogenics*, Vol. 36, pp.979-984, (1996).

Ely, J. F., and Huber, M. L., *NIST Thermophysical Properties of Hydrocarbon Mixtures Database (SUPERTRAPP)*, NIST Standard Reference Database 4, U.S. Department of Commerce, National Institute of Standards and Technology, Version 3, (2003).

Incropera, F., DeWitt, D., 2002, *Introduction to Heat Transfer*, John Wiley & Sons, New York.

G. F. Nellis, C. B. Hughes, and J. M. Pfotenhauer, "Heat Transfer Coefficient Measurements for Mixed Gas Working Fluids at Cryogenic Temperatures," *Cryogenics*, Vol. 45, No. 8, pp. 546-556, August, (2005).

Gong, M.Q., Lou, E. C., Zhou, Y., Liang, J. T., and Zhang, L., "Optimum Composition Calculation for Multicomponent Cyrogenic Mixture used in Joule-Thomson Refrigerators", *Advances in Cryogenic Engineering*, Vol. 45, pp.283-290 (2000).

Keppler, F., Nellis, G., and Klein, S., "Optimization of the Composition of a Gas Mixture in a Joule-Thomson Cycle", *International Journal of Heating, Ventilation, Air Conditioning, and Refrigeration Research*, Vol 10, No. 2, pp. 213-230, April (2004).

Klein, S.A., EES – *Engineering Equation Solver*, F-chart Software (2005).

Little, W. A., "Method for Efficient Counter-Current Heat Exchange using Optmized Mixtures", *U.S. patent No. 5,644,502*, (1997).

Lemmon, E.W., McLinden, M.L, and Huber, M.L., "REFPROP – Reference Fluid and Thermodynamic and Transport Properties,", NIST Standard Reference Database 23, U.S. Department of Commerce, National Institute of Standards and Technology, Version 7.1, (2003)

Luo, E. C., et al. “The Research and Development of Cryogenic Mixed-Refrigerant Joule-Thomson Cryocoolers in CL/CAS”, *Advances in Cryogenic Engineering*, Vol. 45, Part A, Kluwer Press, New York, pp. 299-306, (2000).

Maytal, B. Z., Nellis, G. F., Klein, S. A., and J. M. Pfotenhauer, "Elevated-pressure mixed-coolants Joule-Thomson cryocooling," accepted for publication in *Cryogenics*, December, 2005.

Muller-Steinhagen H., Heck, K., “A simple friction pressure drop correlation for two-phase flow in pipes”, *Chem. Eng. Process*, Vol. 20, pp. 297-308, (1986).

Naer, V., Rozhentsev, A., “Application of hydrocarbon mixtures in small refrigerating and cryogenic machines”, *International Journal of Refrigeration*, Vol. 25, pp. 836-847, (2002).

Nellis, G. F., Pfotenhauer, J. M., Klein, S. A., “Actively Cooled Current Leads For Superconducting Electronics using Mixed-Gas Joule-Thomson Refrigeration”, *Proceedings of IMECE: 2004 ASME International Mechanical Engineering Congress & Exposition,* Washington, D.C., November 16-21, (2004).

Ng, K. C., Xue, H., and Wang, J. B., “Experimental and numerical study on a miniature Joule-Thomson cooler for steady state characteristics”, *International Journal of Heat and Mass Transfer,* Vol 45. pp. 609-618, (2002).

Ould Didi, M.B., Kattan, N., Thome, J.R., “Prediction of two-phase pressure gradients of refrigerants in horizontal tubes”, *International Journal of Refrigeration*, Vol. 25, pp. 935-947, (2002).

Rijpman, A. P., ter Brake, H. J. M., Holland, H. J., and Rogalla, H., "High-Tc SQUID Based Gradiometer Cooled by a Cryotiger Gas-mixture Cooler", *Cryocoolers 12*, R. G. Ross, ed., Kluwer Academic/Plenum, pp. 789-797, (2003).

Timmerhaus, K., Flynn T., *Cryogenic Process Engineering,* Plenum Press, New York. (1989).

Williams, J.E.C., “Counterflow current leads for cryogenic applications”, *Cryogenics*, Vol 3. p.234, (1963).

Appendix A

The following figures provide the temperature and flow rate data for all of the varied pressure test runs. All of the test runs shown in this appendix were accomplished using the 152.4 µm (0.006 in) orifice and the Design mixture. Each figure has a corresponding table containing the recorded initial and final pressures.

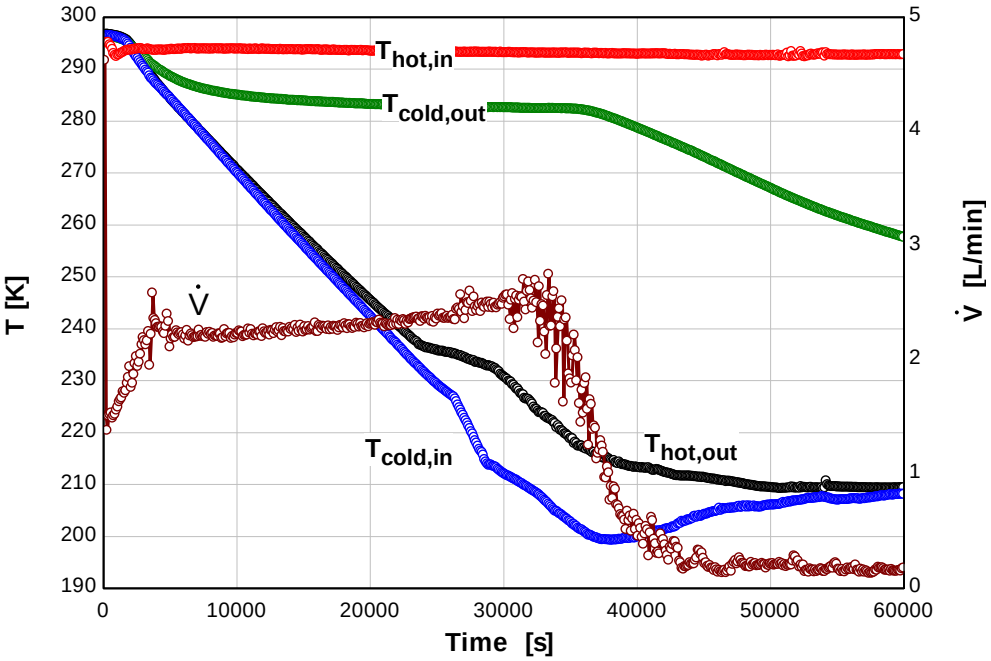

Figure A.1: Temperature and flow rate data for test 02-01-06.

Table A.1: Initial and final operating pressures for test 02-01-06

Initial Pressures		Final Pressures
P_H	345 psig	210-190 psig (pulsing)
P_{H2}	245 psig	180-170 psig (pulsing)
P_{L2}	96.6 psig	89.7 psig
P_L	94 psig	86 psig

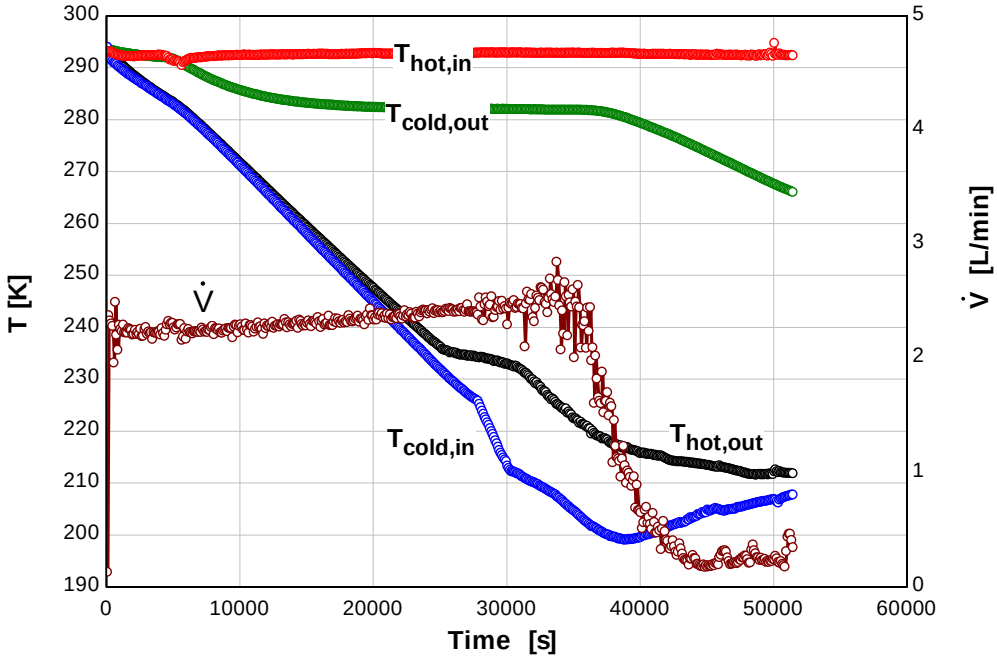

Figure A.2: Temperature and flow rate data for test 02-06-06.

Table A.2: Initial and final operating pressures for test 02-06-06

Initial Pressures		Final Pressures
P_H	340 psig	N/A
P_{H2}	225 psig	N/A
P_{L2}	85.7 psig	N/A
P_L	84 psig	N/A

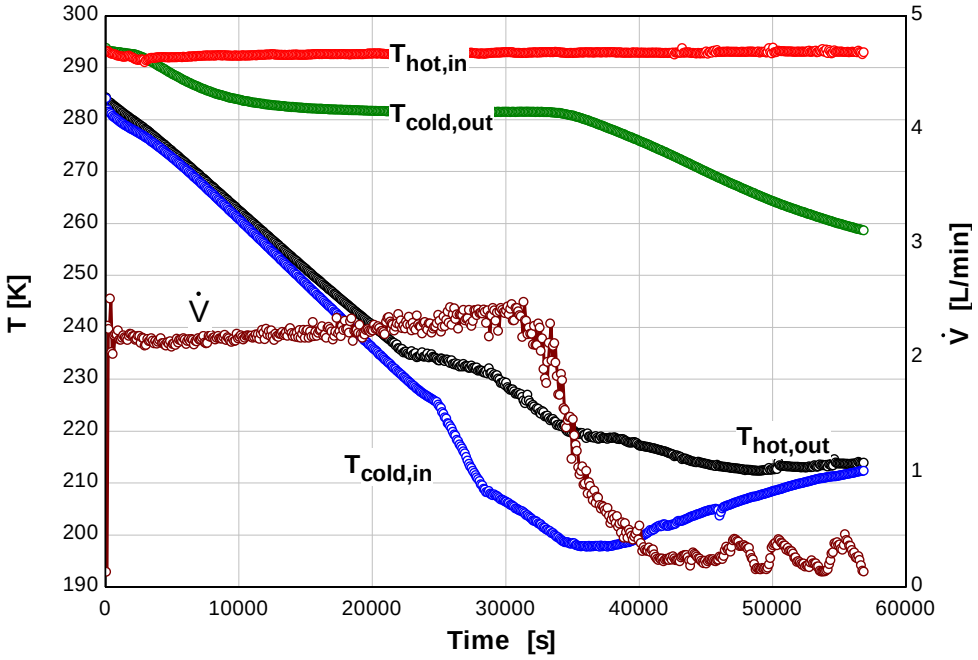

Figure A.3: Temperature and flow rate data for test 02-08-06.

Table A.3: Initial and final operating pressures for test 02-08-06

Initial Pressures		Final Pressures
P_H	320 psig	220 psig
P_{H2}	222 psig	220 psig
P_{L2}	67.8 psig	65.6 psig
P_L	70 psig	65 psig

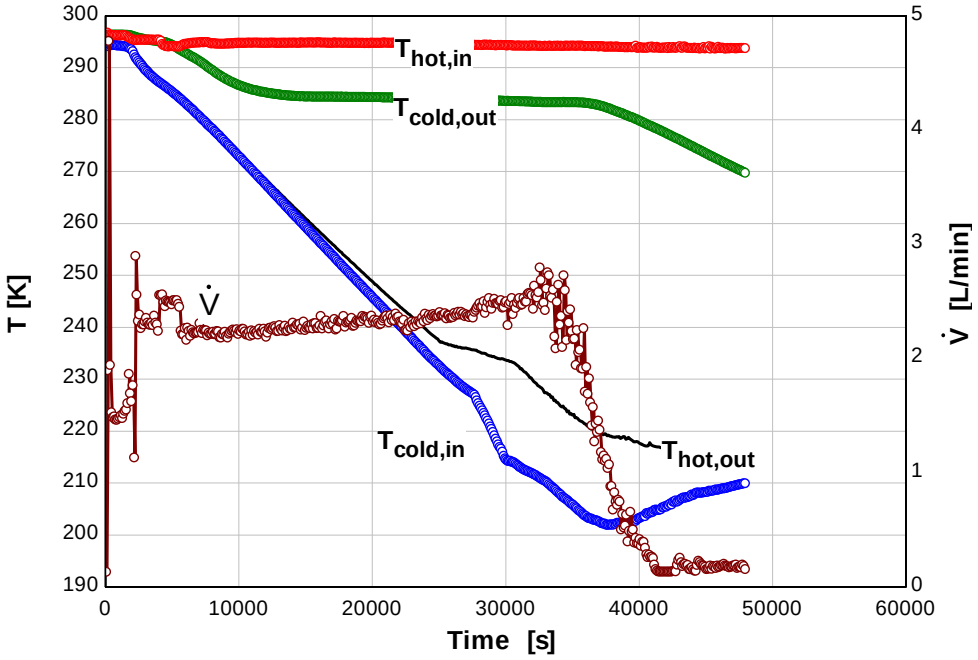

Figure A.4: Temperature and flow rate data for test 02-23-06.

Table A.4: Initial and final operating pressures for test 02-23-06

Initial Pressures		Final Pressures
P_H	349 psig	135 psig
P_{H2}	235 psig	135 psig
P_{L2}	99.3 psig	95.4 psig
P_L	97 psig	90 psig

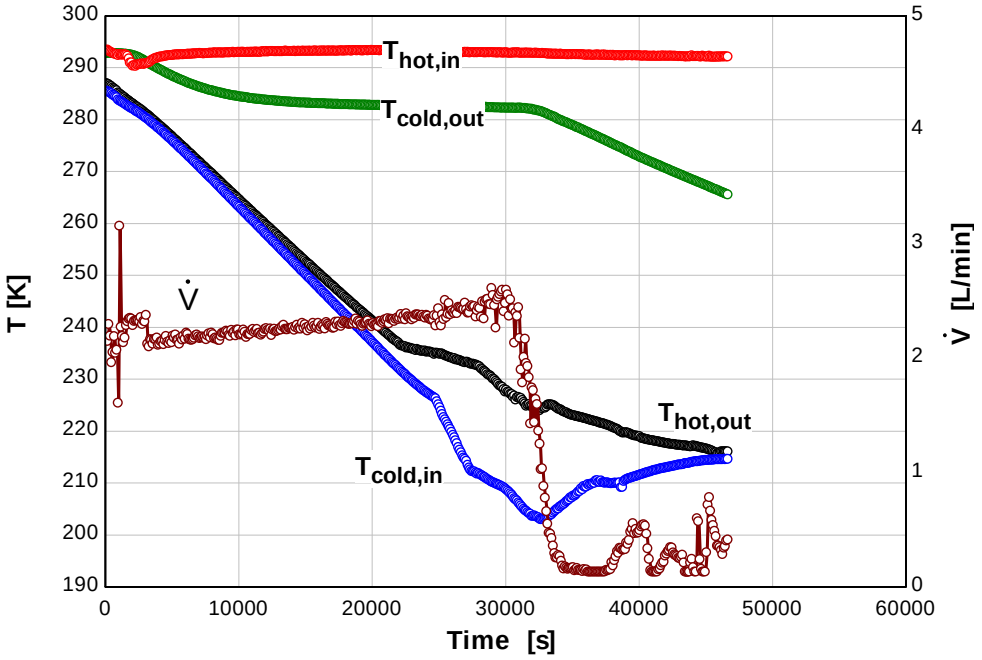

Figure A.5: Temperature and flow rate data for test 02-25-06.

Table A.5: Initial and final operating pressures for test 02-25-06

Initial Pressures		Final Pressures
P_H	335 psig	210-185 psig (pulsing)
P_{H2}	235 psig	210-185 psig (pulsing)
P_{L2}	92 psig	86.7 psig
P_L	86 psig	80 psig

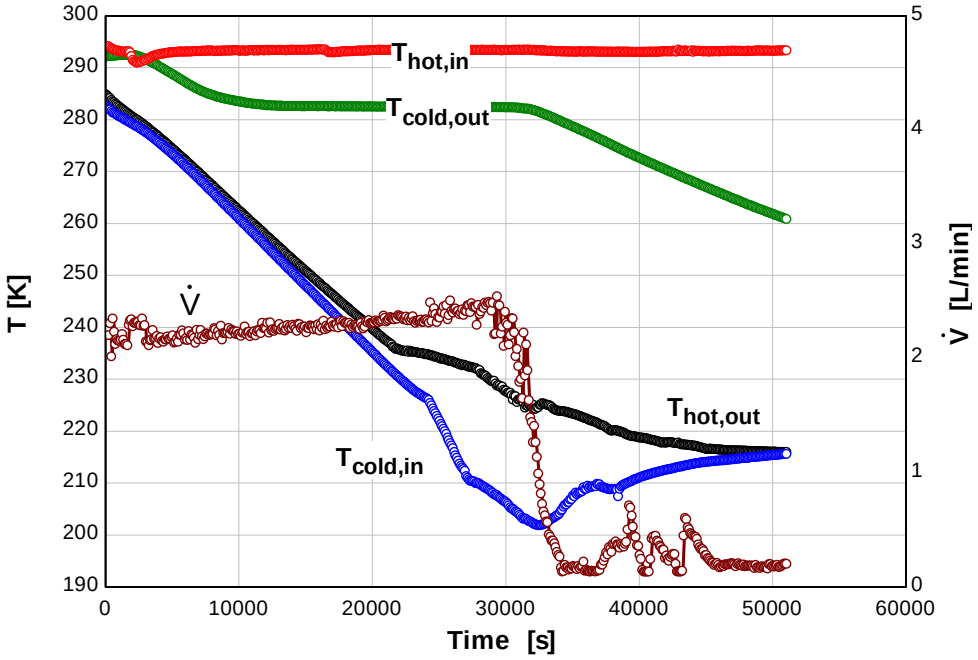

Figure A.6: Temperature and flow rate data for test 02-27-06.

Table A.6: Initial and final operating pressures for test 02-27-06

Initial Pressures		Final Pressures
P_H	330 psig	80 psig
P_{H2}	230 psig	75 psig
P_{L2}	81.9 psig	79.4 psig
P_L	80 psig	75 psig

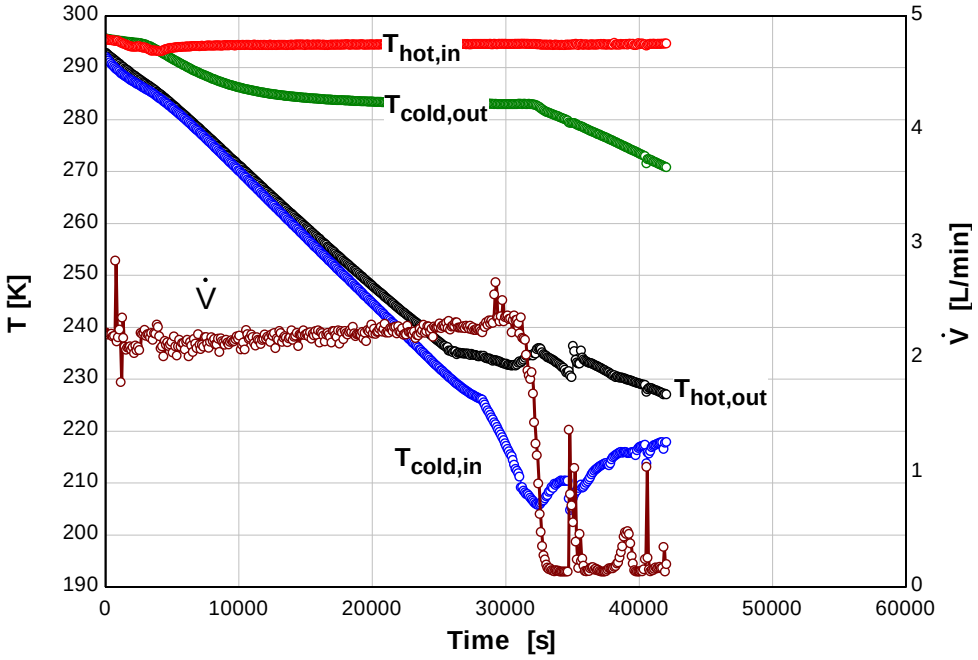

Figure A.7: Temperature and flow rate data for test 03-01-06.

Table A.7: Initial and final operating pressures for test 03-01-06

Initial Pressures		Final Pressures
P_H	320 psig	75 psig
P_{H2}	225 psig	70 psig
P_{L2}	75.2 psig	71 psig
P_L	75 psig	70 psig

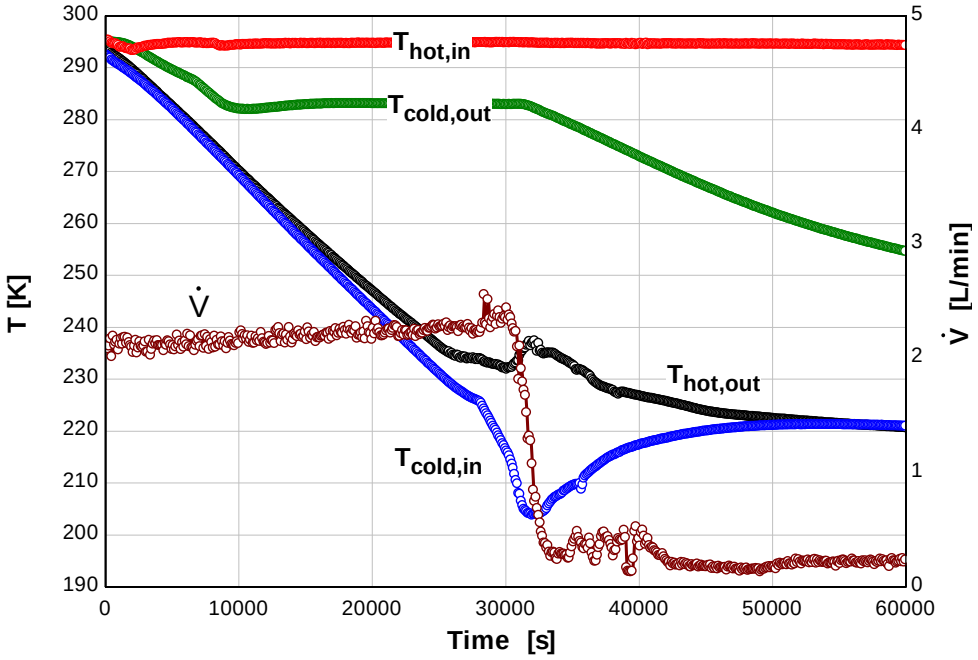

Figure A.8: Temperature and flow rate data for test 03-06-06.

Table A.8: Initial and final operating pressures for test 03-06-06

Initial Pressures		Final Pressures
P_H	310 psig	60 psig
P_{H2}	215 psig	55 psig
P_{L2}	66.1 psig	62.2 psig
P_L	65 psig	60 psig

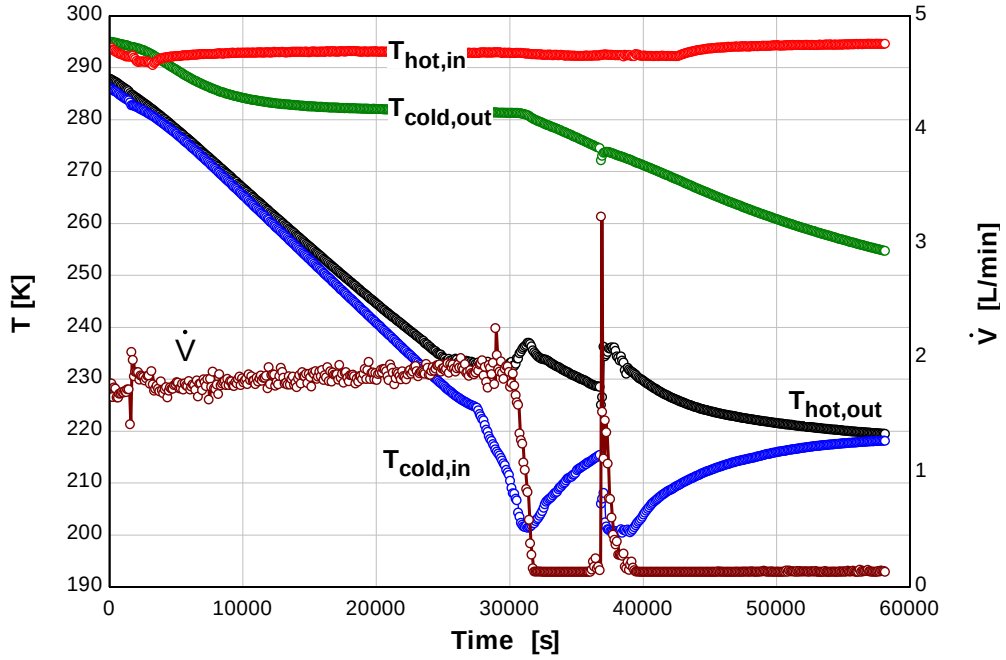

Figure A.9: Temperature and flow rate data for test 03-08-06.

Table A.9: Initial and final operating pressures for test 03-08-06

Initial Pressures		Final Pressures
P_H	300 psig	55 psig
P_{H2}	205 psig	50 psig
P_{L2}	53.4 psig	53.4 psig
P_L	54 psig	52.5 psig

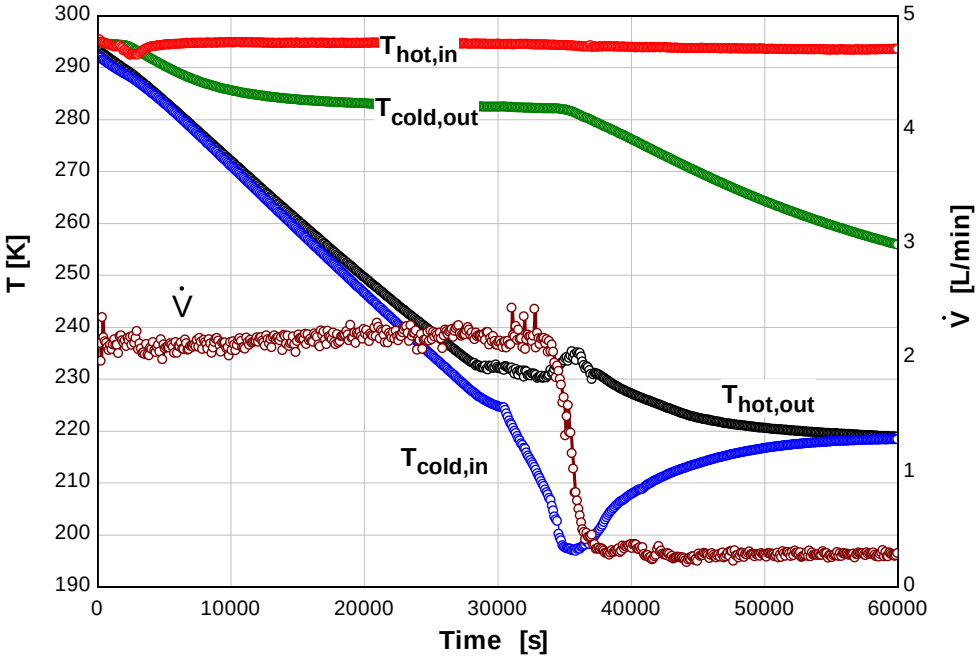

Figure A.10: Temperature and flow rate data for test 03-13-06.

Table A.10: Initial and final operating pressures for test 03-13-06

Initial Pressures		Final Pressures
P_H	290 psig	40 psig
P_{H2}	195 psig	35 psig
P_{L2}	39.9 psig	36.6 psig
P_L	42 psig	39 psig